LABEL-FREE BREAST HISTOPATHOLOGY USING QUANTITATIVE PHASE IMAGING

BY

HASSAAN MAJEED

DISSERTATION

Submitted in partial fulfillment of the requirements
for the degree of Doctor of Philosophy in Bioengineering
in the Graduate College of the
University of Illinois at Urbana-Champaign, 2018

Urbana, Illinois

Doctoral Committee:

Professor Gabriel Popescu, Chair
Professor Andre Kajdacsy-Balla
Professor Stephen Allen Boppart
Professor Michael Insana

ABSTRACT

According to the latest World Health Organization (WHO) statistics, breast cancer is the most common type of cancer among women worldwide (1). The WHO has further emphasized that early diagnosis and treatment are key in mitigating the burden of disease (2). In spite of this assessment, the standard histopathology of breast cancer still relies on manual microscopic examination of stained tissue. Being qualitative and manual in nature, this standard diagnostic procedure can suffer from inter-observer variation and low-throughput (3). In addition, stain variation between different samples and different laboratories creates problems for supervised image analysis methods for automated diagnosis. **A quantitative, label-free and automatable microscopic modality for breast cancer diagnosis is, thus, needed to address these shortcomings in the standard method.**

Furthermore, prognostic biomarkers are important tools used by clinicians in order assess the disease course in patients (4). Being correlated with outcomes, these markers allow pathologists to determine aggressiveness of disease and tailor treatment accordingly. However, the current set of biomarkers for breast cancer are ineffective in predicting outcomes in all patients and there is a need for additional markers of prognosis to better account for variation among individuals (5, 6). **Microscopic and imaging tools for extracting new, quantitative biomarkers during breast histopathology are, thus, also desirable.**

Although a number of new quantitative imaging modalities for diagnostic and prognostic evaluations have been proposed, a key challenge remains compatibility with the existing workflow for easier clinical translation. **Quantitative methods that minimally affect the clinical pipeline already in place are expected to have a greater impact than those that require significant new infrastructure.**

During my graduate work I have approached these problems in modern breast histopathology by using quantitative phase imaging (QPI). QPI is a label-free microscopy technique where image contrast is generated by measuring the optical path-length difference (OPD) across the specimen. OPD refers to the product of the refractive index and thickness at a point in the field of view. Since this measurement relies on a physical property of tissue and is label-free, it provides an objective and potentially automatable basis for tissue assessment. We employ a QPI technique called Spatial Light Interference Microscopy (SLIM) for investigations carried out during this thesis research.

The specific aims of my thesis research are:

1. Label-free quantitative evaluation of breast biopsies using SLIM: In this work, we show by imaging a tissue microarray (TMA) that our QPI based method can separate benign and malignant cases by relying on tissue OPD based features. By employing image processing and statistical learning, we demonstrate a label-free quantitative diagnosis scheme that can provide an objective basis for tissue assessment. A quantitative method like this can also, potentially, be automated, reducing case-load for pathologists by automatically flagging problematic cases that require further investigation.

2. Quantifying tumor adjacent collagen structure in breast tissue using SLIM: Recent evidence shows that the structure of tumor adjacent collagen fibers influences tumor progression. In particular, collagen fiber alignment and orientation can facilitate epithelial invasion to surrounding tissue (5). We demonstrate that SLIM can be used to detect this prognostic marker that in the past had been detected using Second Harmonic Generation Microscopy (SHGM). Our

SLIM based method improves on the SHGM based method in terms of throughput and the fact that cellular information can be obtained, in addition to collagen fiber structure, in a single image.

3. Quantitative histopathology on stained tissue biopsies: The instruments and image analysis tools developed in Aims 1 and 2 are designed for unstained tissue biopsies. Since standard tissue histopathology inevitably requires staining, we aim to demonstrate that we can extend these tools to stained tissue biopsies. In this way, the standard diagnostic workflow will be minimally disrupted. In addition, from a single shot, both an OPD map and stained tissue bright field image will be obtainable for evaluation. We demonstrate that QPI images of stained tissue can be used to solve diagnostic and prognostic problems in breast tissue assessment, using quantitative markers.

ACKNOWLEDGEMENTS

I would like to begin by acknowledging my family – my wife, parents and sisters – whose support allowed me to pull through during the most difficult times. Since like many others my thesis work tended to override everything else in my life, their patience and encouragement was instrumental in my achieving what I have been able to.

I'd also like to acknowledge my lab-mates and collaborators whose ideas are represented throughout this thesis. My work is extremely multidisciplinary – it combines aspects of optical science, tissue biology, clinical pathology and computer science. I had to, therefore, rely heavily on the expertise of others to teach me and guide me through. Needless to say none of these projects would have been completed without the combined effort of the teams I was a part of.

Finally, I'd like to thank my adviser and my doctoral thesis committee for both their praise and constructive criticism. I strongly believe that, as budding scientist, interactions with field experts are the most educational in understanding the issues and challenges within that field. This work would be much less scientifically sound and significant without their input and feedback.

To Fatima, Nasira, Nasim, Hina

and Ayesha – the most important people in my life.

TABLE OF CONTENTS

CHAPTER 1: Introduction

1.1 Background and Significance

According to the latest figures of the International Agency for Research on Cancer (IARC) – a part of the WHO – breast cancer is the most commonly diagnosed cancer among women in both the developed and the developing world (1). The American Cancer Society predicts that in 2018 around 266,120 new cases of invasive breast cancer will be diagnosed among women in the United States (7). While mortality rates due to breast cancer within the US have been consistently falling over the years, rates of incidence have been on the rise (7). This rise in incidence means that an increasing number of follow-up patient investigations will be performed, increasing the case-load for pathology labs. Effective treatment strategies for breast cancer patients require timely diagnosis and prognosis of the disease. It has been reported that, in the US, the 5-year average survival rates for patients with invasive breast cancers increase from 90% to 99% when the disease is detected at a localized (non-metastatic) stage (8). In addition, for difficult and borderline cases there still exists disagreement between pathologists as to what the patient diagnosis should be (9, 10). In this context, tools that improve on the standard histopathology method in terms of speed, sensitivity, specificity and timely diagnosis and treatment are vital for mitigating the burden of disease.

Standard histopathology of breast tissue involves microscopic examination of a stained tissue biopsy by a trained clinical pathologist. These biopsies are surgically obtained after the patient shows an abnormality during a screening procedure such as X-ray mammography. A number of tissue preparation steps occur between surgical extraction and pathologist evaluation. The tissue is dehydrated, fixed in formalin and embedded in paraffin. The resulting processed tissue is referred to as formalin fixed and paraffin embedded (FFPE) tissue (11). Next, thin sections

of tissue (4-5 μm) are prepared by serial sectioning of the tissue block using a microtome, in preparation for staining. Staining of tissue is a vital component of the processing since cells and tissues neither absorb nor scatter light significantly, leading to poor contrast under a conventional microscope, in the absence of staining. The most commonly used stain in a pathology lab is hematoxylin and eosin (H&E). The stain was first discovered in 1876 by Wissowzky and remains to this day the most commonly used contrast mechanism during histopathology (12). Hematoxylin stains the cell nuclei blue/purple whereas eosin stains proteins within tissue pink thus generating contrast for the cell cytoplasm as well as the extra-cellular matrix (13). After staining, the tissue section is examined under a microscope by a pathologist who looks for morphological abnormalities indicative of disease. If the presence of disease is suspected, a parallel section of tissue is stained with immunohistochemical (IHC) markers for converging to a final diagnosis. IHC staining has a higher specificity than H&E and can therefore be used to answer specific questions regarding tissue pathology (14).

This standard tissue assessment method has a number for shortcomings. First, the pathologist evaluation relies on qualitative information, which means that there can be inter-observer variation during microscopic examination (9, 15). This is particularly challenging for borderline and difficult cases since, in the absence of quantification, agreement on the patient diagnosis is difficult to achieve. Second, the investigation is manual which leads to lower throughput that can potentially be achieved through automated or computer-aided analysis. Finally, the tissue preparation, especially stain intensity, can vary from lab to lab as well as from specimen to specimen (16-18). While trained pathologists are able to account for the resulting variations in image contrast, automated analysis through supervised learning schemes is made difficult in the absence of consistent image feature values (19). Even though a whole field, referred

to as “Digital Pathology”, has emerged out of the efforts to automate analysis of H&E stained tissue images, stain normalization is still an active area of research due to the lack of clear agreement on the best practices (20).

Another key challenge in breast pathology is tumor heterogeneity (21, 22). Breast tumors are more varied than other solid tumors resulting in large variations in responses to treatments between patients. For example, a number of breast cancer patients respond to hormonal therapies that target hormone receptors (HER2, estrogen and progesterone receptors) expressed by cells undergoing malignant transformation. However, for a molecular sub-type referred to as triple negative breast cancer, these therapies fail due to the absence of the hormone receptors in the cells being targeted (23). For these and other cases, pathologists rely on prognostic markers that are indicative of tumor aggressiveness and disease subtype. While effective in determining disease aggressiveness for a significant number of patients, due to disease heterogeneity, the current set of markers used for breast cancer prognosis (such as histological grade, hormone receptor status, Ki-67 expression) are not able to determine disease course for all patients (5, 24). There is a need for expanding on the current set of markers in order to better predict outcomes and to tailor therapies to the needs of individuals based on their prognostication (6). As ever, these markers need to be quantitative and the assessment rapid and reproducible in order to be effectively used in the clinic (24). New histological markers can potentially play an important role in this regard and represent an opportunity.

Novel quantitative, label-free microscopy techniques can potentially address these limitations of/opportunities in standard histopathology of breast tissue. Relying on intrinsic contrast that is related to physical property of the tissue, these methods remove subjectivity from tissue assessment by relying on quantitative information (3). In addition, inconsistency in image

pixel values due to variations stain intensity, choice of white balancing method and illumination source variations are also minimized in label-free microscopy. This makes it easier to design and train machine learning classifiers that are able to rely on features that are consistent between training and deployment (25, 26). Automated image analysis through such classifiers can, therefore, also potentially improve the throughput of investigation (26). In addition, since these methods rely on new and different contrast mechanisms to those used in conventional microscopy, they can aid in the development of new image based markers (as yet unknown in traditional histopathology) for expanding on the current set of prognostic markers (5). A key design challenge in these new imaging modalities is compatibility with the current clinical pipeline for breast histopathology. Clinical translation will be difficult for modalities that require significant changes in the current method in terms of sample preparation and additional instrumentation.

QPI is a quantitative microscopy modality which generates contrast by mapping the optical path-length variation across the tissue specimen (27). In most cases QPI systems are built as add-on modules to commercial microscopes and require minimal modifications in the current clinical diagnostic pipeline with regards to tissue processing and optical instrumentation. These systems also provide diffraction limited resolution and sub-nanometer sensitivity to tissue optical path-length changes (27). Although a number of other imaging modalities have been developed and applied for quantitative histopathology, QPI has advantages over them in terms of resolution, speed and compatibility with the standard workflow in a pathology lab (see Section 2.5 for a detailed comparison of the different quantitative microscopy techniques used for histopathology).

In this thesis, I have attempted to use QPI to address the above-mentioned challenges/opportunities in histopathology of the breast. Making developments in both

instrumentation and computational tools, I have investigated a number of questions related to breast cancer diagnosis and prognosis as outlined below.

1.2 Thesis Overview

This thesis is organized as follows. In Chapter 2 I provide an introduction to QPI, touching on the operating principle and the detection method. I also provide a comparison of QPI with other quantitative imaging techniques being used for tissue evaluation and review previous applications of QPI in clinical pathology. In Chapter 3, I discuss the application of QPI for qualitative evaluation of breast tissue. This is followed by Chapter 4 where this evaluation is conducted using quantitative markers and a supervised learning scheme for detecting malignancy in breast tissue images is introduced. In Chapter 5 I discuss a proof-of-principle study where we demonstrated that QPI can be used for detecting orientation of collagen fibers in breast tissue. The tools we developed in this work have applications in developing imaging markers for breast cancer prognosis. In Chapter 6, the imaging of stained tissue using QPI is introduced and it is demonstrated that the diagnostic and prognostic markers (shown to be effective in the earlier chapters on unstained tissue) are extendable to QPI maps of stained tissue. I end my thesis with Chapter 7 which explores the future questions that can be addressed in the field of breast histopathology using QPI, employing the instruments and algorithms developed in this thesis work.

Chapter 2: Quantitative Phase Imaging (QPI)

2.1 Introduction

Transparent specimen such as cells and tissues do not absorb or scatter light significantly and, thus, are difficult to resolve using intensity based detectors (such as CCD cameras, photodetectors, the human eye etc.)(28). One option for imaging such specimen is to generate exogenous contrast by using dyes and fluorescent molecules. However, not only do exogenous agents result in variability from sample to sample but fluorescence can lead to photo-toxicity and photo-bleaching (29). In 1942, Nobel laureate Fritz Zernike developed the phase contrast microscope, which generated *intrinsic* contrast in images by leveraging the phase of the electromagnetic field (30). While widely adopted by microscopists world-wide for label-free imaging, phase contrast images only provide qualitative information. The field of QPI was born out of attempts to quantitate the contrast generating mechanism in phase contrast microscopy.

The interaction of light with transparent specimen (such as cells and tissues) involves a change in the phase of the electromagnetic field with respect to some reference. This phase shift is proportional to the integral, along the light propagation direction, of the difference between the refractive index of the specimen and that of the surrounding medium. Denoting the light propagation direction as the z-axis, the phase map $\phi(x,y)$ is given by

$$\phi(x,y)=\frac{2\pi}{\lambda}\int_{0}^{h(x,y)}[n_s(x,y,z)-n_m]dz \tag{2.1}$$

where $n_s(x,y,z)$ is the refractive index of the specimen as function of space, n_m is the refractive index of the surrounding medium, λ is the wavelength of the illumination source and the integration limits span the thickness of the specimen $h(x,y)$ (27, 31).

Over the years, a number of studies have shown that the refractive index of a cell, $n_{cell}(x,y)$, has a strong dependence on its total protein concentration $\Psi(x,y)$. This relationship is given by

$$n_{cell}(x,y) = n_{sol} + \nu\,\Psi(x,y) \tag{2.2}$$

where n_{sol} is the refractive index of the cytoplasmic solvent and proportionality constant ν is called the refractive increment (31-34). Since for most applications the difference between the refractive index of the cytoplasmic solvent and the cell immersion media is negligible ($n_0 \approx n_{sol}$) it can be shown that the cell dry mass density $\Sigma(x,y)$ is proptional to the phase map $\phi(x,y)$ as (31, 32, 35)

$$\Sigma(x,y) = \frac{\lambda}{2\pi\nu}\phi(x,y). \tag{2.3}$$

These remarkable results have motivated several studies on cell-cycle dependent growth, dynamics of intracellular transport as well as chemical composition of cells though measurement of $\Sigma(x,y)$ and $\Psi(x,y)$ using QPI (31, 35-39). The work presented in this chapter is based on the work in Ref. (31).

2.2 Detection: Off-axis and phase shifting interferometry

Bright field microscopes, generally used in pathology, are only able to measure the intensity of the electric field. This is because all detectors (CCD, CMOS, retina) produce signals that are proportional to the time averaged magnitude square of the electric field and, as a result, fail to capture the phase information (28, 40, 41). QPI systems on the other hand generally exploit

spatial or temporal interferometry that can then be used to obtain both the magnitude and phase information of the image field.

Systems employing spatial interferometry are known as *off-axis* interferometers because they involve interference between the sample wave $U_s(x,y)$ and a plane wave reference U_r that is incident at an angle δ to the sample wave propagation direction. This process is illustrated in Fig. 2.1 (a). The two waves interfere at the detector plane and the resulting intensity distribution or interferogram is given by

$$I(x,y)=\left|U_s(x,y)\right|^2+\left|U_r\right|^2+2\left|U_r\right|\left|U_s(x,y)\right|\cos[\left(qx+\phi(x,y)\right] \tag{2.4}$$

where $q=\frac{2\pi}{\lambda}\sin\delta$ is the modulation frequency. $\phi(x,y)$ can be extracted from the acquired interferogram in two different ways depending on the specifics of the optical setup. In the first method, $I(x,y)$ is measured at a conjugate image plane so that $U_s(x,y)$ represents the in-focus complex image field. In such a case, $\phi(x,y)$ can be obtained from the interferogram by first isolating the cross term in Eq. (2.4) using band-pass filtering and then taking the Hilbert transform of the result, as detailed in ref. (42). In a variant of this method, the camera is placed at a distance d from the conjugate image plane in which case $U_s(x,y)$ is the out-of-focus image field. In this case the complex image field associated with the object is obtained by first extracting $U_s(x,y)$ from $I(x,y)$ through the same process as in the first method and then obtaining the focused image field by numerically propagating $U_s(x,y)$ through a distance d by convolving with a Fresnel wavelet (43-45). $\phi(x,y)$ can then be obtained as the argument of the in-focus image.

Systems employing temporal interferometry are referred to as *phase-shifting* interferometers. In these systems, the phase difference between the sample wave $U_s(x,y)$ and the reference wave $U_r(x,y)$ is changed or shifted. Various devices can be used for this purpose [mobile mirror, liquid crystal phase modulator (LCPM), acousto-optic modulator etc.]. This interaction is illustrated in Fig. 2.1 (b). Denoting this tunable phase shift by φ, the resulting interferogram at the detector plane is given by

$$I(x,y;\varphi) = |U_s(x,y)|^2 + |U_r|^2 + 2|U_s(x,y)||U_r|\cos[\phi(x,y) - \varphi]. \tag{2.5}$$

Unambiguous determination of $\phi(x,y)$, using phase-shifting interferometry, requires four different modulations (four frames). A common choice is to use $\varphi = 0, \frac{\pi}{2}, \pi, \frac{-\pi}{2}$ to acquire these four frames which can then be used to determine $\phi(x,y)$ as

$$\phi(x,y) = \tan^{-1}\left[\frac{I\left(x,y;-\frac{\pi}{2}\right) - I\left(x,y;\frac{\pi}{2}\right)}{I(x,y;0) - I(x,y;\pi)}\right]. \tag{2.6}$$

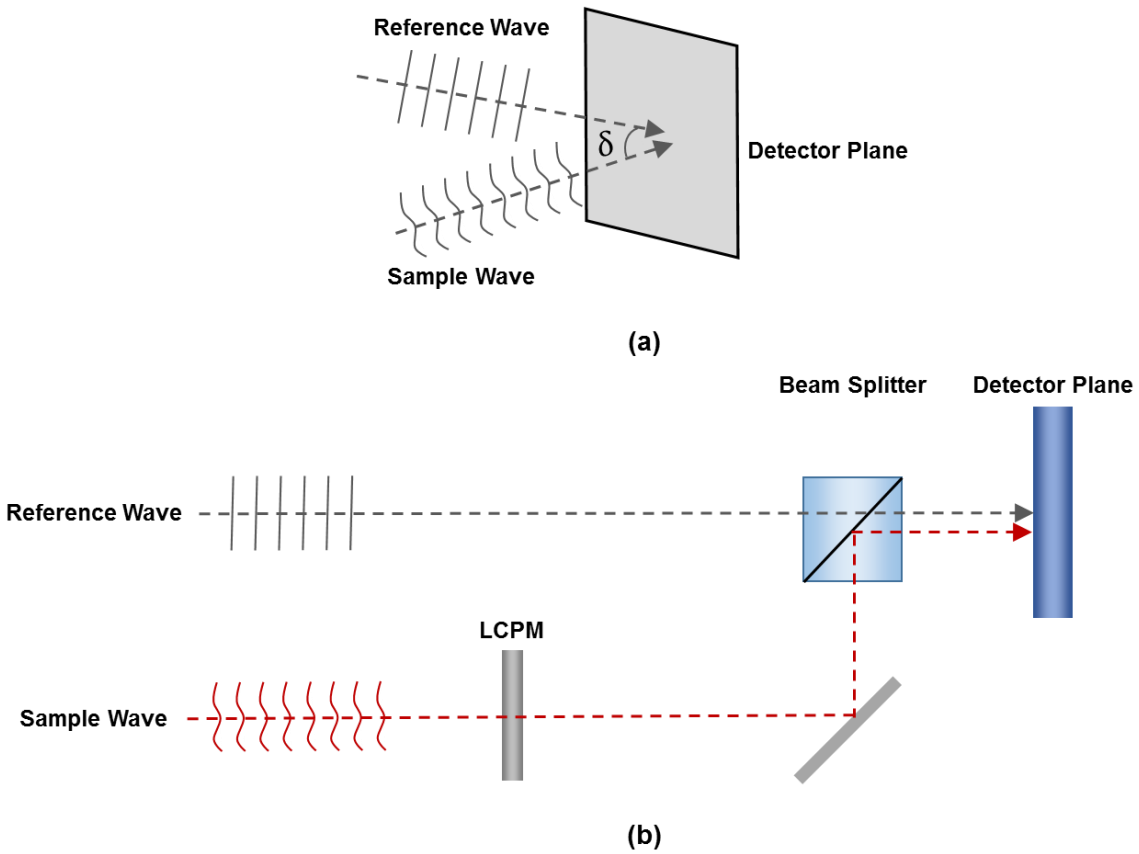

Figure 2.1 Principles of interferometric detection in QPI: **(a)** Off-axis interferometry **(b)** Phase-shifting interferometry. LCPM: Liquid Crystal Phase Modulator.

Both off-axis and phase-shifting interferometry have their respective advantages and disadvantages that influence their adoption in various applications. Off-axis systems allow single-shot measurements, therefore, improving the achievable acquisition rate over phase-shifting systems. However, these systems have coherence and spatial sampling requirements that result in smaller fields-of-view and lower resolutions than comparable phase-shifting interferometers (46, 47). For the investigations discussed in this thesis, a phase shifting interferometer called SLIM has been used. SLIM combines the space-bandwidth advantages of phase-shifting interferometers with other merits, discussed below.

2.3 Spatial Light Interference Microscopy (SLIM)

Among phase-shifting interferometers, SLIM has had a number of applications for label-free quantitative histopathology (see Section 2.4). Figure 2.2 illustrates the SLIM optical setup which has been discussed in detail in previous publications (48, 49). The setup comprises of a module (CellVista SLIM Pro, Phi Optics, Inc.) coupled to the output port of a commercial phase contrast microscope (in this thesis research Carl Zeiss, Axio Observer Z1 was used). This compatibility with existing microscopes promises to reduce barriers to clinical adoption since optical microscopes are commonly available in pathology labs. In the SLIM module, the conjugate image plane outside the microscope is relayed onto a sCMOS camera (Andor, Zyla) using a 4f system comprising lenses L_1 and L_2. At the Fourier plane of L_1, a spatial light modulator (SLM, Boulder Nonlinear Systems) is used to modulate the phase difference between the scattered and unscattered components of light in increments of $\pi/2$. Four different modulations are applied [Fig. 2.2 (b)] and the resulting phase image is reconstructed as discussed in ref. (48). Using a software platform developed in-house, the SLIM module has been upgraded with full-slide scanning capabilities (50, 51). The scanning speed of the SLIM imaging system can be assessed by comparing it with that of a commercial slide scanner. For example, the Zeiss Axio Scan.Z1 slide scanner is able to scan a 15x15 mm^2 area, at 0.22 μm/pixel sampling rate, in 240 s. The SLIM system scans the same area at 0.125 μm/pixel in 1638 s. Scanning at the same resolution as the Zeiss instrument would improve the speed of the SLIM system by a factor of $(0.22/0.125)^2$ = 3.1, to 528s (51). Thus, our SLIM scanner is only a factor of 2.2 slower than the commercial Zeiss scanner, which is remarkable, especially considering that we record 4 intensity images for each SLIM image.

Since SLIM relies on the same microscope optics as standard histopathology, the transverse resolution of the two systems is the same. Being a common-path, white-light based system (27), SLIM offers a spatial sensitivity of 0.28 nm and temporal sensitivity of 0.029 nm in terms of OPD (48). For histopathology, this implies that subtle (nanometer scale) changes in tissue OPD are detectable, which are correlated with on-set of malignancy and prognosis, as demonstrated in later chapters.

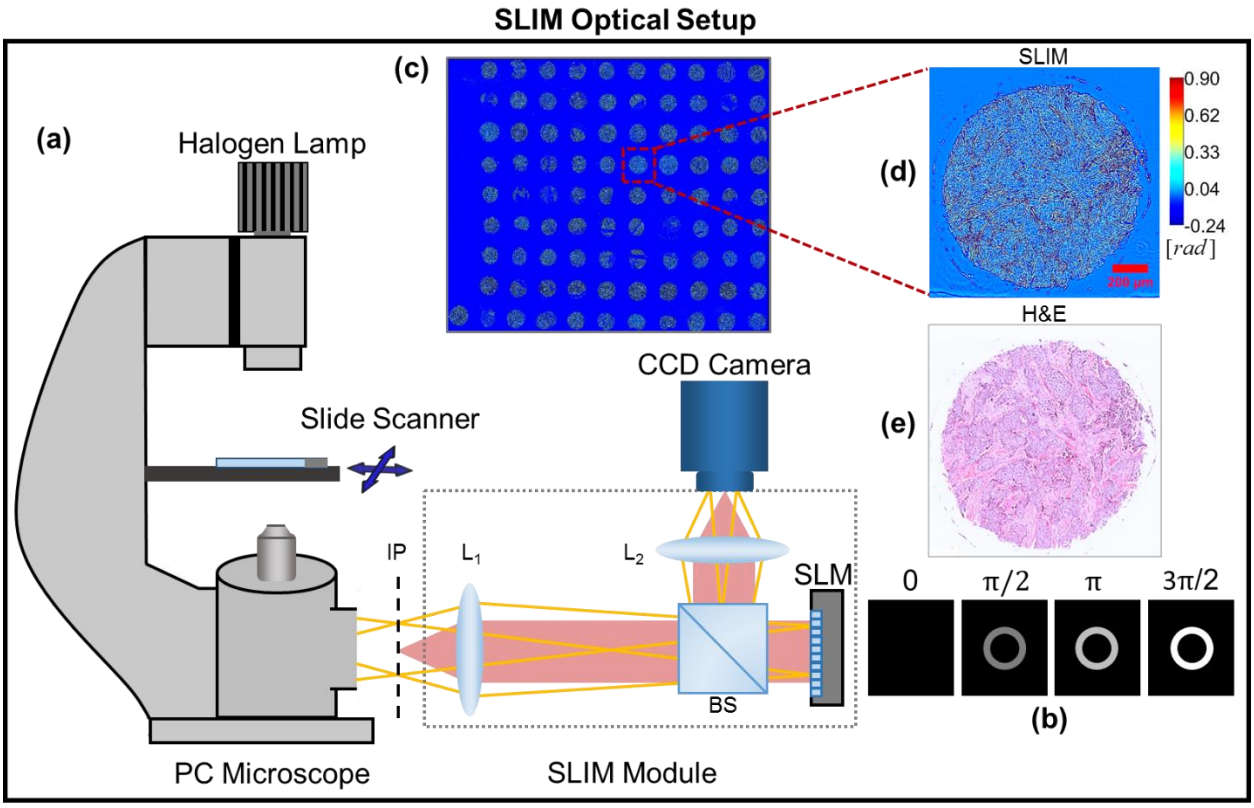

Figure 2.2 (a) The SLIM module added on to a commercial phase contrast microscope. **(b)** Four frames are acquired to compute one phase image by modulating the phase difference between scattered and incident light using a spatial light modulator (SLM). **(c)** An image of the whole slide scanned using SLIM. **(d)** Example of a TMA core SLIM image. **(e)** Bright field image of the same core after H&E staining. BS, beam splitter; L_1-L_2, lenses; IP, image plane.

2.4 Previous work on quantitative histopathology using QPI

Quantitative phase images of tissue biopsies report on the OPD across the tissue specimen (Eq. 2.1). OPD of tissue describes its nanoscale architecture which can be expected to vary between healthy and diseased tissue as well as between different disease types. This has motivated several histopathological investigations of different organs using QPI which I briefly review here.

A majority of these studies have focused on diagnosis i.e separating diseased and normal tissue. In (52) Wang *et al.* showed that the median and mode of SLIM phase images vary significantly between benign and malignant prostate tissue. They also reported that phase images are able to generate contrast for calcium oxalate micro-calcifications in breast tissue. These calcifications are important for a pathologist to detect from a clinical point of view but are not visible on standard H&E stained bright-field images. In (53), an off-axis QPI technique called Hilbert Phase Microscopy (HPM) was used to extract phase images of healthy and diseased mouse liver tissue. Using refractive index maps extracted from these phase images, by assuming constant known tissue thickness (see Eq. 2.1), the authors showed that the spatial standard deviation of these maps was significantly different between normal liver tissue and liver tissue with lysosomal storage disease. Refractive index maps, extracted using a QPI technique called Spatial Low-coherence Quantitative Phase Microscopy (SL-QPM), were also used by the authors of (54) to show that malignant breast epithelial cells have on average higher refractive index than benign breast epithelial cells. Takabayashi *et al.* showed, once again using SLIM, that normal breast tissue has a smaller ‘disorder strength’ than malignant breast tissue (55). This parameter was once again measured using QPI-derived refractive index maps and is inversely related to the strength of tissue scattering (55). QPI images have also been used for diagnosing colorectal cancer. In (50), the

authors used the median phase value of each gland within colorectal tissue, imaged using SLIM, to separate benign, dysplastic and malignant cases.

While (55) and (54) have characterized differences in refractive index and scattering between benign and malignant breast tissue, a formal model for automated, supervised classification of diseased and non-diseased cases, using QPI, has as yet not been reported and is one of the aims of this thesis research.

On the prognosis front, Sridharan *et al.* used SLIM images of prostate tissue biopsies to investigate how the scattering properties of tissue vary between patients having recurrence and non-recurrence after prostatectomy (56). Their analysis showed that scattering anisotropy, measured from phase maps using the scattering phase theorem (57), was higher in non-recurrent cases compared to recurrent cases. Nguyen *et al.* used SLIM phase maps of prostate tissue biopsies to come up with a model for classifying tumors according to their Gleason grade. They used supervised learning to automate the process of tumor scoring (25). In a study focused on determining the future risk of developing colorectal cancer, the authors in (58) generated depth-resolved OPD maps of tissue biopsies using SL-QPM. Using statistical parameters measured from these maps, they separated patients at high risk of developing colorectal cancer from those at low risk. To our knowledge, little to no work has been done on breast cancer prognosis using QPI, which is one of the aims of this thesis research.

2.5 Competing label-free quantitative microscopy techniques

A number of other label-free contrast generating mechanisms have been proposed in the past for quantitative histopathology. The three mostly widely used ones are: Fourier Transform Infra-Red Spectroscopic (FTIR) imaging, Raman Spectroscopic (RS) imaging and SHGM. In this

section, we briefly compare and contrast these techniques with QPI, highlighting their relative merits and demerits.

FTIR relies on the difference in absorption spectra across the tissue specimen to generate contrast. The absorption spectra vary for different tissue components due to their different chemical compositions and, thus, different molecular vibrational modes (3, 59). In this way FITR imaging provides chemical specificity and multidimensional data and has been used for probing both diagnostic and prognostic questions related to prostate (3, 60), colon (61, 62) and breast cancer (63, 64). However, compared to conventional light microscopy FTIR has lower resolution and throughput. In addition, it faces challenges in terms of compatibility with the current diagnostic pipeline: both sample preparation and instrument optics vary significantly from those used in conventional microscopy. A separate dedicated scanner would need to be deployed if FTIR based disease markers are needed as a complement to traditional histopathology.

RS imaging measures the frequency shift caused by inelastic light scattering due to unique molecular vibrational and rotational modes within different tissue components (65). Like FTIR it has the advantage of providing multidimensional spectral information with chemical specificity. Quantitative histopathology using RS imaging has been used for many studies including breast (66, 67) and bladder cancer diagnosis (68) as well as investigation of esophageal dysplasia (69). However, like FITR, RS imaging is slower than standard bright-field imaging and requires a specialized tissue scanner as well as different specimen preparation.

SHGM generates contrast in the tissue image by measuring light emitted by non-linearly active, non-centrosymmetric materials such as collagen. In these materials, two lower energy photons are up-converted to a single photon at twice the incident light frequency (70). In this way SHGM provides specificity to collagen in tissue, generating high contrast images that map out the

extracellular matrix organization. It has been used for tumor microenvironment investigations of breast (5, 71), pancreatic (72) and ovarian cancers (73). In addition to its specificity to collagen, SHGM also has the advantage that a standard H&E stained histology can be used as the sample. However, SHGM has lower throughput than conventional bright-field microscopy and would, once again, require a separate scanner/instrument if it were to be deployed as a histopathology tool in the clinic. In addition, since contrast in SHGM is generated only in non-cellular structures, the tumor edge cannot be discerned from the SHGM image and other modalities (such as bright-field H&E images) need to be combined with it in order to answer clinical questions.

In contrast with these methodologies, QPI is not as specific since contrast is generated in all structures that have a refractive index difference from their surroundings (27). However, QPI provides similar resolution and speed as standard histopathology and, especially in the case of SLIM, can be added-on as a functionality to microscopes already in existence in pathology labs. Thus far, the key barrier to clinical translation in QPI has been the need for an unstained tissue sample for histopathological analysis. This need poses additional sample preparation requirements in a clinic - if a pathologist needs QPI markers in addition to H&E based markers, they need to prepare a separate sample for QPI. It is, therefore, one of the aims of this thesis to demonstrate that QPI can also be performed on standard H&E stained histology to provide both phase maps and bright-field images in a single scan (Chapter 6).

CHAPTER 3: Breast cancer diagnosis using QPI – Qualitative Assessment

3.1 Abstract

As discussed earlier, the standard practice in histopathology of breast cancers is to examine an H&E stained tissue biopsy under a microscope to diagnose whether a lesion is benign or malignant. This determination is made based on a manual, qualitative inspection making it subject to investigator bias and resulting in low throughput. Hence, a quantitative, label-free and high throughput diagnosis method is highly desirable. We present in this chapter preliminary results showing the potential of QPI for breast cancer screening and help with differential diagnosis. We generated phase maps of unstained breast tissue biopsies using SLIM. As a first step towards quantitative diagnosis based on SLIM, we carried out a qualitative evaluation of our label-free images. These images were shown to two pathologists who classified each case as either benign or malignant. This diagnosis was then compared against the diagnosis of the two pathologists on corresponding H&E stained tissue images and the number of agreements were counted. The agreement between SLIM and H&E based diagnosis was 88% for the first pathologist and 87% for the second. Our results demonstrate the potential and promise of SLIM for quantitative, label-free and high throughput diagnosis.

3.2 Motivation and overview

As described in Chapters 1 and 2, quantitative histopathology of the breast is key to improving patient health outcomes as it provides an objective and potentially automatable basis for diagnosing disease. Thus, a QPI based diagnosis method can potentially improve on the current gold-standard of microscopic examination of stained tissue in terms of objectivity and throughput and provide additional information for difficult cases. In this chapter we present preliminary results that show the potential of a SLIM based technique for diagnosis of breast cancers. Specifically, the resolution and contrast of SLIM phase images for diagnostic purposes were evaluated qualitatively by two board certified pathologists. As outlined in detail in the following sections, using the standard H&E staining based diagnosis protocol as a benchmark, the success of the pathologists in carrying out diagnosis on SLIM images was measured. Our results provide an indication of the signal to noise ratio available to us for subsequent quantitative analyses for carrying out diagnosis based on the relative phase values of various tissue components. The work presented in this chapter is based on the work published in ref. (51).

3.3 Experimental procedures

3.3.1 TMA

The samples consisted of a TMA of cores constructed from breast tissue biopsies of 400 different patients. Each biopsy was formalin fixed and paraffin embedded before sectioning it into slices of 4 μm thickness each, using a microtome. Two parallel, adjacent sections were selected from each biopsy and one of these sections was stained using H&E, leaving the other one unstained. Cores were then constructed for both the stained and unstained tissue and these were mounted on separate slides after de-paraffinization, using xylene as the mounting medium. The

stained samples were imaged used a bright field microscope and their images served as a reference for evaluating diagnosis on the unstained samples using SLIM. The slides were obtained from our collaborating pathologist at the University of Illinois at Chicago (UIC) Dr. Andre Balla. The procedures used in this study for conducting experiments using human subjects were approved by the Institute Review Board (IRB) at the University of Illinois at Urbana Champaign (IRB Protocol Number 13900).

3.3.2 Slide scanning and mosaicking

The TMA was imaged using our SLIM imaging system (Figure 2.2), equipped with a 40x/0.75 NA phase contrast objective. A slide scanning software, developed in-house in Visual C++, was used to obtain the raw images for the entire microscope slide (scanning area approx. 20 mm x 45 mm) at high throughput (approx. 2 hrs per slide).

The phase maps were extracted from the acquired intensity images using a MATLAB-based code. A C++-based code was used for stitching the mosaic for the entire slide and segmenting out each individual core for subsequent processing and analysis. As shown in Figure 3.1, our processing allows the visualization of the entire TMA from the slide scale to the sub-cellular scale within each core. As illustrated in Figure 3.1 (c), our label-free SLIM images clearly delineate the epithelial stromal boundary allowing for assessment of tumor malignancy.

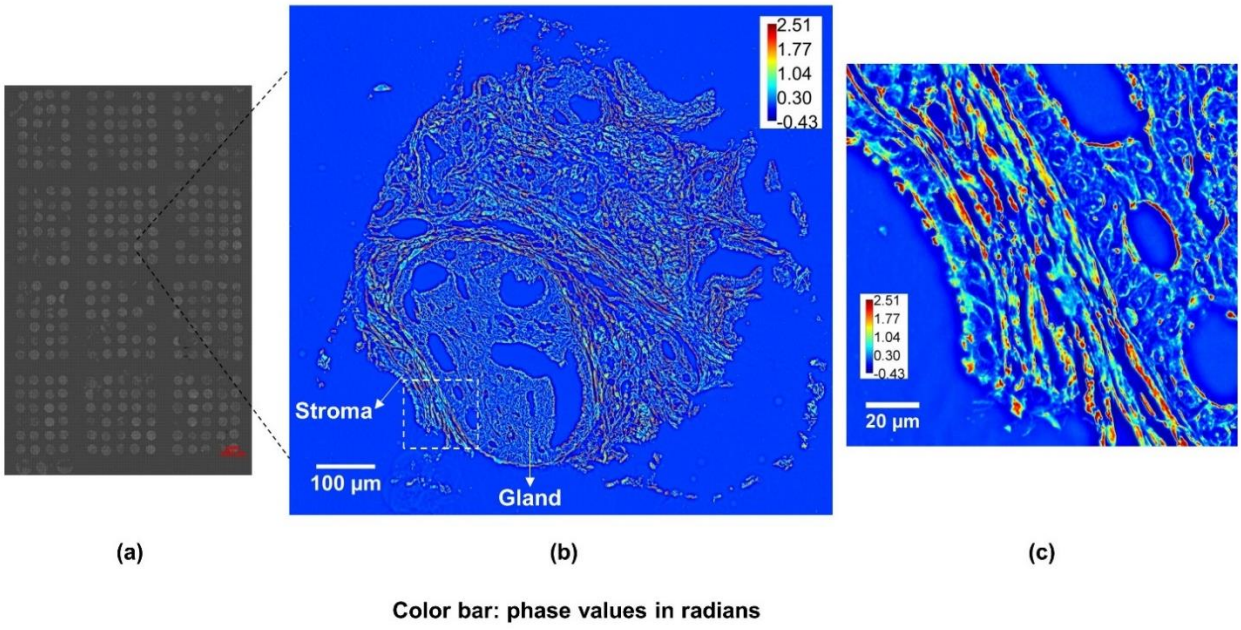

Figure 3.1 (a) The SLIM image of an entire TMA slide (20 mm x 45 mm) scanned and stitched using software developed in-house. **(b)** Label-free SLIM image of a single TMA core delineating the boundary between the tumor and its extracellular environment. **(c)** Magnified image of region indicated in (b) clearly showing tumor cell nuclei and collagen fibers, specific to epithelial and stromal regions.

3.3.3 Pathologist training procedure

In order to assess the diagnostic capabilities of our SLIM imaging modality, we asked two board certified pathologists to evaluate our SLIM images. For this preliminary study, we selected 109 cores for evaluation and stacks of both SLIM and corresponding H&E images for these cores were assembled in ImageJ. Since pathologists are generally trained to recognize morphological features in H&E stained tissue, we performed a training step before the actual test. In this training step, out of the total cohort of 109 cores, 10 benign and 10 malignant cores (classified as such by a third board certified pathologist *a priori*) were chosen and their SLIM and H&E images were shown side by side to each pathologist. By comparing the SLIM and H&E images for each core, the pathologists were able to learn how to interpret the tissue morphological details from SLIM

phase maps. The total training time for each pathologist ranged from 10 – 15 minutes, approximately.

Figure 3.2 compares and contrasts how different tissue components are resolved in SLIM and H&E stained tissue images. Due to the fact that our system uses phase contrast illumination, SLIM images inherit some of the halo artifact that is characteristic of phase contrast images. This effect is due to the fact that some of the high spatial frequency components pass through the low spatial frequency or D.C region (ring) in the Fourier plane [Fig. 2.2 (c)]. As a result, negative phase values are observed at sharp edges in the SLIM phase images. Since the study presented here is based on visual interpretation of SLIM images by pathologists, the halo artifact does not affect our results because, as illustrated in Figure 3.2, the tissue morphology is not obscured by the presence of the halo artifact. Typically, for quantitative studies based on measuring physical parameters, we use halo removal algorithms developed in house to recover halo free quantitative phase images (74, 75)

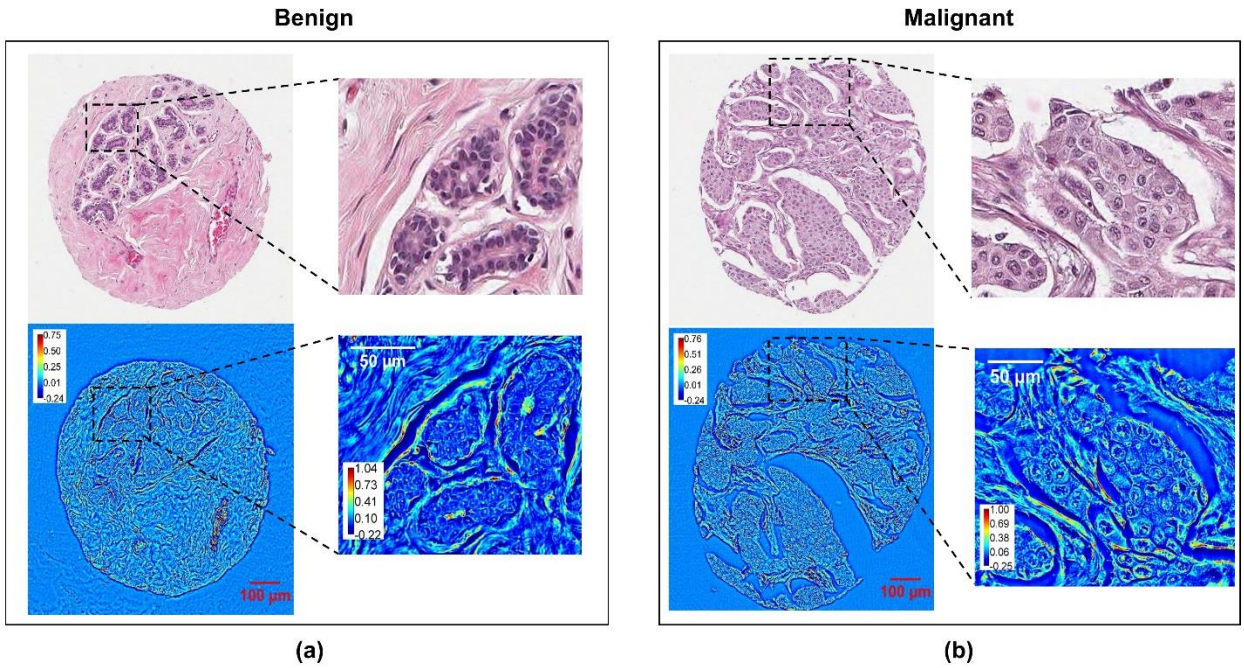

Figure 3.2 Comparison between H&E stained bright field microscopy (top row) and SLIM (bottom row) images in their respective abilities to resolve tissue morphology for **(a)** benign and **(b)** malignant cases. The H&E images were obtained from stained sections that were adjacent to the unstained sections used for SLIM imaging. Color bars are in radians.

3.3.4 Pathologist diagnosis using SLIM

After the completion of the training step, at the testing stage, each pathologist was first shown the stack of SLIM images for all of the 109 cores chosen. The pathologist classified each core as either benign or malignant. The process was repeated for the stack of H&E images for the same 109 cores. Using each pathologist's diagnosis on the H&E stained cores as the gold standard, the success of diagnosis using SLIM images was measured by counting the number of agreements between SLIM and H&E based diagnoses. The entire exercise is schematically depicted in Figure 3.3.

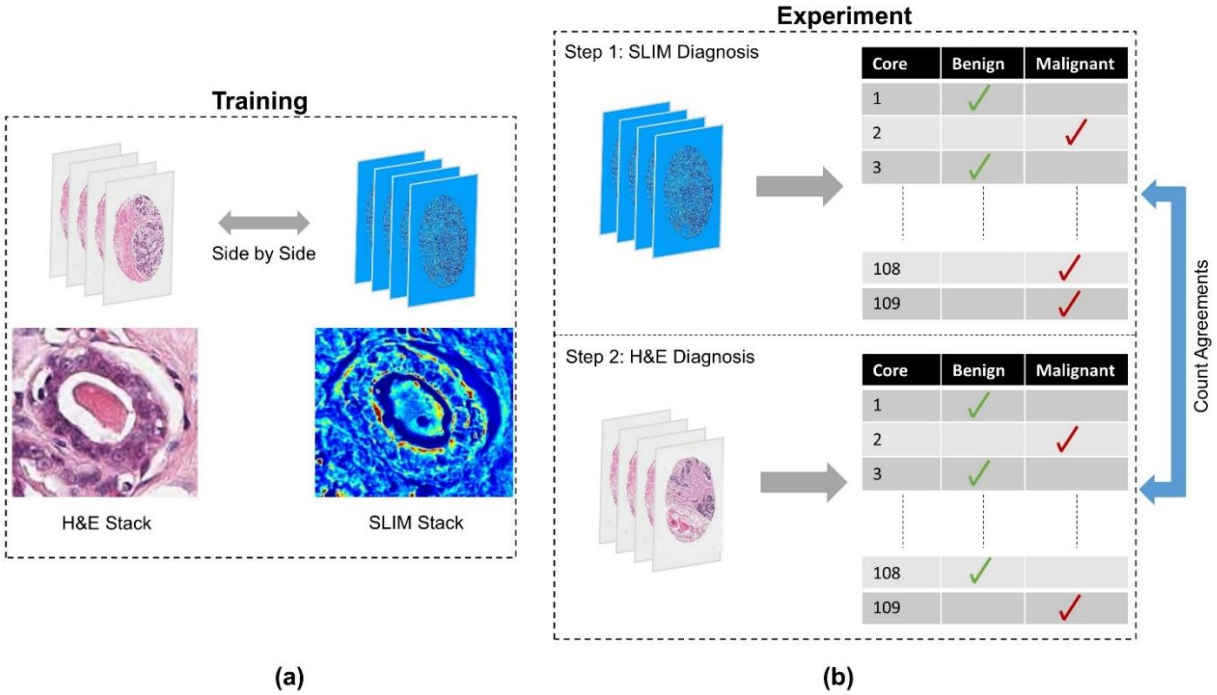

Figure 3.3 Diagnosis using SLIM images by pathologists and comparison with H&E based diagnosis. **(a)** The training step was performed prior to the experiment. For 20 cores out of the cohort of 109 cores in total, both SLIM and H&E images were shown side by side to each pathologist, training the pathologist to interpret morphology from SLIM images by comparing features with corresponding H&E images. **(b)** For the entire 109 core cohort, each pathologist classified a core as either benign or malignant by looking at their SLIM images. The process was repeated for H&E images and number of agreements between the two diagnoses were counted for each pathologist.

3.4 Results

The results of the core classification carried out by the two pathologists on both SLIM and H&E images are summarized in Figure 3.4. As shown in Figures 3.4 (c) and (d), the success rate of diagnosis on SLIM images (considering diagnosis on H&E as the gold standard) for pathologist 1 was 88% and that for pathologist 2 was 87%. As shown Figures 3.4 (a) and (b), the agreement between the two pathologists when rating SLIM images stood at 83% whereas the same for H&E images was much higher at 98%. The lower agreement between the two pathologists on SLIM images is not surprising when one takes into account the fact that, as part of their professional

training, pathologists are trained to interpret images of H&E stained tissue for a number of years whereas, for this experiment, the training time for SLIM images was only a few minutes. We expect the agreement between the diagnoses of the two pathologists on SLIM images to increase significantly with longer training in interpreting SLIM images.

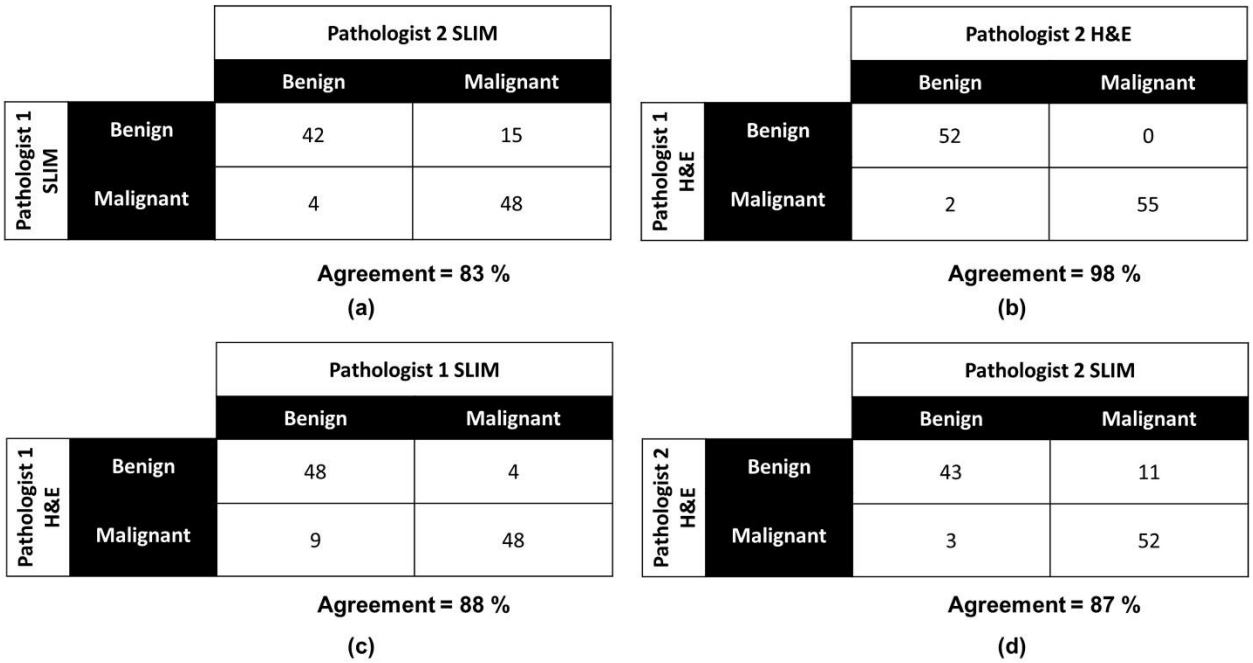

Figure 3.4 Confusion matrices showing results of qualitative diagnosis carried out by two pathologists on both SLIM and H&E stained tissue images for 109 cores. **(a)** Pathologist agreement on SLIM images. **(b)** Pathologist agreement on H&E images. **(c)** and **(d)** Agreement between ratings on SLIM and H&E images for each pathologist.

3.5 Summary and Conclusion

The preliminary results discussed in this chapter show the capability of our label-free imaging modality of resolving morphological features relevant for diagnosis of breast cancer. While this qualitative analysis is promising, the actual research aim in this thesis is to leverage the tissue physical properties extracted by SLIM for quantitative analysis. This is addressed in Chapter 4, for which the results of chapter 3 provide motivation - all that remains is to come up with the

appropriate feature extraction and supervised learning method in order to detect quantitative markers of malignancy automatically.

CHAPTER 4: Breast cancer diagnosis using QPI – Quantitative Assessment

4.1 Abstract

Building on the evidence shown in the last chapter that SLIM images resolve morphological markers of malignancy we present in this chapter a *quantitative* method for label-free breast tissue evaluation using SLIM. We rely on scattering, geometric and texture-based features, extracted from OPD maps of breast tissue. We demonstrated our method by imaging a TMA consisting of 68 different subjects - 34 with malignant and 34 with benign tissues. Three-fold cross validation results showed a sensitivity of 94% and specificity of 85% for detecting cancer. Our disease signatures represent intrinsic physical attributes of the sample, independent of staining quality, facilitating classification through machine learning packages since our images do not vary from scan to scan or instrument to instrument.

4.2 Motivation and Overview

To date, a majority of quantitative image analyses on breast tissue biopsies have relied on color images of stained tissue. Image classification in these cases has involved computing a wide range of histological features including geometric features (76, 77), texture-related features (78, 79) and radiometric features (78) (80, 81) [see (19) for a review of methods]. However, the feature extraction process relies heavily on tissue staining which can vary from sample to sample and instrument to instrument, affecting the robustness of the classifier (82). We present in this chapter a label-free QPI based approach which makes classification through machine learning easier since the instrument does not require calibration for inconsistency in pixel values due to variations in staining, tissue changes caused by harsh solvents etc. These advantages of QPI have already been leveraged to develop supervised learning methods for classifying erythrocytes infected with *Plasmodium falciparum* (83) and non-activated lymphocytes (84).

We demonstrate the quantitative analysis capabilities of our tissue evaluation system by imaging a TMA comprising 68 different cases (34 benign and 34 malignant). For each epithelial region (ER) within a tissue core, we extracted scattering, geometric, and texture-related markers of tissue malignancy from the SLIM maps (see Section 4.3 Materials and Methods). A linear-discriminant analysis (LDA) classifier was trained to separate benign cases from malignant cases and three-fold cross validation was performed to measure the classification accuracy of the learned model (85, 86). Using validation by the Receiver Operating Characteristic (ROC) curve analysis, our results revealed a sensitivity of 94% and specificity of 85%. Our results are the first demonstration, to our knowledge, of using OPD based tissue markers for detecting malignancy in breast tissue, label-free. The work presented in this chapter is based on the work published in ref. (87).

4.3 Materials and Methods

4.3.1 SLIM optical system

We used the SLIM imaging system for this study, the working principle of which was described earlier in Section 2.3. Throughout our experiments, a 40x/0.75 NA phase contrast objective was used for imaging. At this sampling rate (6.2 pixels/μm), the typical time for imaging a single tissue core (1 mm^2 area) was approximately 12 sec.

4.3.2 TMA

The TMA used for our study was purchased from US Biomax Inc. (Serial # BR-1002) with diagnosis for each case provided by the manufacturer through examination by a board certified pathologist. The TMA was obtained with all human subject information de-identified. Neither the authors of this work nor their institutions were involved in the collection of tissue. The TMA consisted of cores 1 mm in diameter and a section thickness of 5 µm. Standard FFPE histological preparation was used for each tissue block before extraction of cores. A xylene based mounting medium was used during cover-slipping.

The TMA consisted of 36 cases of infiltrating ductal carcinoma (IDC), 36 cases of tumor adjacent normal tissue and 10 cases of normal breast tissue derived from autopsy procedures (one core per case). Three of the tumor adjacent normal cores were obtained from the IDC cohort. The TMA was designed to mix approximately equal numbers of histologically normal and histologically invasive carcinoma cases. The post-mortem interval for autopsy cases was less than 6 hours and after assembly the TMA was inspected for quality control and diagnosis by the manufacturer through review by a board certified pathologist. For final analysis we selected 34 cores diagnosed as malignant and 34 cores diagnosed as normal (within which 28 were tumor adjacent normal and 6 were normal). Each of these final cores were selected based on whether the

core was intact and whether any epithelial tissue was present in the core (cores containing only stromal tissue were excluded).

A SLIM image of the whole TMA slide is illustrated in Fig. 2.2 (c). Figs. 2.2 (d) and (e) show, respectively, the phase map and the H&E stained tissue bright field image (henceforth referred to as 'H&E image') of one core. For obtaining a mosaic of the TMA, we used a C++ based stitching code, developed in-house (50). After staining the same tissue slide using standard protocols (13), H&E images of the TMA were acquired using a bright-field microscope (Carl Zeiss, Axio Observer Z1) outfitted with a color camera (Carl Zeiss, Axiocam MRC). The H&E images were used for qualitative evaluation only, to assist with annotation of epithelial regions in tissue, discussed below.

4.3.3 Annotation of epithelium in tissue images

Each gland or continuous ER within each core was manually annotated using the region of interest (ROI) tool of ImageJ to allow feature extraction for each ER. A consistent criterion for annotation was used where groups of epithelial cells bounded by stroma on all sides were considered a single ER. Other tissue components within epithelium (such as lumen etc.) were considered part of the ER if bounded on all sides by epithelial cells. ERs from cores in the cancer cohort were labelled as malignant while those from cores in the normal cohort were labelled as benign.

4.3.4 Extraction of geometric and scattering features

Malignant transformation in breast tissue affects the size, shape and density of epithelial cells as well as the shape and organization of epithelial tissue. As a result, both the geometry and scattering properties of an ER (tumor) are affected. We used ER perimeter curvature C, as well as the mean scattering length l_s as part of the feature set used for separating benign and malignant

tissue. The parameter extraction process is illustrated in Fig. 4.1 and a detailed description for each is provided below.

The extrinsic curvature C of a two-dimensional plane curve $\Gamma(x,y)$, that is parametrized by Cartesian coordinates $x(s)$ and $y(s)$ with parameter s, is given by the expression (88)

$$C(s)=\frac{|x'y''-y'x''|}{\left(x'^2+y'^2\right)^{\frac{3}{2}}}, \tag{4.1}$$

where the x', y' and x'', y'' refer to the first and second derivatives in s, respectively. In the above parametrization, s refers to each pixel comprising the curve $\Gamma(x,y)$, having coordinates $x(s)$ and $y(s)$. This curvature can be interpreted as the magnitude of the rate of change of a vector tangent to $\Gamma(x,y)$. We computed C for the perimeter $\Gamma(x,y)$ of each annotated ER by using an open source MATLAB code (89). The code approximates $\Gamma(x,y)$ as a polygon before computing C for each point defining the ER perimeter, as described in Eq. (4.1). To speed up computation, the image of each core was first down-sampled from the raw image size of 8000 x 8000 to 2048 x 2048 pixels. The sampling rate in the down-sampled image was 1.59 pixels/μm and a bi-cubic interpolation technique was used for down-sampling. The perimeter $\Gamma(x,y)$ was then further down-sampled by a factor 20 (every 20th pixel was analyzed) before computing $C(s)$ in order to remove any pixel level errors due to manual annotation. The median ER curvature $\langle C \rangle$ was then used as a feature for separating benign and malignant cases. Figs. 4.1 (c) and (d) illustrate $\langle C \rangle$ for representative benign and malignant ERs.

The scattering mean free path l_s, is a bulk scattering parameter that defines the length scale over which a single scattering event occurs on average. Assuming that the tissue slice captures the

refractive index spatial fluctuation statistics, i.e., assuming statistical homogeneity, l_s can be computed through the *scattering-phase theorem* using the expression (57)

$$l_s = \frac{L}{\text{var}[\phi(x,y)]}, \tag{4.2}$$

where $\phi(x,y)$ is the SLIM phase image, L is the tissue section thickness and the operator $\text{var}[.]$ computes the spatial variance over a region. The l_s parameter has been used in the past for discriminating between benign and malignant prostate tissue (52). We first computed the image $l_s(x,y)$ from the phase image $\phi(x,y)$ (8000 x 8000 pixels) using a variance filter kernel size of 149 x 149 pixels, which equals the approximate diameter of 3 epithelial cells. The feature $\langle l_s \rangle$ was then computed by calculating the median of $l_s(x,y)$ over the ER area. This computation is illustrated in Figs. 4.1 (e) and (f).

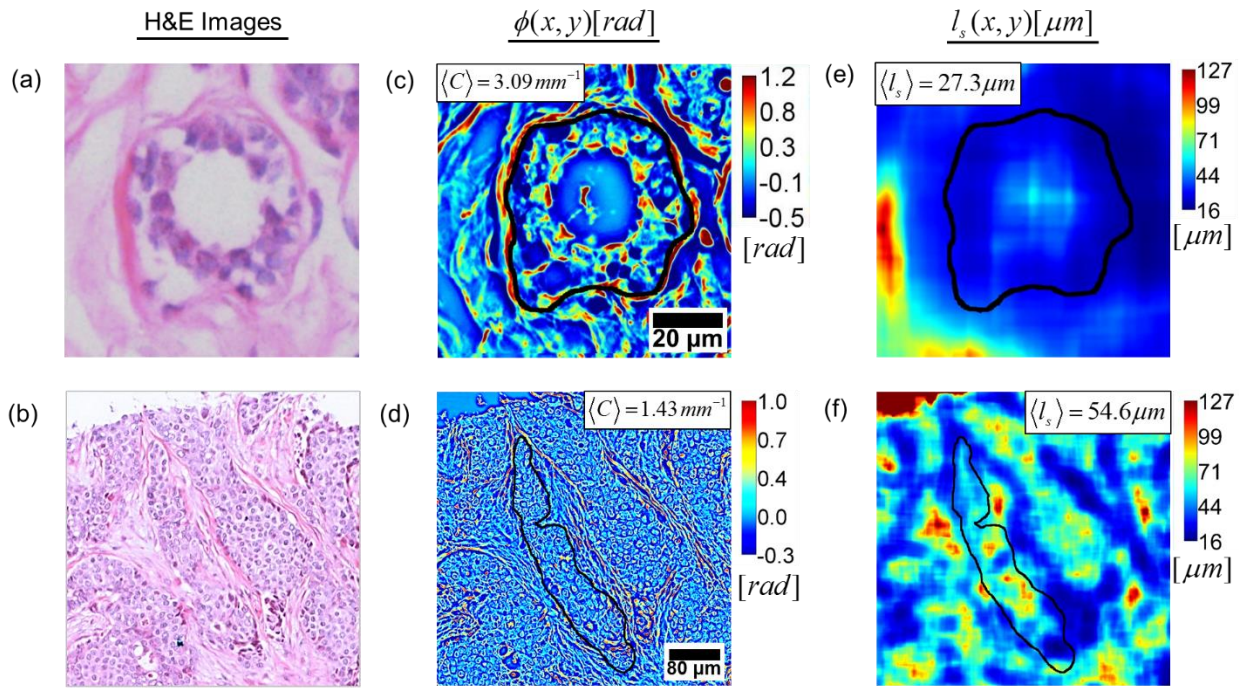

Figure 4.1 Computing the geometric feature $\langle C\rangle$ and scattering feature $\langle l_s\rangle$ over each annotated ER. **(a)** and **(b)** H&E images of benign and malignant ERs, respectively. **(c)** and **(d)** SLIM images of the same benign and malignant ERs, respectively, illustrating ER curvature C. The median over ER $\langle C\rangle$ is used as the geometric feature for classification. **(e)** and **(f)** $l_s(x,y)$ for benign and malignant ERs, respectively. The median over ER $\langle l_s\rangle$ is used as the scattering feature for classification.

4.3.5 Extraction of texture-related features

Benign and malignant epithelial tissues differ not only in cell morphology but also in the organization of their components, leading to different textures. Texture-related features have been used in the past for solving different classification problems in histopathology of cancers (19, 25). Our feature extraction follows the work done by Varma *et al.* (90) for classifying different materials based on their texture. The approach is illustrated in Fig. 4.2. Each TMA core phase image was first down sampled to 2048 x 2048 pixels from 8000 x 8000 pixels [Fig. 4.2 (a)]. A bi-cubic interpolation was used for down-sampling and the sampling rate in the down-sampled image was 1.59 pixels/ μm. The down-sampled core image was then filtered through a convolution with

the Leung-Malik (LM) filter bank [Fig. 4.2 (b)]. This filter bank consists of gradient filters (both odd and even) at different orientations and spatial scales (91) . In total, 58 different filters were used, generating a 58-dimensional response vector for each pixel in the core phase image [Fig. 4.2 (c)]. The response vectors from ERs within each core were then randomly sampled (10000 vectors per core) to generate a smaller dataset for further processing. K-means clustering was then performed on the response vectors (number of clusters, K = 50) sampled from all cores within each training set (see Results and Discussion) and the computed cluster centroids were referred to as 'textons' (90, 91). K = 50 was chosen iteratively by repeatedly measuring the cross-validation AUC (see Results and Discussion, Section 4.4) and determining the number of clusters required to maximize it (to account for both overfitting and separation accuracy). Since each pixel in each core belongs to a texton, for each pixel the histogram of textons was generated for its vicinity (window size 60 x 60 pixels) and was used to characterize the local texture in that neighborhood. This way, a 50 dimensional feature vector T was generated to characterize texture in a pixel's neighborhood. An open source MATLAB code was used for generating the LM filter bank for this work (92).

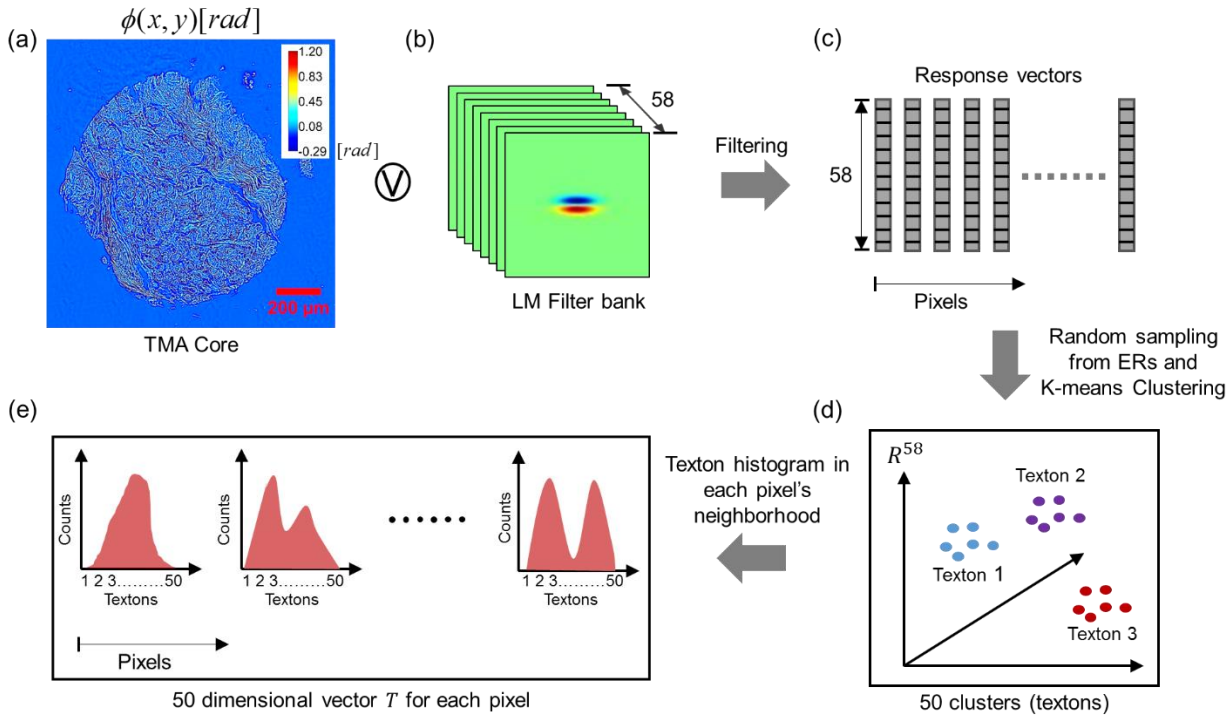

Figure 4.2 Algorithm for computing the texture in a pixel's neighborhood. **(a)-(c)** Generating the response of each pixel to an LM filter bank. **(d)** K-means clustering of response vectors, generated from all cores in the training set, in order to find 50 cluster centroids or textons. **(e)** Histogram of textons, within a pixel's neighborhood, comprise the texture-related feature vector T for each pixel.

4.3.6 Classifier training and validation

Since our work involves classifying each tumor within a tissue core as benign or malignant, a feature vector for each ER was next generated by concatenating geometric, scattering and texture-related features. This procedure is illustrated in Fig. 4.3. After pixel-wise computation of ER curvature C, scattering length l_s and texture vector T, the median of each feature was computed over each ER in a core and a combined 52 dimension feature vector was generated for training. For each ER, this feature vector was then used as a predictor for training an LDA classifier [Fig. 4.3 (a)]. Class labels, either benign or malignant, were used as the ground-truth for each ER during the training process. All ERs within cores deemed cancerous by the pathologist were labelled malignant and all ERs within cores deemed normal were labelled benign.

The feature extraction for validation purposes, illustrated in Fig. 4.3 (b), followed a nearly identical procedure to that used during training. The only difference was that, instead of finding new textons (cluster centroids) for validation data, the texture feature vector T was computed by using the same textons as determined during training. As in training, a 52 dimensional feature vector was input to the LDA classifier which then used the model learned during training to generate a likelihood score for an ER being benign or malignant. Finally, the mean of the likelihood scores of all ERs within a core was computed and used as the likelihood score of a core being benign or malignant. These scores were then used to generate an ROC curve to select an operating point for separating benign and malignant cases (see Results and Discussion). For an annotated test core the total time required by our algorithm to generate a core likelihood score was approximately 2 minutes. This is in the absence of any parallelization of the computation through graphics processing unit (GPU) implementation which can significantly boost the computational throughput.

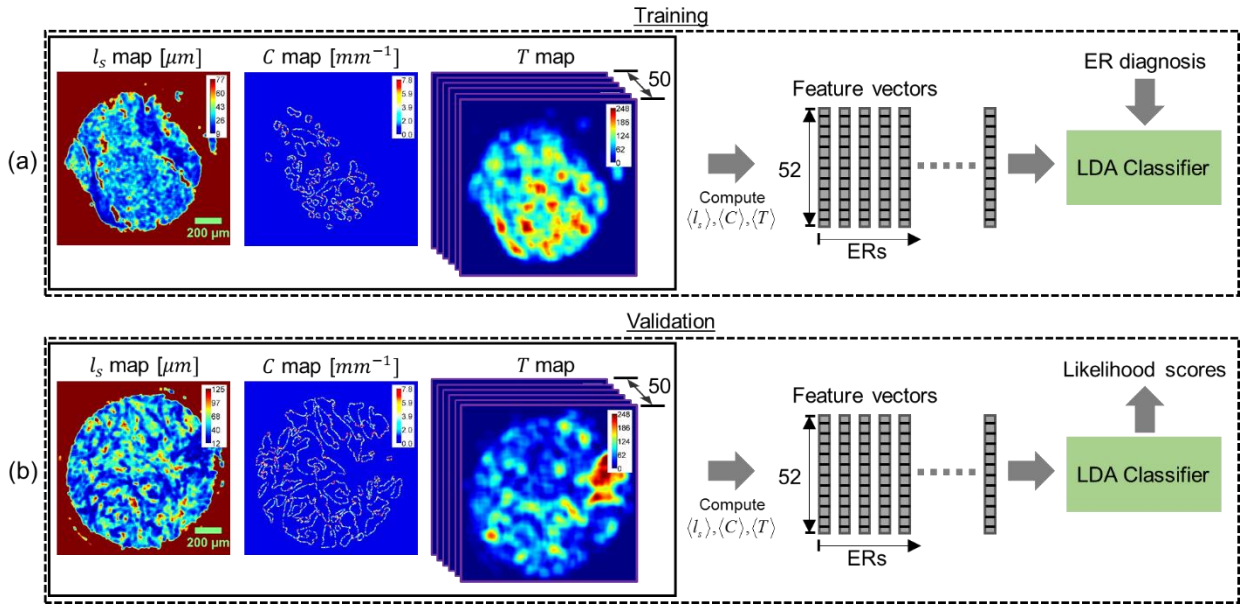

Figure 4.3 (a) Training and **(b)** Validation procedure for classifying ERs as benign or malignant.

4.4 Results and Discussion

The classification results of our analysis are summarized in Fig. 4.4. In order to evaluate the accuracy of our method, we performed three-fold cross-validation (93) as illustrated in Fig. 4.4 (a). The total number of cases were divided into three (nearly) equal groups. In each trial, two groups were used for training while the remaining one was used for validation. Thus, three validation trials were performed, each time selecting a different validation/training set combination.

Figure 4.4 (b) illustrates the separation between benign and malignant ER feature vectors in one training set. In order to illustrate the data separation in 3 dimensions, we use principal component analysis (PCA) and represent the 50-dimensional feature vector $\langle T \rangle$ through its first principal component PC1 $\langle T \rangle$. The training space shows that scattering feature $\langle l_s \rangle$ has on average higher values for malignant ERs than for benign ERs. This finding is compatible with typical ER morphology in breast tissue since benign ERs are well differentiated, consisting of a number of

different structures including epithelial cells, lumen and myoepithelial cells (94). This heterogeneity of structure results in short mean scattering lengths as explained by a large variance in Eq. (4.2). Malignant ERs on the other hand consist of a monoclonal proliferation of cells, sometimes even showing sheets of poorly differentiated epithelial cells, resulting in smaller variance and larger l_s values (94). These phenomena can also be observed in the examples given in Figs. 4.1 (e) and (f). In previous investigations on prostate cancer, it was shown that l_s has a lower value in malignant tissue than in benign tissue (52). That analysis, however, was carried out on larger areas of tissue where cellular organization can be different from the epithelial only regions we are studying in this work (52).

The median ER curvature $\langle C \rangle$, on the other hand, generally has higher values for benign ERs than for malignant ERs. This is a result of the fact that the edge of a benign ER is constrained to follow a round or elliptical shape due to tubule formation [Figs. 4.1 (a) and (c)] (94). When malignant transformation occurs, this constraint is broken and the ER edge is more irregular. At the spatial scale of investigation we have used here (approx. 13 μm), the perimeter of the malignant ER is less rapidly varying, on average, than that of a benign ER. This geometric feature is similar to the previous measurement of the ER perimeter fractal dimension that has been used for histopathology (19, 76).

Fig. 4.4 (c) shows the separation between benign and malignant ERs in the validation feature space, where, qualitatively, the same separation trend is seen as in training. We show the results of only one of the three validation trials that were carried out. As described in Materials and Methods, the ER likelihood scores, generated by the classifier during validation, were averaged over each ER in order to obtain core-wise or case-wise scores. The standard deviation of ER likelihood scores, within each core, had a mean value of 0.18, a median value of 0.19 and a

maximum value of 0.41 for the benign dataset (i.e across 34 cores). The same for the malignant dataset (again across 34 cores) were 0.17, 0.17 and 0.37, respectively. This indicates that the malignant cores consisted primarily (if not entirely) of malignant ERs since the variance of ER likelihood scores over them was similar to that over benign cores, which consisted entirely of benign ERs. In addition, while we treated all ERs within cancerous cores as malignant during training, removing any benign tissue from malignant cores, during classifier training, is likely to improve our accuracy rather than worsen it.

The core-wise likelihood scores from the 3 trials were then pooled together to generate the ROC curve illustrated in Figure 4.4 (d) (95). Our results indicate an area under the curve (AUC) of 0.91. The optimum operating point for classification was determined by using the standard method of assigning equal weight to the cost of misclassifying positives and the cost of misclassifying negatives (96). This resulted in a sensitivity of 0.94 and specificity of 0.85 for the three-fold cross validation. When the same analysis was repeated by using the median rather than the mean of the ER scores over each core (to get a case-wise score), it resulted in an AUC of 0.91 and sensitivity and specificity of 0.94 and 0.82, respectively. While we use the standard method for determining the operating point here (which assigns equal cost to false negatives and false positives) in principle any operating point along the ROC curve can be chosen depending on the application (e.g 0.97 sensitivity and 0.77 specificity). Having said that, the higher sensitivity of 0.94 is useful since it results in a smaller number of false negatives than false positives. Minimizing false negatives is more important than minimizing false positives since the latter only result in further investigations of the patient whereas the former constitute a missed diagnosis. A sensitive method is also useful in situations where a small biopsy specimen is available and detection of small amounts of malignant tissue visually is a challenge for the pathologist.

Our results are significant because they are the first illustration of tissue OPD derived features being used to detect intrinsic markers of malignancy in breast tissue, using supervised learning. While previous works employing image analysis and supervised learning for detecting cancerous regions in H&E-stained tissue images have demonstrated good classifications AUCs (greater than 0.90) (19, 76, 97, 98), accounting for stain variation through normalization remains a challenge (82) due to a lack of universal agreement on the correct normalization method (19). Our label-free results, thus, eliminate an important factor affecting consistency of results between different samples and instruments whilst maintaining high sensitivity and specificity.

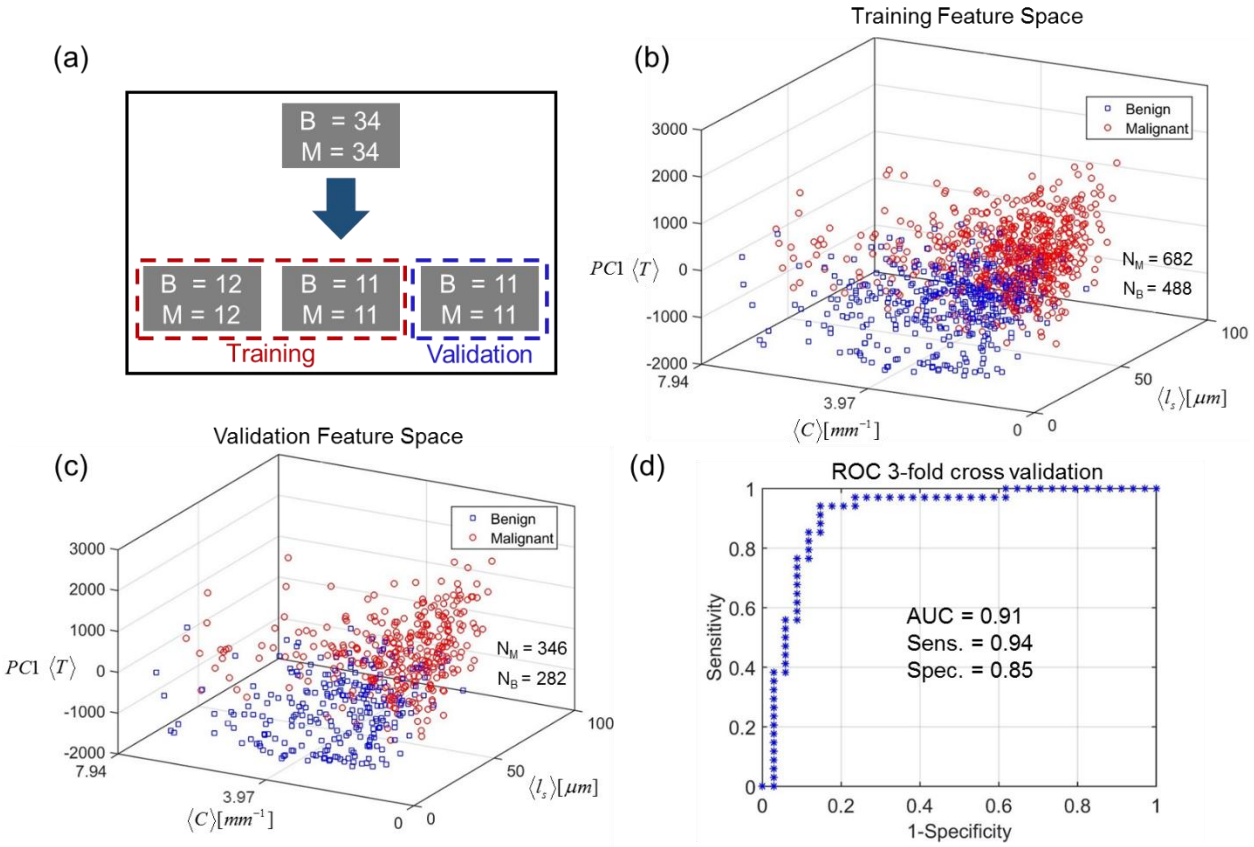

Figure 4.4 (a) Three-fold cross-validation procedure for evaluating classification accuracy. **(b)** Separation of benign and malignant ER feature vectors during *training* in 1 of 3 validation trials. **(c)** Separation of benign and malignant ER feature vectors during *validation* in 1 of 3 validation trials. **(d)** ROC curve for the 3 validation trials resulting in a sensitivity of 0.94 and specificity of 0.85 at the optimum operating point.

4.5 Summary and Conclusions

In summary, we presented in this chapter a new method for quantitative evaluation of tissue biopsies obtained from patients under investigation for breast cancer. Since our method relies on measurement of OPD maps, an intrinsic property of tissue, the basis for classification is objective and not subject to inter-observer variation. In the past much of quantitative histopathology has relied on analysis of stained tissue. However, stain variability continues to remain a grand challenge in applying computer algorithms across multiple H&E stained specimens. This fact is

well documented in the literature, as follows. In ref. (99), it is stated that: “On the technical side, one of the main challenges in the computational interpretation of digital slide images has to do with color variations in the tissue induced by differences in slide preparation, staining, and even whole slide scanners. Clearly decision support algorithms that aim to work on digital pathology images will have to contend with and be resilient to these variations.” In ref. (20) the authors state that “One of the major difficulties in breast cancer histopathology image analysis, particularly of H&E stained sections, is appearance variability.” As a final example, ref. (100) states “It is clear that an integral part of digital pathology that has yet to be resolved is colour standardization; in order to do so, further work is needed focusing upon fine-tuning colour calibration methods in relation to the effect on diagnosis.”

Although OPD depends on tissue slice thickness which can vary slightly from section to section, previous studies on colorectal and prostate cancer, using SLIM, have indicated that variations in OPD due to cutting errors are insignificant (50, 101). These studies looked at the variation of median phase values and anisotropy in scattering between tissue slices having the same nominal thickness and reported insignificant differences. Despite this preliminary evidence, future studies where variation in our feature set is explicitly tested against tissue slice thickness variation are required. While in this work we have performed manual segmentation of epithelium, the automation of the entire process (including segmentation) is feasible and subject to future efforts.

While our cross-validation results show promising sensitivity and specificity, a number of further studies are proposed before clinical adoption of our method. First, our analysis needs to be further tested with separate training and testing tests, the latter being obtained from an independent laboratory and remaining unused during model development. Second, our feature set needs to be

applied to more clinically difficult cases since making frank benign versus frank malignant diagnoses is not currently a serious challenge for pathologists. However, our results demonstrate an important and necessary first step and we propose to apply our feature set, in future studies, to more challenging cases such as stratification of benign lesions as well as distinguishing ductal carcinoma in situ (DCIS) from benign atypical hyperplasia (BAH) (102, 103). Third, while we have applied our diagnosis method to cases of IDC, the most widely prevalent form of breast cancer, the applicability of the model to other histological sub-types (such as infiltrating lobular carcinoma) also needs to be explored.

While other label-free diagnosis methods have been proposed for these types of investigations, they affect the standard diagnostic pipeline in terms of either speed, resolution or compatibility with established workflow. SLIM, on the other hand, requires minimal changes to a conventional microscopic optical train due to its modular design. Even though in this study a research grade microscope was coupled to the SLIM module, in principle SLIM can be used with any phase contrast microscope. Furthermore, the SLIM instrument is less expensive than most commercial tissue scanners. Our results, although preliminary, are an important stepping stone towards extracting reliable novel markers that can provide pathologists adjunct information to H&E based markers for assessing difficult cases. In addition, computational pathology tools such as ours can help pathologists where the biopsy specimen is small and highly sensitive detection is desired.

CHAPTER 5: Quantifying collagen fiber orientation in breast tissue using QPI

5.1 Abstract

Tumor progression in breast cancer is significantly influenced by its interaction with the surrounding stromal tissue. Specifically, the composition, orientation and alignment of collagen fibers in tumor-adjacent stroma affects tumor growth and metastasis. Most of the work done on measuring this prognostic marker has involved imaging of collagen fibers using SHGM, which provides label-free specificity. Here we show that SLIM is able to provide information on collagen-fiber orientation that is comparable to that provided by SHGM. Due to its wide-field geometry, the throughput of the SLIM system is much higher than that of SHGM and, because of the linear imaging, the equipment is simpler and significantly less expensive. Our results indicate that SLIM images can be used to extract important prognostic information from collagen fibers in breast tissue, potentially providing a convenient high throughput clinical tool for assessing patient prognosis.

5.2 Motivation and Overview

As explained earlier in Chapter 1, prognostic markers provide clinicians with important information about disease aggressiveness, cancer sub-type and expected patient outcomes (4). This allows these clinicians to make treatment decisions that best suit a patient's disease state and avoid over-treatment (6, 24). Current markers, such as histological grade, hormone receptor status, tumor size etc., while useful for most patients, do not accurately predict outcomes for all patients. Thus, there is a need to expand on the current prognostic markers to account for biological variation among individuals (5, 6).

The role of adjacent stroma in mediating breast tumor initiation, progression, and invasion to surrounding tissue has been extensively discussed over the years (104-108). Tumor invasion into surrounding healthy tissue involves breaking down of the basement membrane and a desmoplastic response in the stroma. This response involves an increase in density of the extracellular matrix (ECM), marked by increased deposition of collagen, as well as recruitment of stromal cells (e.g. fibroblasts and inflammatory cells) to facilitate tumor growth (5, 105, 106). Using both mouse and in vitro models of mammary tissue, studies have also concluded that tumor progression is marked by re-alignment and re-orientation of collagen fibers (5, 109-111). For example, Conklin *et al.* showed that the Tumor Adjacent Collagen Signature 3 (TACS3) correlates with lower disease-free and disease-specific survival in breast cancer patients (5, 112). TACS3 refers to the histological marker involving aligned collagen fibers that are oriented perpendicularly to the tumor edge (5).

As described in Chapter 2, SHGM has emerged as a powerful technique for imaging collagen fibers in breast cancer adjacent stroma with sub-cellular resolution (113). SHGM measurement of the prognostic signature TACS3 was reported in ref. (5). Ambekar *et al.* used

Fourier analysis on SHGM images to show that the collagen fibers in breast biopsies are more aligned in malignant *vs.* pre-malignant and benign tissue (71). Riching *et al.* used SHGM to image 3D collagen gels to elucidate specific epithelial cell-fiber interactions that are responsible for enhancing tumor progression along aligned fibers in breast tissue (114). Other researchers have used image segmentation and machine learning tools to extract prognostic information from SHGM images of collagen fibers (115, 116).

SHGM maps the second-order non-linear susceptibility $\chi^{(2)}$ associated with *non-centrosymmetric* molecules and thus probes fibrillar collagen structures with specificity (113). As detailed in Section 5.3, collagen generates a strong second-harmonic signal compared to the surrounding cellular structures, resulting in high imaging contrast (117). However, the low contrast of other cellular structures in SHGM images means that the tumor boundary is difficult to delineate and often other imaging modalities are required (116). Furthermore, since SHGM systems employ a laser point-scanning geometry, the imaging throughput is low and whole slide scanning of breast cancer tissue sections remains a tedious task.

In this chapter, we show that SLIM, in conjunction with basic image segmentation, is able to provide information on collagen-fiber orientation and alignment similar to that obtained using SHGM. In addition, SLIM generates contrast for epithelial cells as well, which can be used to detect tumor boundaries. Furthermore, compared to SHGM, the SLIM images are acquired at much higher throughput due to the wide-field geometry. Using both SLIM and SHGM, we imaged a TMA of breast biopsy cores consisting of both benign cases and malignant cases at different stages of the disease. Using the Fourier analysis method described in Section 5.5 we show that both SLIM and SHGM images generate similar histograms of fiber orientation angle.

This chapter is organized as follows. In Section 5.3, we present the theoretical foundation for extracting second-order nonlinear response from phase-resolved linear imaging. Section 5.4 describes the experimental details of the study, and Section 5.5 presents the results. Section 5.6 summarizes and discusses these results. The work presented in this chapter is based on the work published in ref. (118).

5.3 Theory

In this section we explain the theoretical motivation for using SLIM for collagen fiber analysis imaging by showing that the signal measured in SLIM is related to that measured in SHGM. The source of the signal measured in both modalities is the induced polarization $\boldsymbol{P}$. To the second-order approximation, this can be related to the fundamental (incident) field $\boldsymbol{E}$ as

$$\boldsymbol{P} = \chi^{(1)}(\omega)\boldsymbol{E} + \chi^{(2)}(2\omega)\boldsymbol{E}^2, \tag{5.1}$$

where $\chi^{(1)}$ is the first-order electric susceptibility, $\chi^{(2)}$ is the second-order nonlinear susceptibility and ω is the optical frequency of the source (119).

The physical quantity measured in SLIM is the spatially-resolved linear response, $\chi^{(1)}(\boldsymbol{r}) = n^2(\boldsymbol{r}) - n_0^2$ with n being the refractive index of tissue, n_0 the refractive index of the immersion medium, and $\boldsymbol{r} = (x, y)$. Note that for low refractive index contrast, $\chi^{(1)}$ simplifies to $\chi^{(1)}(\boldsymbol{r}) \approx 2n_0\left[n(\boldsymbol{r}) - n_0\right]$. The SLIM signal is the optical path-length map generated by the tissue slice

$$\phi(\boldsymbol{r}) = \beta_0 \left[n(\boldsymbol{r}) - n_0 \right] t$$

$$\approx \beta_0 \frac{\chi^{(1)}(\boldsymbol{r})}{2n_0} t \tag{5.2}$$

where $\beta_0 = 2\pi / \lambda$ is the wavenumber in vacuum, t the local thickness of tissue, and λ the wavelength of the illumination (27).

The physical quantity measured in SHGM is $\chi^{(2)}(2\omega)$, which relates to the SHG electric field $\boldsymbol{E}_{SHG}(2\omega)$ via (113, 119-121)

$$\boldsymbol{E}_{SHG}(2\omega) \propto \beta_0^2 \chi^{(2)}(2\omega) \boldsymbol{E}^2(\omega). \tag{5.3}$$

We can find a relationship between the $\chi^{(2)}(2\omega)$ and $\chi^{(1)}(\omega)$ signals measured by our two imaging methods by solving the equation of motion for the anharmonic oscillator describing microscopic charge displacement [see, for example, Section 1.4. in ref. (119)]. This leads to the expression

$$\left[\frac{2n_0}{\beta_0 t} \phi(\boldsymbol{r}, \omega) \right]^2 = \left[\chi^{(1)}(\boldsymbol{r}, \omega) \right]^2 = \frac{1}{A} \frac{\chi^{(2)}(\boldsymbol{r},\ 2\omega)}{\chi^{(1)}(\boldsymbol{r},\ 2\omega)}. \tag{5.4}$$

In Eq. (5.4), $A = \frac{a\epsilon_0^2 m}{N^2 e^3}$, where a is a constant that depends on the mechanical properties of the anharmonic oscillator model, N the volume density of electric dipoles in the medium, ϵ_0 is the permittivity of free space, m the mass of an electron and e the elementary charge. Equation (5.4) indicates that the second-harmonic response is proportional to the squared of the linear response, which is measured directly by SLIM, namely

$$\chi^{(2)}(\boldsymbol{r}, 2\omega) \sim \chi^{(1)}(\boldsymbol{r}, 2\omega) \phi^2(\boldsymbol{r}, \omega). \tag{5.5}$$

This relationship can then be used to re-write Eq. (5.1) in the form

$$\boldsymbol{P} = \chi^{(1)}(\omega)\boldsymbol{E} + \chi^{(1)}(2\omega)\phi^{2}(\omega)\boldsymbol{E}^{2}. \tag{5.6}$$

In Eq. (5.6) the linear term generates the SLIM signal and provides contrast in both centrosymmetric and non-centrosymmetric structures. The quadratic term accounts for the SHGM signal and generates contrast only in non-centrosymmetric structures (119). Since the quadratic term has a dependence on $\phi(x,y)$, we anticipate that in non-centrosymmetric regions (collagen fibers) SLIM and SHGM images provide similar morphological information. However, before a comparison between the two can be made, the centrosymmetric information in SLIM (linear imaging) needs to be extracted out. In this work, we extract this information out using image processing techniques as discussed in the Section 5.5.

5.4 Materials and Methods

5.4.1 The SHGM and SLIM imaging systems

The optical setups for the two imaging modalities are illustrated in Fig. 5.1. The operating principle for the SLIM system was outlined in Section 2.3. While that for SHGM has been detailed in previous publications (71, 122), here we briefly describe it.

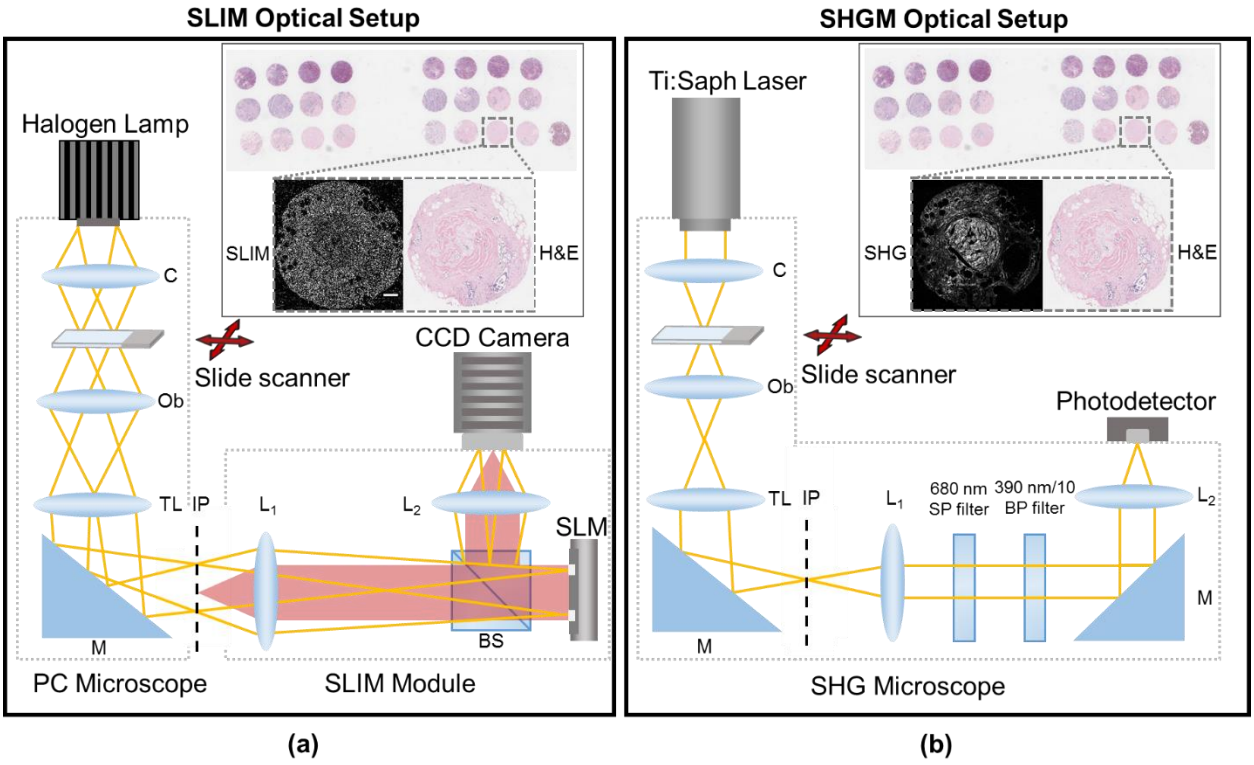

Figure 5.1 (a) Optical setup of the SLIM system, built as a module attached to the output port of a commercial phase contrast microscope. The insert shows an H&E image of TMA slide, as well as H&E and SLIM images of one of its cores. Scale bar: 200 µm. **(b)** Optical setup of the SHGM system. The insert shows an H&E image of the TMA slide as well as H&E and SHGM images of one of its cores. C, condenser. Ob, objective. TL, tube lens. IP, image plane. M, mirror. BS, beam splitter. SP, short pass. BP, band pass. SLM, spatial light modulator.

Figure 5.1 (b) illustrates the SHGM system. A Ti: Sapphire laser was used to produce 70-fs pulses at an excitation wavelength of 780 nm and a repetition rate of 80 MHz. The beam was scanned onto the sample, and focused by a 20x/0.8 NA air-illumination Zeiss condenser. The transmitted beam was collected in the forward direction by a 40x/0.9 NA Zeiss objective and then passed through two filters. The first filter was a 680 nm short-pass filter (680 nm/SP-25) for blocking the laser light, and the second was a 390 nm band-pass filter (390 nm $\pm$ 18-25 nm) for selecting the second harmonic signal. In contrast to the wide-field CCD detector used in SLIM, SHGM uses a single point photodetector. More details regarding this particular SHGM system

have already been published in refs. (71) and (122). The acquisition rate for SHGM system was 7 μs per pixel while that for the SLIM system was 0.08 μs per pixel.

5.4.2 TMA

The breast TMA used in this study was purchased from US Biomax Inc. (Serial # T088b). The TMA was received from the manufacturer with all human subject information de-identified. Neither the authors of this work nor their institutions were involved in tissue collection. The TMA comprised of 24 cores from 6 different cases with 8 benign/normal and 16 malignant cases. The malignant cases included cores corresponding to three different stages of breast cancer: IIa, IIb and IIIa. The inserts of both Fig. 5.1 (a) and 5.1 (b) show an H&E image of the TMA. Also shown are H&E, SLIM and SHGM images of one of the cores in the TMA.

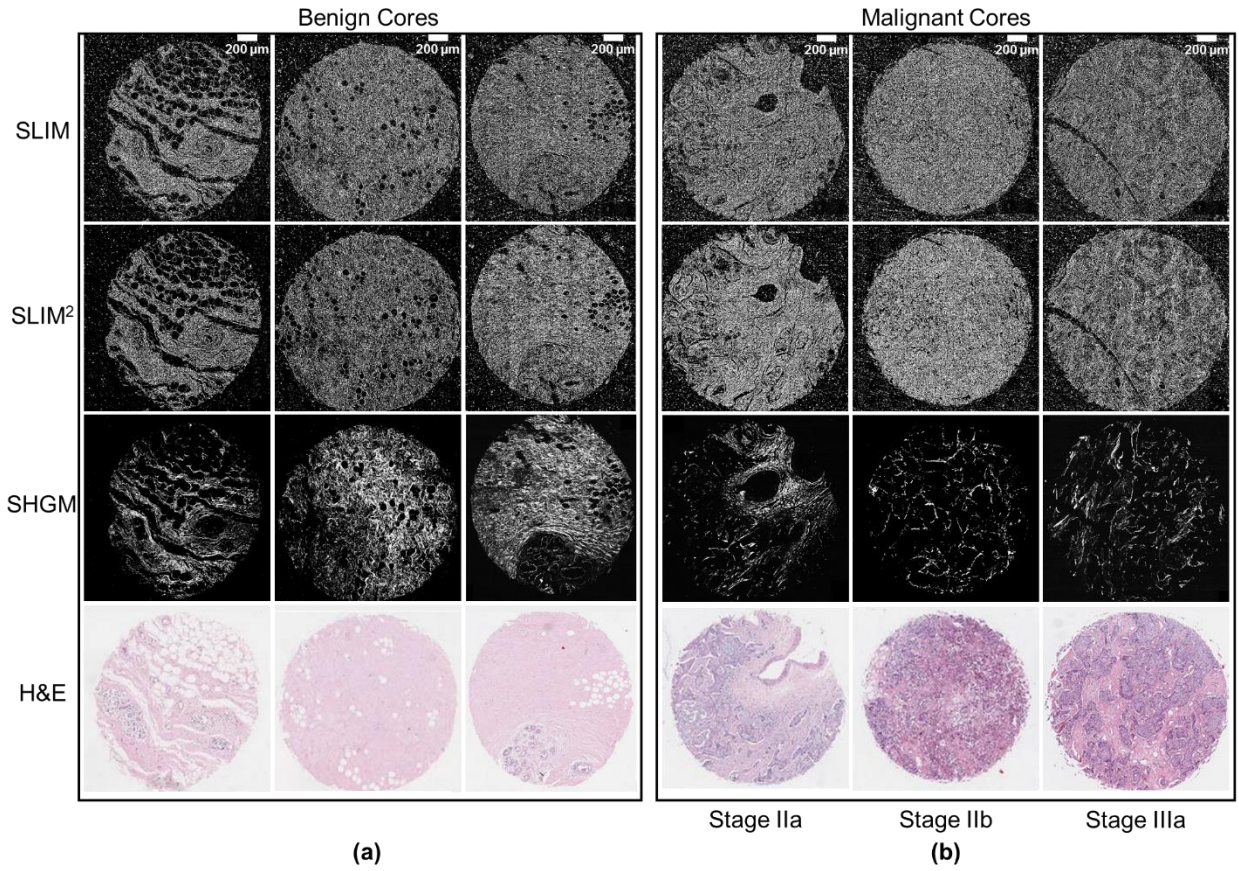

Figure 5.2. Morphological comparison between **(a)** Benign and **(b)** Malignant cores from patients at three different stages of disease as captured by SLIM, SHGM and H&E images. The square of the quantitative phase map in SLIM is referred to as SLIM^2, and is proportional to $\left[\chi^{(1)}\right]^2$.

Figure 5.2 shows H&E, SLIM and SHG images of 3 benign and 3 malignant cores, each at a different disease stage, as indicated. The SLIM images generate uniform contrast across the cores, including in cellular structures. SHGM images on the other hand generate contrast only in areas where collagen fibers are present. Note that the SHG signal is more sparse in the malignant cores versus benign cores due to the higher fraction of epithelial cells in the former, associated with tumor invasion into surrounding stroma. Row 2 of Figure 5.2 shows the square of the quantitative phase map $\phi(x,y)$ (SLIM^2), for each core.

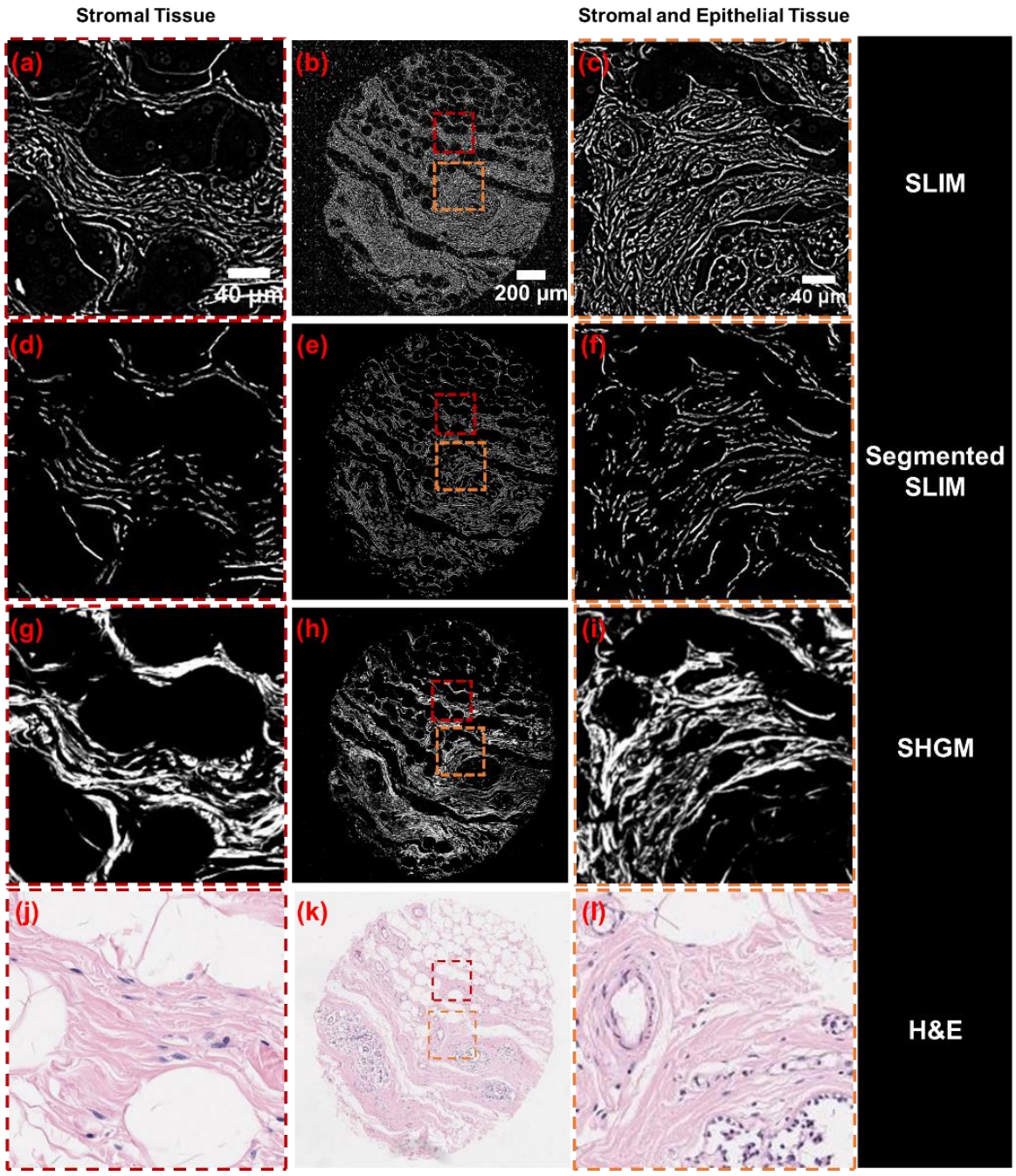

Figure 5.3. SLIM **(a-c)**, SHGM **(g-i)** and H&E **(j-l)** images of both stromal and epithelial/stromal mixed tissue in a TMA core. Left-most **(a,d,g,j)** and right-most **(c,f,i,l)** columns show zoomed-in versions of the regions indicated on the core in the central column **(b,e,h,k)**. As is evident from a comparison with the H&E images, the SLIM images show contrast in both stromal and epithelial regions where as the SHGM images only generate contrast in stromal regions. Segmented SLIM **(d-f)** images were obtained from the SLIM images by numerically removing the cellular structures and preserving the collagen fibers.

Figure 5.3 provides a comparison between morphologies of stromal and epithelial tissue within one core, as revealed in H&E, SHGM and SLIM images. As shown in Figs. 5.3 (a) and (g), both SLIM and SHGM reveal qualitatively similar stromal structures. The situation is different in areas with epithelial tissue where SLIM images [Fig. 5.3 (c)] contain centrosymmetric structures such as epithelial cells, which are absent in SHGM images [Fig. 5.3 (i)]. The presence of these cellular structures is confirmed by the H&E stain, which shows cell nuclei in purple color [Fig. 5.3 (l)]. In areas that are a mixture of cells and collagen fibers, quantifying fiber alignment and orientation from SLIM images requires segmentation of epithelial cells as discussed in detail in the next section.

5.5 Results

5.5.1 Decoupling isotropic from anisotropic signals in SLIM images

Prior to measuring collagen fiber orientation, the SLIM and SHGM images were registered and an image segmentation algorithm was used to remove isotropic structures from SLIM images, leaving behind the highly anisotropic collagen fibers. No information from the SHGM data was used for the segmentation of SLIM images.

To perform image registration, the SLIM images were first down-sampled, from 12000 x 12000 to 9,216 x 9,216 pixels/core, to match the sampling of the SHGM images. These images were then co-registered using ImageJ by selecting control point pairs for each image, and matching them using transformation techniques (primarily translation and rotation).

The image segmentation algorithm used for removing isotropic cellular structures from SLIM images is schematically illustrated in Fig. 5.4. Specifically, for each core image we first computed the response to the LM filter bank comprising gradient filters at 50 different orientations (90, 91). Each filter in the bank computed the directional image gradient by using the first

derivative of a Gaussian, oriented at $\Omega = \frac{j\pi}{50}$ where j = 0, 1, 2 ….. 49, from the horizontal axis in the image. The resulting stack of responses represented both the magnitude and direction of the local gradient or anisotropy in a pixel's vicinity for each TMA core. The magnitude of these gradients was then normalized by the highest value in the stack and was summed along the stack (along the z-axis in Fig. 5.4). The resulting image represented the isotropy map of the tissue with higher values representing locally isotropic structures (background and cells) and lower values representing locally anisotropic structures (collagen fibers). This isotropy map was then low-pass filtered (Gaussian kernel of 15x15 pixels which is slightly larger than one epithelial cell) and the Otsu's thresholding method was used to find the grayscale level separating anisotropic from isotropic pixels (123). The Otsu thresholding method dynamically sets the threshold by minimizing the intra-class variance and maximizing the inter-class variance under the assumption of a bio-modal class histogram distribution. Since this method establishes a threshold based on the natural separation of isotropic and anisotropic pixels in the data, it can be applied to arbitrary SLIM images without prior training. After setting the isotropic pixels to zero we employed another round of low pass filtering (Gaussian kernel, 5x5 pixels) followed by thresholding to remove any remaining background pixels and obtain the label map. During this process, the maximum gradient along z for each pixel was also used for detecting the remaining background pixels and marking them for removal. The final segmentation map was then computed by using the label map as a mask. The segmentation algorithm was coded in MATLAB and a pre-published LM filter generator was used for the purpose (92).

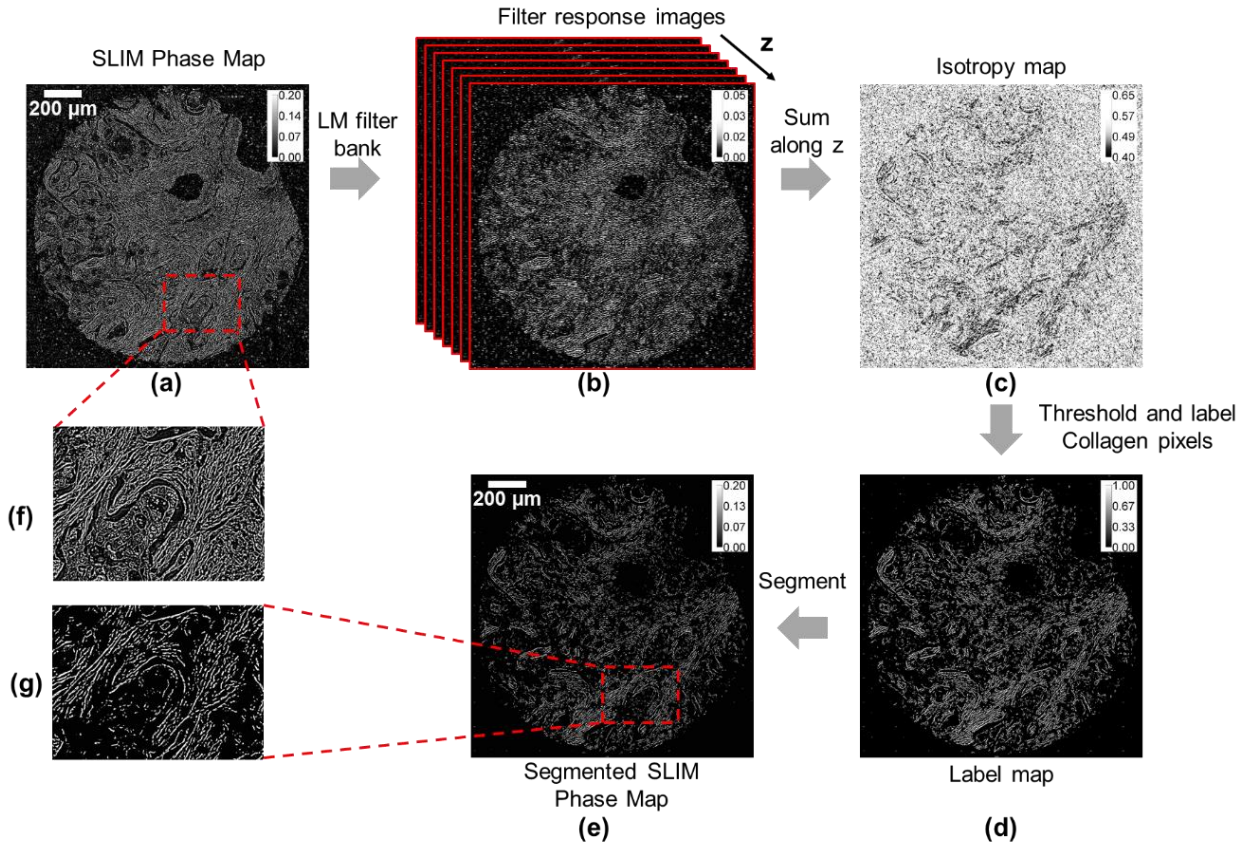

Figure 5.4 The segmentation algorithm for removing isotropic structures from SLIM phase images. **(a)** SLIM phase map before segmentation (color bar in radians). **(b)** Response to LM filter bank. **(c)** Normalized isotropy map. **(d)** Binary label map. **(e)** Segmented SLIM image (color bar in radians). **(f)** and **(g)** represent zoomed-in portions of the SLIM and Segmented SLIM images respectively, showing an epithelial stromal boundary. The segmentation algorithm removes isotropic structures and preserves anisotropic signals associated with collagen fibers.

As apparent from comparing the SLIM and segmented SLIM images in Figs. 5.4 (f) and 5.4 (g), the algorithm leads to over-segmentation, and sometimes collagen fibers that are isotropic at length scales equal to or smaller than the size of one epithelial cell are segmented out. In some cases, the segmentation algorithm may break up thin or twisting fibers. As shown in Section 5.4 (c), these imperfections in segmentation are subdominant, and the local collagen orientation remains similar between SLIM and SHGM images. Furthermore, as demonstrated in refs. (5, 121, 124), biomarkers for prognosis are based on average orientation of collagen over spatial scales that

are longer than those at which segmentation errors occur in our images. Thus, for the relevant clinical applications, sufficient information remains in the segmented SLIM images to measure fiber–orientation based bio-markers. Another important consideration for clinical applications is the relative orientation of tumor adjacent collagen fibers with the tumor boundary. While SLIM images can be segmented to digitally remove the epithelial cells, they clearly resolve epithelial structures, allowing determination of the tumor boundary orientation with respect to the collagen fibers.

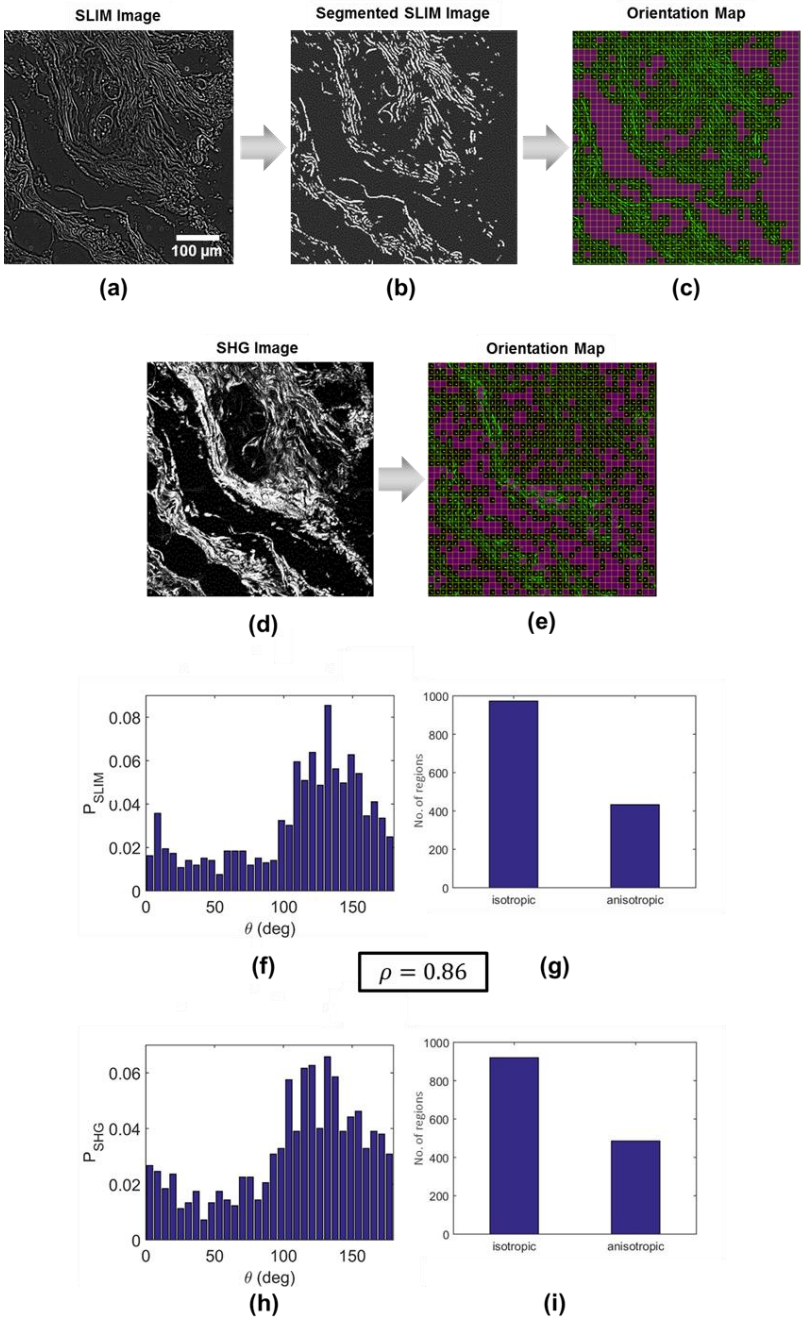

Figure 5.5 The Fourier analysis procedure for computing collagen fiber orientation probability densities. **(a)** SLIM image. **(b)** Segmented SLIM image. **(c)** Orientation map of SLIM image. **(d)** SHGM image. **(e)** Orientation map of SHGM image. **(f)** Probability density of collagen fiber orientation θ computed from the SLIM orientation map in **(c)**. **(g)** Bar chart showing the number of isotropic and anisotropic regions in segmented SLIM image. **(h)** Probability density of collagen fiber orientation θ computed from the SHGM orientation map in **(e)**. **(i)** Bar chart showing the number of isotropic and anisotropic regions in SHGM image. The Pearson's correlation ρ between the probability densities for the two modalities is also shown.

5.5.2 Fourier analysis

Fourier analysis was carried out on SHGM and segmented SLIM images to extract collagen fiber orientation. Each image was sectioned into sub-image regions using grids (16×16, 32×32 or 64×64), and the localized orientation per sub-image (which we call θ) was determined using the Fourier analysis technique outlined in ref. (121). Regions having a mean direction above a chosen threshold were referred to as anisotropic regions, while those under this threshold were labeled isotropic. In order to highlight preferred orientation in each sub-image, quiver plots were superimposed on anisotropic regions to give an orientation map. Histograms of θ for anisotropic regions (number of bins = 32), and bar plots showing the isotropic and anisotropic region counts were also generated from these data. The θ histograms were further normalized to obtain orientation probability densities $P_{SHG}(\theta)$ and $P_{SLIM}(\theta)$. Figure 5.5 shows the comparable results obtained for a selected pair of segmented SLIM and SHGM images.

5.5.3 Comparison between SHGM and SLIM signals

Figure 6 shows the fiber orientation probability densities P_{SHG} and P_{SLIM} for three different cores, extracted from their respective SHGM and segmented SLIM images. As shown, the shapes of the density functions obtained from the two modalities are qualitatively similar for each of the cores. In order to obtain a quantitative measure of this similarity, the following procedure was used. The cross-correlation between P_{SHG} and P_{SLIM} was first obtained and the circular lag corresponding to maximum cross-correlation was computed. The two densities were then shifted relative to one another by this lag, such that any errors due to overall rotation between the two images are minimized. This alignment procedure is required for a fair comparison between the two densities because errors in registration of the images from the two modalities can cause one density

to be slightly shifted with respect to the other. After alignment, the Pearson's correlation coefficient ρ between the two densities was computed as a quantitative measure of their similarity. The Pearson's correlation measures the similarity of any two random variables X and Y, and is defined as

$$\rho = \frac{E\left[\left(X-\mu_x\right)\left(Y-\mu_y\right)\right]}{\sigma_x \sigma_y}. \tag{5.7}$$

In Eq. 5.7, the operator $E[\,]$ refers to the expected value and μ and σ are the mean and standard deviation of the random variable in question (125). The correlation coefficient ρ has values over the interval [-1, 1] with -1 referring to perfect negative correlation and 1 corresponding to perfect positive correlation. In our analysis, X and Y refer to the probability densities P_{SHG} and P_{SLIM} .

The three cores in Fig. 5.6 belong to three different disease stages and, therefore, correspond to three different morphologies. As shown, the benign core shows the highest positive correlation between P_{SHG} and P_{SLIM} with ρ = 0.93, which decreases to 0.82 for the stage IIa malignant core. The lowest correlation is seen for the stage IIIa core which was computed as 0.71. This trend can be accounted for by the fact that a core from a patient at an advanced stage of disease is more likely to contain large amounts of epithelial tissue. A large proportion of epithelial tissue both suppresses the SHG signal and results in greater image segmentation errors in SLIM images due to the smaller amount of collagen involved, resulting in lower agreement between the two. In addition to the probability densities, the bar charts showing the number of isotropic and anisotropic cells counted by the Fourier analysis procedure, are also very similar for both imaging modalities as demonstrated in Fig. 5.6.

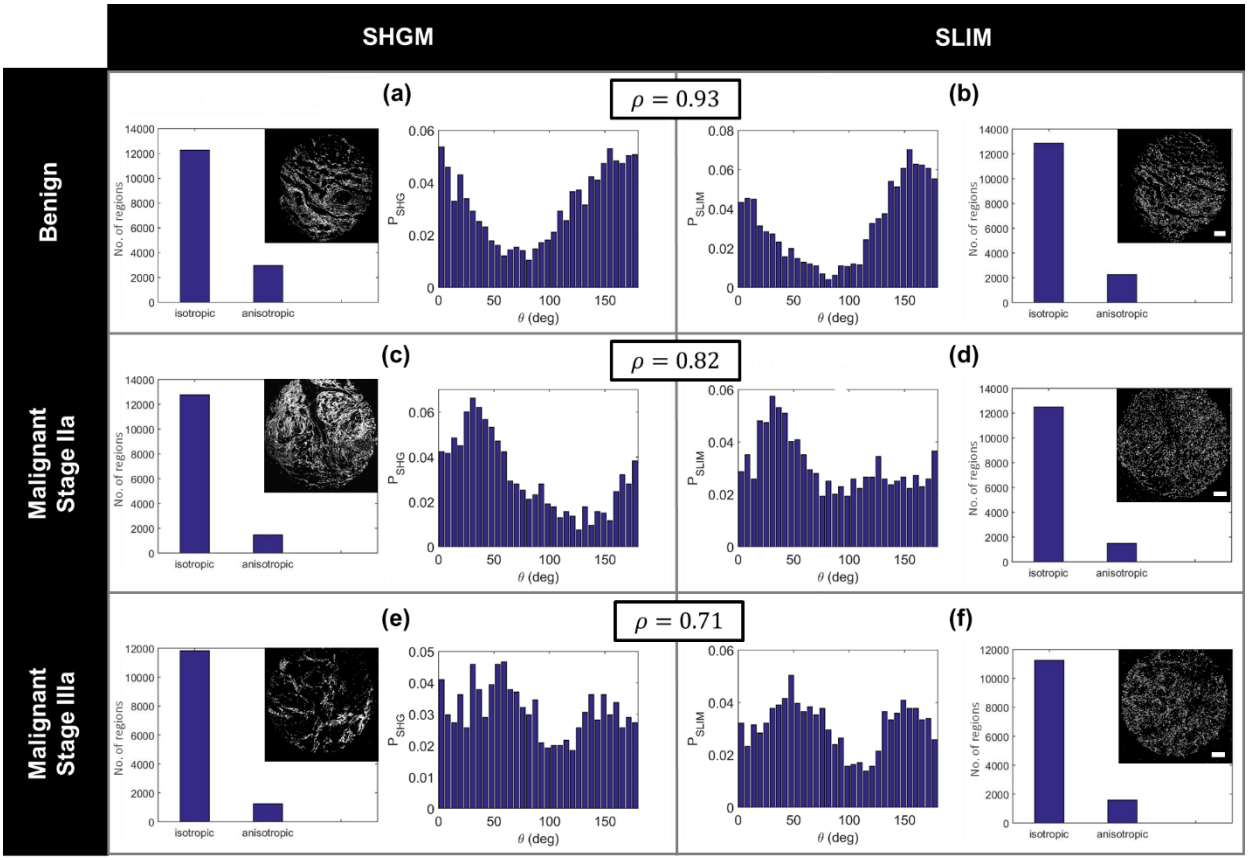

Figure 5.6. Comparison between the fiber orientation probability densities and bar charts counting number of isotropic and anisotropic regions for 3 different cores: SHGM (left column) and SLIM (right column). This comparison is shown for a benign core (a-b), malignant stage IIa core (c-d) and malignant Stage IIIa core (e-f). The similarity of P_{SHG} and P_{SLIM} is measured for each case using the Pearson's correlation coefficient ρ, as indicated. Scale bars: 200 µm.

5.5.4 Measuring relative angles of tumor adjacent fibers using SLIM

While the results of the last section demonstrate that collagen fiber orientation is measurable using SLIM, collagen fiber based histological markers (for example TACS3) are based on *relative* angle θ_r between tumor adjacent fibers and the nearest point on the tumor or ER edge (5, 126). This angle is schematically illustrated in Figure 5.7. To demonstrate that θ_r is measurable using SLIM, we used a MATLAB based open-source fiber analysis tool called "CurveAlign" (116,

127) and extracted θ_r for 34 benign and 34 malignant cases selected from a TMA. This the same TMA that was used for the study in Chapter 4. A description of CurveAlign and specifics of parameters used during fiber analysis are included in Section 6.4.7. As discussed in Section 4.3.3, all ERs within each core from this TMA had been manually annotated using the region-of-interest tool of ImageJ. Before fiber extraction and angle measurement, each ER was segmented out to ensure edges of epithelial cells did not interfere with fiber analysis.

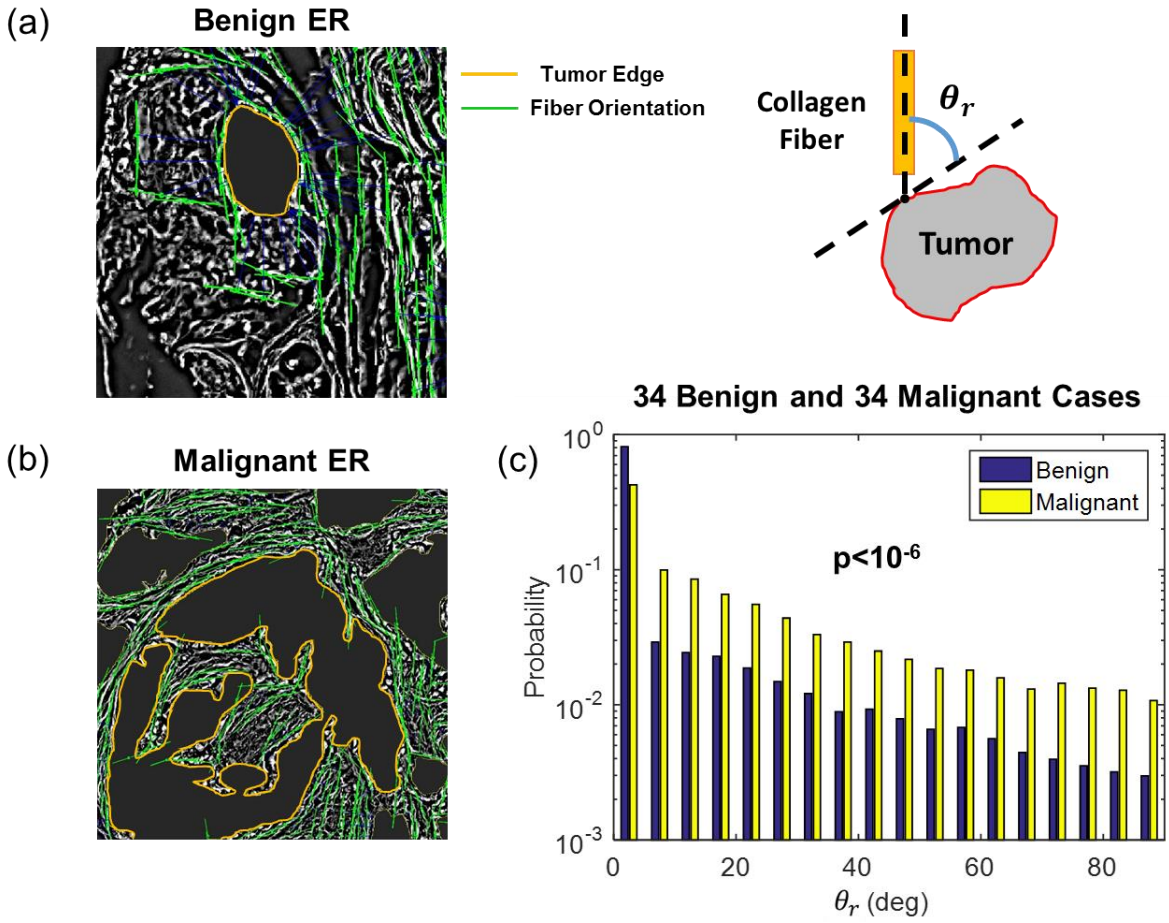

Figure 5.7 Fiber orientation relative to tumor edge for **(a)** Benign and **(b)** Malignant ERs. (c) Histogram of relative angles measured for 34 benign and 34 malignant cases, showing that on average higher relative angles are measured for malignant tumors.

Figure 5.7 (a) and (b) show benign and malignant ER edges and orientations of fibers within their vicinity. Fibers within a distance of 64 μm from the ER edge were associated with each ER during this analysis. As is evident from these images, benign ERs have on average lower values of θ_r than malignant ERs. This is both due to the presence of the basement membrane around benign epithelium (which tracks its perimeter) but also because invasion in malignant epithelium can occur along collagen fibers (5). The results from all epithelium adjacent fibers within the 34 benign and 34 malignant cases are summarized in the histogram in Fig. 5.7 (c). As shown, there is statistically significant difference between the relative angles measured for benign and malignant tissue (determined using the two-sample Student's T-test). Furthermore, the probability of higher values of θ_r is higher for malignant cases than for benign cases. These data agree with previous studies that have linked higher relative angles with worse prognosis (TACS3 marker) and have suggested that collagen fibers oriented perpendicular to the tumor edge may serve as highways for epithelial cell invasion to surrounding tissue (5).

5.6 Summary and Conclusion

Motivated by the relationship between $\chi^{(2)}$ and $[\chi^{(1)}]^2$ (Section 5.2), we have presented experimental support for the hypothesis that measuring $\chi^{(1)}$ via phase-resolved imaging, can provide $\chi^{(2)}$ information, similar to that obtained in SHGM. Specifically, we have shown that, SHGM and segmented SLIM images measure quantitatively similar collagen fiber orientations in breast tissue. The conclusions are significant because collagen fiber alignment and orientation are potential markers for patient prognosis. We further showed that the relative orientation between tumor adjacent fibers and tumor edge, as measured by SLIM, is significantly different between cancerous and non-cancerous tissue. While in the past SHGM has been the method of choice for

measuring these biomarkers, our results demonstrate the potential of SLIM as a complementary method for this assessment. Clearly, compared to SHGM, SLIM lacks the specificity to collagen, as the phase image includes signals due to centrosymmetric molecules. As a result, a numerical post-processing procedure is necessary to eliminate the isotropic structures from the SLIM image. However, these isotropic signals, mainly from epithelial contributions, can be used to delineate the glands and potentially, tumor margins. These margins are difficult to detect in SHGM alone and other modalities are sometimes used (e.g., two-photon fluorescence microscopy) (117, 128).

In comparing the optical setups of the two modalities, it is evident that SLIM benefits from common components, of much lower cost, compared to those needed in SHGM (e.g., halogen lamp *vs.* femtosecond laser). Furthermore, due to the full-field and continuous wave (CW) illumination, SLIM operates at much lower exposures and, thus, is non-perturbing to live cells and tissues. For example, SLIM imaging over multiple days without damage is possible (35). The acquisition rate of the SLIM system is 0.08 μs per pixel as compared to 7 μs per pixel for the state of the art SHGM system used here. Of course, SLIM signals do not depend on phase matching and, as such, the signals are always quantitatively related to the structure under investigation.

While we showed in this study that the relative fiber angle, measured using SLIM, is higher for cancerous tissue as compared with healthy tissue, future studies that specifically compare SLIM based fiber features between cancer patients that have different outcomes are needed. This is explored in the next chapter in Section 6.3.5.

Chapter 6: QPI of stained breast tissue biopsies

6.1 Abstract

Thus far we have presented in this thesis QPI investigations that have relied on imaging of unstained tissue. Such an approach poses challenges in clinical adoption of QPI-based disease markers because *stained* tissue is typically assessed in a pathology lab. In this work, we show that phase maps of stained tissue, provided by QPI, can be leveraged to extract markers of disease in a manner similar to that shown for unstained tissue. We numerically correct for the effects of staining on tissue phase maps and show that features extracted from the resulting 'normalized phase maps' have similar values to those in corresponding unstained tissue. Our imaging system provides these maps and traditional bright-field images of stained tissue in a single acquisition. Thus, our instrument reduces barriers to clinical translation as a clinician can potentially obtain traditional markers of disease as well novel quantitative phase based markers simultaneously. We demonstrate the utility of our stained tissue analysis instrument by diagnosing breast cancer through supervised learning and measuring collagen fiber based prognostic markers in breast tissue.

6.2 Motivation and Overview

I have demonstrated in the previous three chapters that SLIM based features have utility for quantitative breast tissue diagnosis. I also demonstrated that collagen fiber structure can be assessed from SLIM images. In both cases, the analysis was performed on unstained tissue sections. Staining is an inevitable part of standard histopathology in a clinic so if a pathologist wants to look at SLIM based disease markers during investigations, they'll need to obtain a separate dedicated, unstained tissue slice. We propose in this work to bridge this barrier to clinical translation in QPI by demonstrating that analyses previously done on unstained breast tissue biopsies can be extended to stained tissue. We modified SLIM (48) to provide both phase and bright-field microscopy images in a single acquisition. The resulting system is referred to a color spatial light interference microscopy (cSLIM). Next a TMA was imaged using SLIM and cSLIM before and after H&E staining, respectively. Both sets of raw phase images, $\phi(x,y)$, were then normalized numerically to obtain normalized phase images $Z(x,y)$. For the same TMA core, $Z(x,y)$ maps showed excellent agreement pre- and post-staining indicating their stain independence. We further demonstrated that results from supervised learning based detection of breast cancer as well as extraction of stromal collagen fiber orientation using these normalized phase maps also produces similar results in stained and unstained tissues. Having shown that analyses developed for unstained biopsies are extendable to stained ones, we demonstrated the ability of our stained tissue analysis system to diagnose histologically difficult cases and to detect aligned collagen fiber-based prognostic markers that have been previously shown to correlate with outcomes in breast cancer patients.

6.3 Results and Discussion

6.3.1 cSLIM optical setup and outputs

The cSLIM optical setup is illustrated in Fig. 6.1. The optical train is based on the previously described SLIM system (48) with two important modifications. First, in the place of the phase contrast microscope objective used in SLIM we employ a 40x/0.75 NA bright-field objective. The use of a bright field objective allows us to obtain typical H&E stained histology images that are the mainstay of breast histopathology in the clinic. The annular condenser ring is retained from the SLIM system. Second, the grayscale camera is replaced by a color RGB camera (Carl Zeiss Axiocam MRc) which provides red, green and blue spectral channels of information. The remainder of the system operates as previously described for SLIM: The SLIM module (CellVista SLIM Pro, Phi Optics, Inc.) is placed at the output port of a commercial microscope. The conjugate image plane at the microscope output port is imaged onto the camera using a 4f system formed by lenses L_1 and L_2. At the Fourier plane of lens L_1 an SLM (Boulder Nonlinear Systems) is used to modulate the phase difference between the scattered and incident components of light. As illustrated in Figs. 6.1 (c) and (d), four modulations, $\varphi = 0, \pi/2, \pi, 3\pi/2$ rad, are employed. For each modulation, we acquire three intensity frames corresponding to the red, green and blue channels of the camera: $R(x,y;\varphi), G(x,y;\varphi)$ and $B(x,y;\varphi)$, respectively. In each case, these channels are combined to obtain an equivalent grayscale intensity image using the formula

$$I(x,y;\varphi) = 0.1R(x,y;\varphi) + 0.6G(x,y;\varphi) + 0.3B(x,y;\varphi). \quad (6.1)$$

The weighting attached to each channel was determined empirically and is related to the resulting wavelength at which phase modulation occurs between the scattered and incident light in cSLIM [see Section 6.4.3 of the Methods section for details]. Thus four intensity frames $I(x,y;\varphi)$ are acquired for each phase map, $\phi(x,y)$, reconstruction. The phase reconstruction process using

these four frames is identical to that previously published for SLIM (48) and is typical of phase shifting interferometers (46).

The modifications to the original SLIM system required us to perform two calibration steps. First, SLM re-calibration was required to ensure that the correct value of φ is used for each of the four frames (48). This was performed by configuring the SLM in amplitude mode and measuring the amplitude modulation in $I(x, y; \varphi)$ as a function of the SLM 8-bit grayscale input (48). The calibration curve for phase was then obtained by taking the Hilbert transform of the amplitude modulation curve [see Section 6.4.3 for details]. Second, the SLIM phase reconstruction algorithm includes the attenuation term α_{pc} which is the factor by which incident light is attenuated with respect to the scattered light in a phase contrast objective. Since bright field objectives do not impart his attenuation, an equivalent attenuation α_{bf} was introduced numerically in place of α_{pc} in the SLIM phase reconstruction. The correct value of α_{bf} was determined by imaging an unstained TMA core using both phase contrast and bright field objectives and tuning α_{bf} until the similarity between the phase maps from the two acquisitions was maximized [see Section 6.4.4]. The final value of $\alpha_{bf} = 3.4$ was then used for all subsequent phase reconstructions.

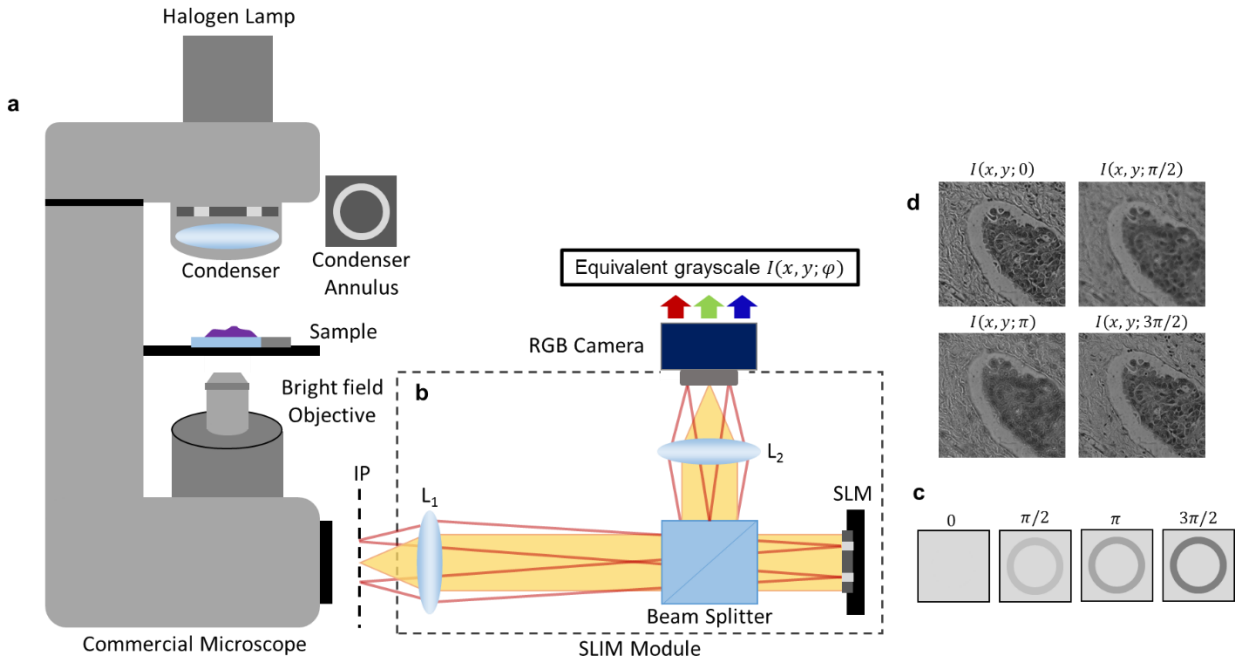

Figure 6.1 cSLIM optical setup. **(a)** A commercial microscope with phase contrast illumination and bright-field objective. **(b)** SLIM module placed at the microscope output port, equipped with color RGB camera. **(c)** Phase shifts imparted between scattered and incident light by the SLM in the Fourier plane of L_1. **(d)** Four intensity frames obtained for each phase modulation by weighted sum of the red, green and blue channel images of the RGB camera. IP, image plane, SLM, spatial light modulator.

The typical raw outputs generated by the cSLIM system are illustrated in Fig. 6.2. Results are shown for an H&E stained TMA at the slide [Figs. 6.2 (a) and (d)], core [Figs. 6.2 (b) and (e)] and cellular scales [Figs. 6.2 (c) and (d)]. As shown, whole slide phase and bright-field microscopy images are obtainable in a single scan. The scan time for a single core (approx. 1 mm^2 area) was approx. 13 secs at a sampling rate of 7.4 pixels/ μm. A key advantage of the cSLIM outputs is that perfectly registered standard histopathology and quantitative phase images are obtainable. This is significant in carrying out QPI studies with large cohorts since independent pathologist evaluation can be done on the same tissue rather than a parallel section. This ensures that a pathologist's diagnosis matches precisely with markers extracted in QPI without the need for duplicate scanning of tissue section before and after staining. Furthermore, information from both channels (phase

and bright-field) can be combined for improving results of classification and segmentation problems for which algorithms related to both modalities have been published, separately thus far, in literature (19, 20, 25, 87).

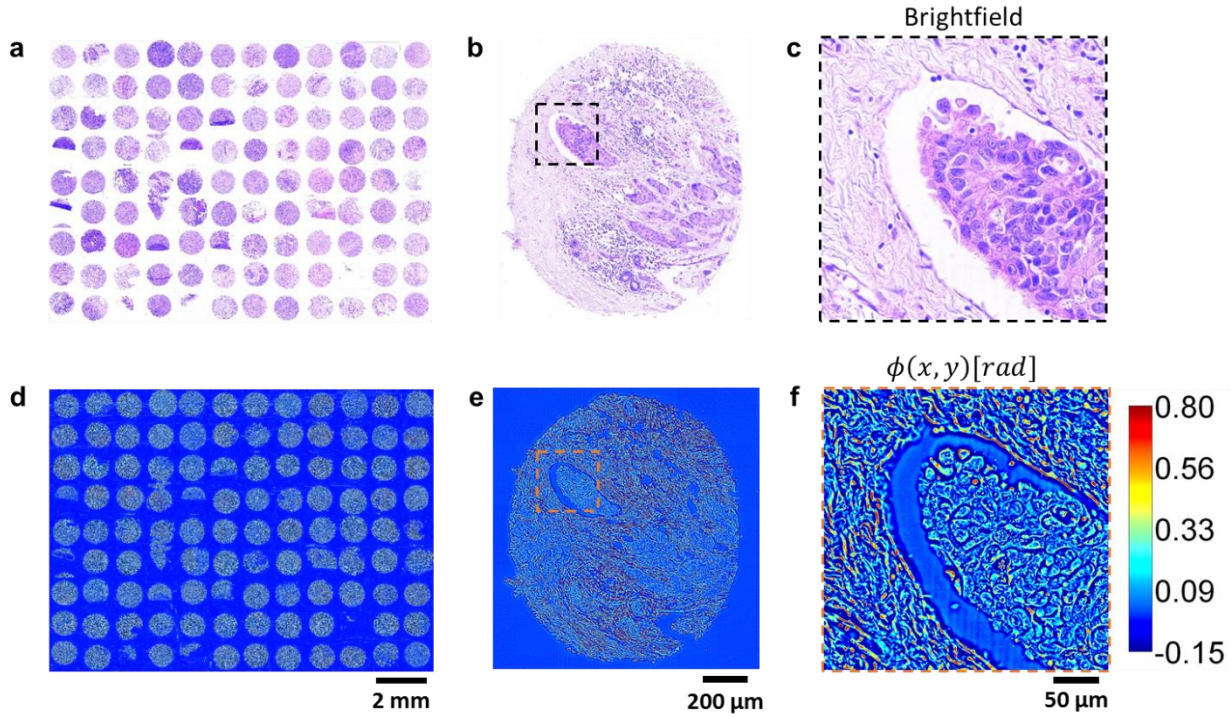

Figure 6.2 cSLIM outputs obtained by scanning a whole TMA slide. **(a)-(c)** H&E stained tissue bright-field images of whole slide, single core and epithelial region within core, respectively. **(d)-(f)** Raw phase maps of whole slide, single core and epithelial region within core, respectively.

6.3.2 Normalizing effects of staining

The spectrum of light is not identical between the SLIM and cSLIM systems – there is a difference in both the spectral width (determined by the coherence length l_c) as well as the central wavelength λ_0. For the SLIM system $\lambda_0 = 589\,nm$ and $l_c = 2.26\,\mu m$ in air whereas for cSLIM, in the absence of tissue, $\lambda_0 = 558\,nm$ and $l_c = 3.24\,\mu m$ also in air [see Methods Section 6.4.3]. When stained tissue is present, the cSLIM spectrum the will vary even further due to absorption (refer to Appendix A for analysis of dispersion in tissue). As a result, phase maps extracted from stained and unstained tissue samples differ. To quantify this difference we imaged a TMA of breast tissue

biopsies before H&E staining using SLIM and after staining using cSLIM. We refer to this TMA as "TMA-1" in the rest of the chapter [refer to Methods Section 6.4.1 for details about TMA-1]. This is the same TMA that was used in ref. (87) and Chapter 4 for separating normal and cancerous cases using SLIM based features. The raw phase maps $\phi(x,y)$ for one TMA core, before and after staining, are illustrated in Figs. 6.3 (a) and (b), respectively. It is evident that staining causes a reduction in phase values as well as the image contrast. These effects are also illustrated in the histograms of the two phase images in Fig. 6.3 (c) where the stained tissue histogram is noticeably narrower. To normalize these effects of staining we computed, for each core, the standard normal variable $Z(x,y)$ from $\phi(x,y)$ using the equation

$$Z(x,y) = \frac{\phi(x,y) - \mu}{\sigma} \tag{6.2}$$

where μ is the mean of $\phi(x,y)$ in the tissue region within each core image (after segmenting out background pixels) and σ its standard deviation. Details about this computation, including removal of background pixels, are described in Methods, Section 6.4.5.

The results of this normalization procedure are shown in Figs. 6.3 (d) – (f). As shown, the normalized phase maps are visually very similar between stained and unstained tissue and the histograms seem to overlap almost perfectly. To quantify this similarity, the Pearson's correlation coefficient ρ (125) was computed between the stained and unstained tissue histograms, both before and after phase normalization. As illustrated in Figs. 6.3 (c) and (f), the ρ values improved significantly due to the normalization procedure (were in fact almost equal to 1), indicating a very high degree of correlation. The ρ values for a total of 30 cores (15 cancerous and 15 normal, selected randomly from TMA-1), before and after normalization, are summarized in Fig. 6.3 (g). The bar heights represent mean values whereas the error bars represent the standard deviations

over the 30 cores. The $Z(x,y)$ maps are, thus, consistently more similar before and after staining than $\phi(x,y)$ maps indicating a stain independent signal in the normalized images. Benign and malignant tissue have different stain distributions due to differing proportions of epithelium and stroma as well as a different cellular phenotype. In addition, the cores used for this analysis were selected randomly from different parts of the TMA slide, meaning that their staining intensities can potentially vary due to local variations in staining agent concentration. Despite these sources of variation, our normalization technique is robust and works well across the cores considered.

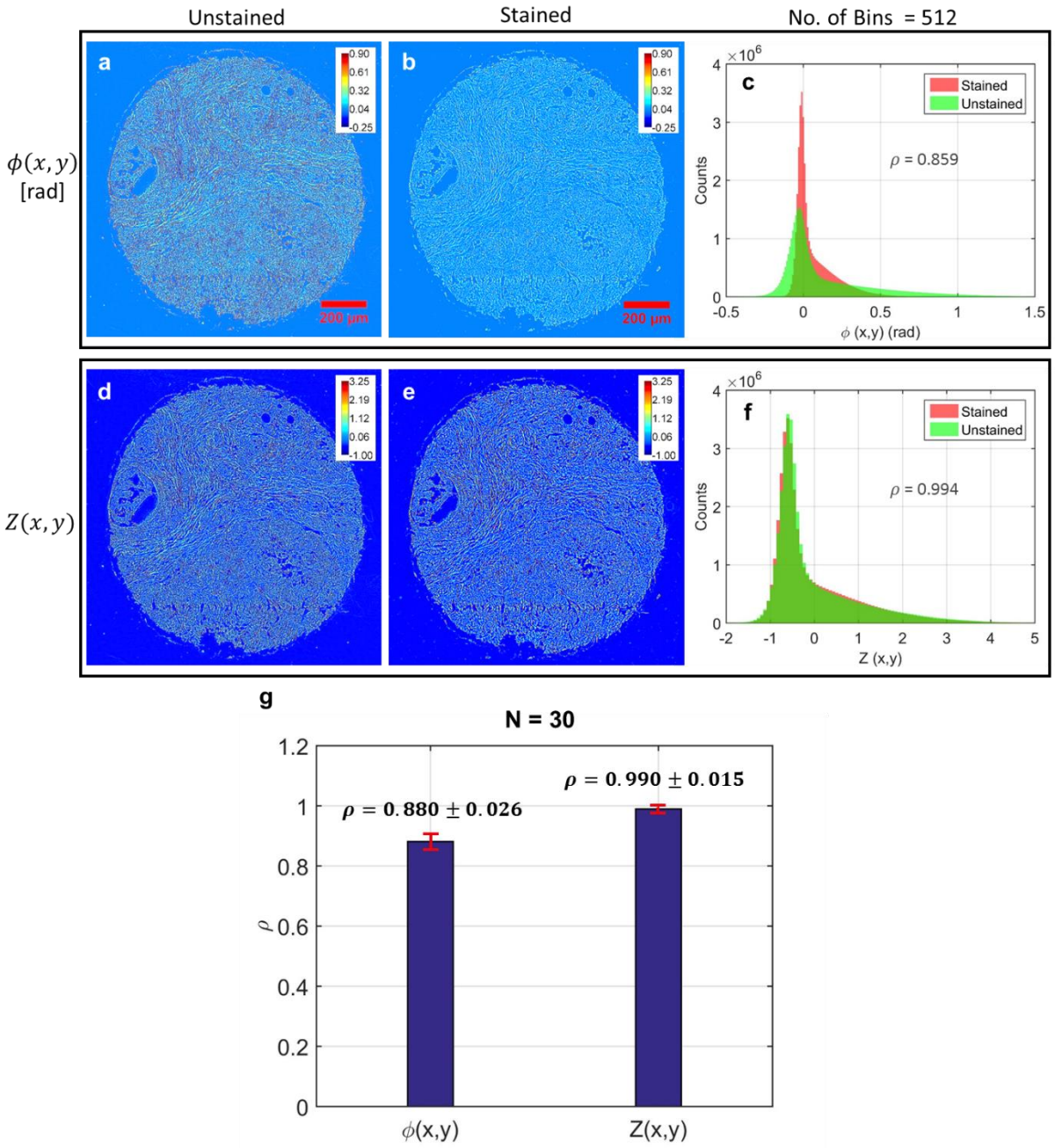

Figure 6.3 Comparison of phase maps obtained from the TMA-1 before and after staining. **(a)** and **(b)** TMA core raw phase images before and after staining, respectively. **(c)** Histograms of the phase images in (a) and (b). The similarity of the two histograms is quantified by computing the Pearson's correlation coefficient ρ between them. **(d)** and **(e)** Normalized phase maps for the same core before and after staining, respectively. **(f)** Histograms of the phase images in (d) and (e). The similarity of the two histograms is quantified by computing the Pearson's correlation coefficient ρ between them. **(g)** Bar plots showing the mean value of Pearson's correlation coefficient ρ between core histograms for raw and normalized phase maps. Error bars show the standard deviation over the 30 cores.

Computation of $Z(x,y)$ minimizes the difference between SLIM and cSLIM results because division by standard deviation removes the $1/\lambda$ dependence of the phase maps so that variations due to different λ_0 between the two systems, in absence of absorption in tissue, are minimized (for details see Appendix A). While dispersion in tissue (spatial variation of both wavelength and refractive index) is also expected to cause differences between these images, our detailed analysis of this phenomenon (included in Appendix A) showed that these changes are small. The fact that a global normalization is effective in removing the stain-related effects also indicates that dispersion in tissue is not a dominant effect (see Appendix A).

6.3.3 Breast cancer diagnosis on stained tissue biopsies using supervised learning

6.3.3.1 Classifying benign versus malignant cases

As stated earlier, features extracted from SLIM images of unstained tissue have been shown to detect malignancy in different organs (50, 52, 87). In ref. (87) and Chapter 4 we developed a supervised learning method for breast cancer diagnosis that relied on three types of features extracted from SLIM images: the median gland or ER curvature $<C>$, the median of mean scattering length within an ER $<l_s>$ and the median texture vector for the ER $<T>$. These features were extracted from and compared between benign and malignant ERs within a TMA (unstained TMA-1 was used in that study). 3-fold cross-validation results showed an AUC of 0.91 during ROC analysis of the classification (87).

To demonstrate that this analysis can be extended to stained tissue cores, for the 15 malignant and 15 benign cores selected from TMA-1 in the previous section, we assembled $Z(x,y)$ maps both before and after staining. Each core belonged to a different case/patient. All malignant cases were diagnosed as IDC whereas the all benign cases were diagnosed benign

without atypia (BWA) by a certified pathologist. From the $Z(x, y)$ maps of each core, the same feature set $[< C >, < l_s >, < T >]$ was extracted for each ER. Pathologist diagnosis for each ER was available and was used as the ground truth for training [see Section 6.4.1 for details]. The classification scheme developed for $\phi(x, y)$ in Chapter 4 was repeated for $Z(x, y)$ in both stained and unstained cases and the results were compared. Details of the feature extraction, training and validations steps, specific to this study, have been included in Methods, Section 6.4.6.

Figure 6.4 illustrates the diagnosis results obtained for stained and unstained tissue. Figs. 6.4 (a), (b), (d) and (e) compare $Z(x, y)$ for example benign and malignant ERs before and after staining. As shown, once again the images are very similar between the before and the after. In cSLIM, morphological details of these ERs are also available for traditional histopathological assessment through bright-field images [Figs. 6.4 (g) and (h)]. To test whether features derived from these $Z(x, y)$ maps can detect malignancy in breast tissue, 3-fold cross-validation was performed, consisting of three trials. ERs from all cores were pooled and divided into three equal sets and in each trial two sets were used for training and one set for validation. Figs. 6.4 (g) and (h) compare the values of the three features between unstained and stained ERs, for one training set. Since texture feature $< T >$ is multidimensional, it is represented by its first principal component in the plot. As is noticeable, the feature values have a similar distribution for both benign and malignant ERs between the unstained and stained cases.

In each case, the probability scores for all ERs, generated by an LDA classifier in all three trials, were pooled together to generate an ROC curve for the cross-validation [see Section 6.4.6]. As shown in Fig. 6.4 (i), similar AUCs were measured for analysis on both

stained and unstained tissue using $Z(x,y)$ maps, indicating that detection of malignancy is achievable at high accuracy using stained tissue biopsy phase maps. While the AUCs are similar, they are not identical. This can be attributed to the fact that the tissue morphology itself (while similar) is not identical between the two experiments since the process of removing the coverslip from the TMA slide and staining it results in some physical changes to the tissue biopsies, in addition to those due to staining.

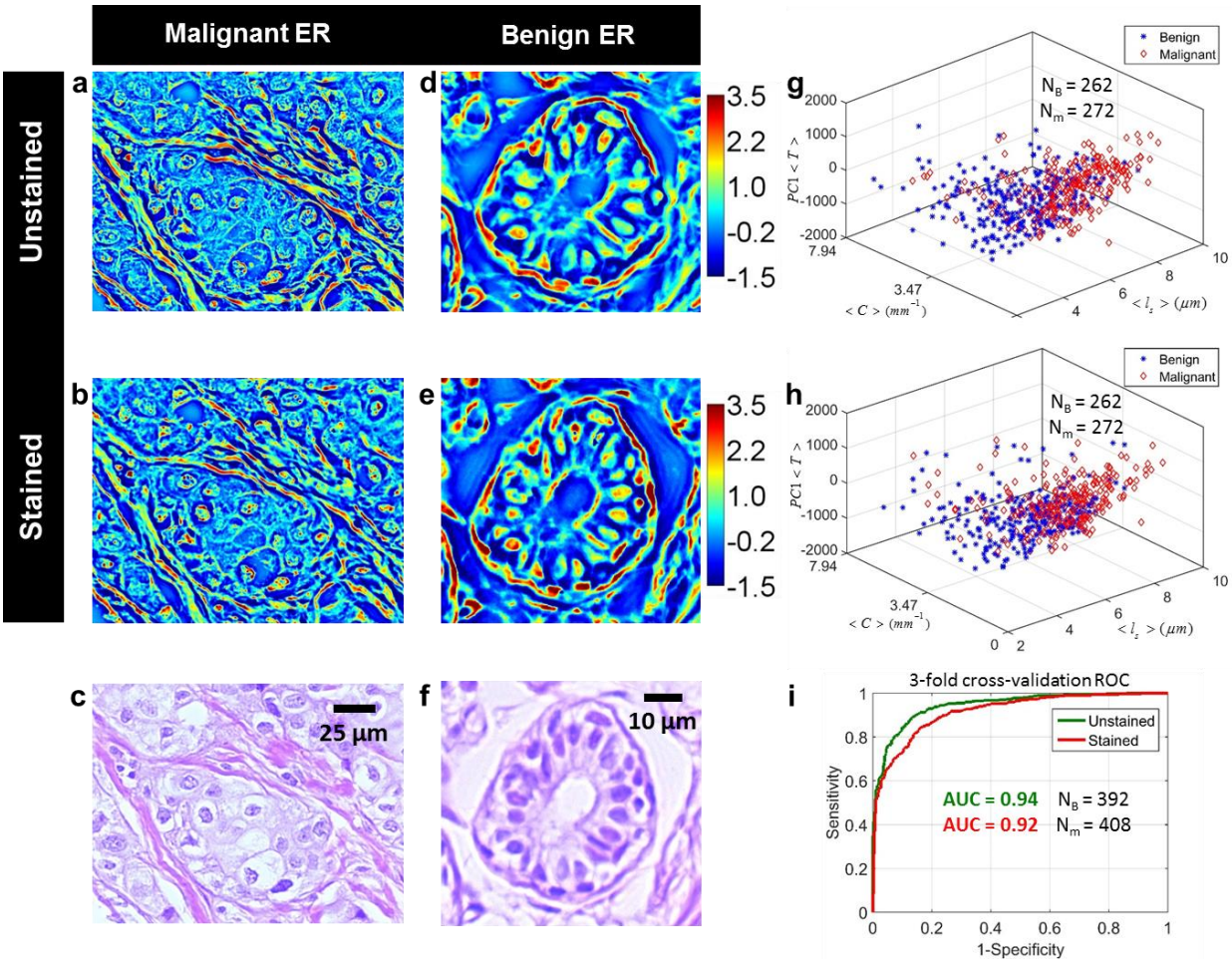

Figure 6.4 Comparison of diagnosis results between stained and unstained tissue using $Z(x,y)$ maps. **(a)-(b)** $Z(x,y)$ images of an unstained and stained malignant ER, respectively **(c)** H&E stained bright-field image of the same malignant ER. **(d)-(e)** $Z(x,y)$ images of an unstained and stained benign ER, respectively. **(f)** H&E stained bright-field image of the same benign ER. **(g)-(h)** Separation of benign and malignant ERs in feature space for stained and unstained tissue, respectively. **(i)** ROC curves for 3-fold cross-validation for classifying benign and malignant ERs.

6.3.3.2 Screening of high-risk and low-risk breast lesions using cSLIM

Having demonstrated that our feature set has the ability to detect malignancy on stained tissue biopsies, we next applied our model to a more diagnostically challenging problem. Stratification of benign lesions in breast tissue during histopathology is a significant challenge for pathologists (15, 129, 130). One of the key questions is finding a consistent and quantitative basis for separating cases of benign atypical hyperplasia (BAH) from cases of BWA. QPI based markers can help pathologists during these borderline investigations by supplementing the information available in traditional histopathology with quantitative markers. To demonstrate that our feature set is capable of stratifying benign lesions, we imaged a second H&E stained TMA consisting of 9 cases of BAH (2 cores per case), 9 cases of IDC (2 cores per case) and 17 cases of BWA (2-3 cores per case). We refer to this TMA as 'TMA-2' in the rest of the chapter. Details regarding TMA-2 are included in Section 6.4.1. TMA-2 was imaged using the cSLIM system and $Z(x, y)$ maps for each core were assembled. Figs. 6.5 (a) and (b) show the bright-field and $Z(x, y)$ maps for an ER with BAH, acquired by the cSLIM system. Examples of ERs diagnosed as BWA and IDC have already been shown in Fig. 6.4.

The cores in TMA-2 were used to construct two groups: a high-risk group consisting of 18 cases (IDC and BAH) and a low-risk group consisting of 17 cases (BWA). This study design is illustrated in Fig. 6.5 (c). The data were partitioned in this way because diagnosis of BAH, while not considered a diagnosis of cancer, has clinical significance and patient follow-up is carried out to ensure further progression of disease is prevented (129, 130). A patient diagnosed with BAH is, therefore, placed into a higher risk category than a patient diagnosed as BWA (129). Pathologist diagnosis for each ER was available within each case and was used as the ground-truth during analysis [see Methods, Section 6.4.1]. Using the same feature

extraction and training procedures as used to separate cancer from non-cancer in part (a) of this section, a binary classifier was developed for separating high-risk and low-risk groups. Once again 3-fold cross validation was employed to assess classifier accuracy. Classifier probability scores from all three trials were pooled together to generate an ROC curve for cross-validation [Methods, Section 6.4.6] which is illustrated in Fig. 6.5 (d). A cross-validation AUC of 0.81 was obtained for separating the high-risk and low-risk groups. Since pathologist agreement on BAH diagnosis through H&E stained tissue histopathology is low [concordance rate of 48% was reported in (15)] and often additional IHC based markers are needed to help with diagnosis (130), our cSLIM based markers can provide an additional channel of information to a pathologist, helping them determine whether or not the patient is high-risk and, thus, requires further investigations/procedures.

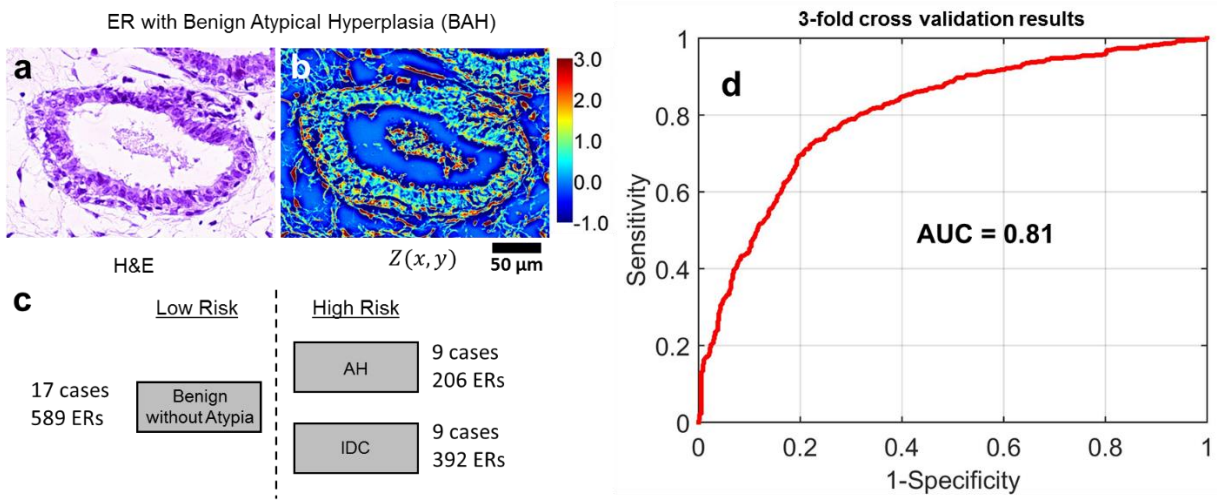

Figure. 6.5 (a) Bright field and **(b)** Normalized phase image of a benign ER with atypical ductal hyperplasia. **(c)** Study design for screening out high-risk cases from low risk cases **(d)** ROC for separating high-risk ERs from low risk ERs.

6.3.4 Collagen fiber orientation measurement on stained tissue

The prognostic value of tumor-adjacent collagen signatures (TACS) in breast tissue has been demonstrated in a number of studies (5, 111). Traditionally, these markers have been measured using SHGM which provides chemical specificity to collagen. However SHGM has disadvantages in that the tumor edge is difficult to identify due to low contrast in cellular structures and the acquisition speed is slower than conventional microscopy due to a point-scanning geometry (118). We demonstrated in ref. (118) and in Chapter 5 that SLIM phase images of unstained tissue can be used to quantify collagen fiber orientation in breast tissue. Here we demonstrate that the relative angle θ_r between collagen fibers near an ER edge and the tangent to the nearest point on the edge itself is detectable on stained tissue biopsies. θ_r is schematically illustrated in Fig. 6.6.

For the 30 cases selected from TMA-1 (used in the previous two sections) we measured θ_r in the $Z(x,y)$ maps of both stained and unstained tissue using an open source MATLAB based tool called CurveAlign (116) [see Methods Section 6.4.7 for details and parameter specifications]. All fibers within a distance of 63 μm from the ER edge were considered. This is within the range of the typical intercellular signaling distance reported in literature (116, 131). ERs in all cores were segmented out before computation of θ_r so that their cellular structures did not interfere with the process of collagen fiber extraction [see Section 6.4.2 of methods for details on ER segmentation].

Figure 6.6 compares the obtained results between unstained and stained tissue biopsies. Figures 6.6 (a) and (b) show the bright-field images of malignant and benign ERs whereas Figs. 6.6 (c), (d), (f) and (g) illustrate the fiber orientation in their vicinity. As evident from these images, values of θ_r are on average higher for malignant tissue than for benign. Furthermore, the orientation measured on stained tissue qualitatively matches that measured on unstained. Figures

6.6 (e) and (h) show the histograms of θ_r measured for all tumor adjacent fibers within the 30 core dataset. Once again not only are the values comparable between stained and unstained tissue samples but also in both cases malignant ERs show a greater probability of forming higher angles with their adjacent fibers. These measurements agree with previous results in literature where it was demonstrated that higher values of θ_r are associated with more aggressive disease and that aligned collagen fibers, oriented perpendicularly to tumor edge, facilitate local invasion (5). The results here are also significant because collagen fiber based parameters show similar values between stained and unstained normalized phase maps. This means that prognostic markers related to stromal fibers too can, potentially, be evaluated using cSLIM while simultaneously having access to bright-field standard histopathology images (as demonstrated in the next section).

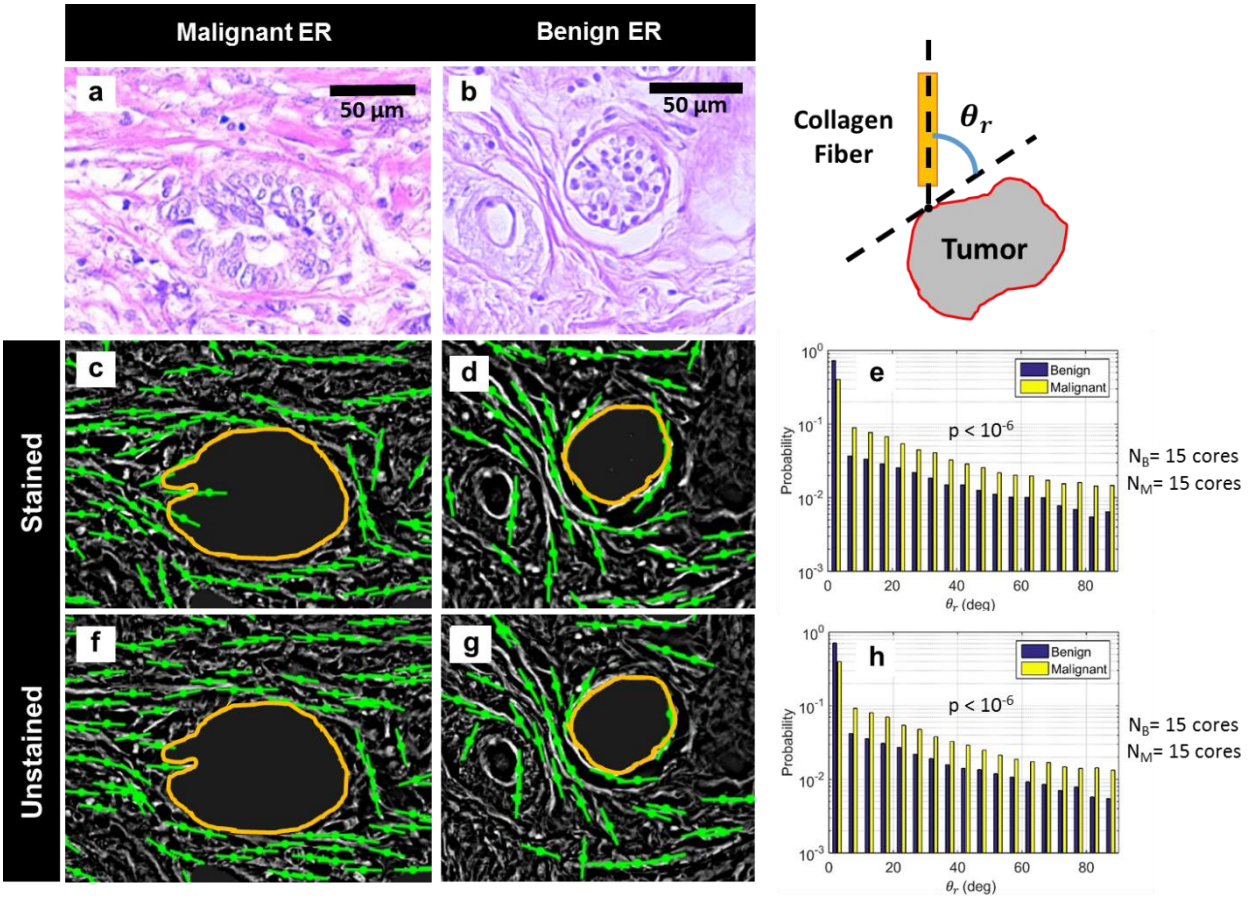

Figure 6.6 Comparison of relative collagen fiber angle θ_r between stained and unstained tissue biopsies. **(a)** and **(b)** Bright-field images of malignant and benign ERs, respectively. **(c)** and **(d)** Orientation of collagen fibers in stained tissue, in the vicinity of malignant and benign ERs, respectively. Fiber orientations are shown as green lines while the ER edge is marked in orange. **(e)** Normalized histogram of θ_r measured for all ERs within the stained tissue dataset (15 malignant and 15 benign cores). **(f)** and **(g)** Orientation of collagen fibers in unstained tissue in the vicinity of malignant and benign ERs, respectively. Fiber orientations are shown as green lines while the ER edge is marked in orange. **(h)** Normalized histogram of θ_r measured for all ERs within the unstained tissue dataset (15 malignant and 15 benign cores). p-values in both cases were computed using the two-sample Student's T-test.

6.3.5 Quantifying aligned collagen fibers in stained tissue for prognosis

Having demonstrated in the last section that fiber extraction and orientation measurement is possible in cSLIM images of stained tissue, in this section we formally measure the prognostic marker TACS3. TACS3 refers to the presence of aligned collagen fibers that terminate at the tumor edge at high (near perpendicular) values of relative angle θ_r. In Bredfeldt *et al.* (116), TACS3 was

measured using an automated, supervised learning scheme within a TMA imaged using SHGM. We imaged the same H&E stained TMA, referred to in the rest of the chapter as TMA-3, using cSLIM and extracted $Z(x,y)$ maps for each core. The analysis method from ref. (116) was then repeated on these maps to demonstrate that cSLIM can also detect TACS3. Details regarding TMA-3 have previously been published and are summarized in Section 6.4.1.

TMA-3 comprised 196 cases (1 core per case) of IDC with disease free survival (DFS) and disease specific survival (DSS) information available for each case (5). Using open-source MATLAB based tools CT-FIRE (116, 127, 132) and CurveAlign, features were computed for each fiber that was within a distance of $100\ \mu m$ from the tumor edge [see Section 6.4.9 for details on fiber extraction and feature computation]. Once again this distance was chosen bearing in mind the typical intercellular signaling distances reported in literature (131). For each core, the features extracted from each fiber were then combined to generate a feature vector for the core. Three core-level features were found to be most informative in distinguishing TACS3 positive and negative patients: mean of ε (mean nearest fiber alignment), mean of l (nearest distance of fiber from tumor edge) and skewness of θ_r. These features are listed in the table in Fig. 6.7 (a). Their detailed description has already been published (116, 127) and is also described in Methods, Section 6.4.9. Feature vectors for 10 cores marked as TACS positive and 10 cores marked as TACS3 negative [based on pathologist consensus (5)] were used as predictors for training a linear Support Vector Machine (SVM) classifier. The classifier was then used to classify all 196 cores as either TACS3 positive or TACS3 negative. Figure 6.7 (a) shows the difference in the feature means of groups classified as TACS3 positive and TACS3 negative. According to these mean values, cores classified as TACS3 positive have a higher probability of containing aligned fibers (high ε) that terminate at or near the tumor edge (low l). Furthermore, these cores have θ_r histograms that are

more positively skewed, reflecting an asymmetry due to more instances of high θ_r. These measurements agree with the pathologist definition of TACS3, indicating successful classification.

Survival analysis was carried out to test whether patients classified as TACS3 positive had significantly worse outcomes than those deemed TACS3 negative. Figure 6.7 summarizes the results of this analysis. Univariate cox proportional hazard regression and Kaplan-Meier estimates were used to compare survival between TACS3 positive and TACS3 negative cases. As shown in Fig. 6.7 (b), TACS3 positive patients had hazard ratios of greater than 2 and p-values < 0.05, representing a statistically significant chance of worse DSS and DFS outcomes. This trend is also evident in the Kaplan-Meier estimate of the DFS and DSS survival functions [Fig. 6.7 (c)] where TACS3 positive patients show significantly higher frequency of events. The p-values in this case were computed using the log-rank test (133). Finally we also computed the Pearson's correlation coefficient ρ between the computationally generated TACS3 scores on cSLIM images and manual scores generated by pathologists [see ref. (5) for details] . As shown in Fig. 6.7 (d), a positive correlation was measured in each case, indicating that the automated analysis extracted the same or similar histological markers as were observed by the pathologists manually.

a

Features used	$\mu_p - \mu_n$
Mean of ε	0.062
Mean of l	- 53 μm
Skewness of θ	0.11 deg

b

Univariate Cox Proportional Hazard Model		
	Hazard Ratio	P value
DSS	2.17	0.037
DFS	2.39	0.017

d

	ρ	P value
Manual Score 1	0.341	$<1 \times 10^{-6}$
Manual Score 2	0.350	$<1 \times 10^{-6}$
Manual Score 3	0.374	$<1 \times 10^{-6}$

c

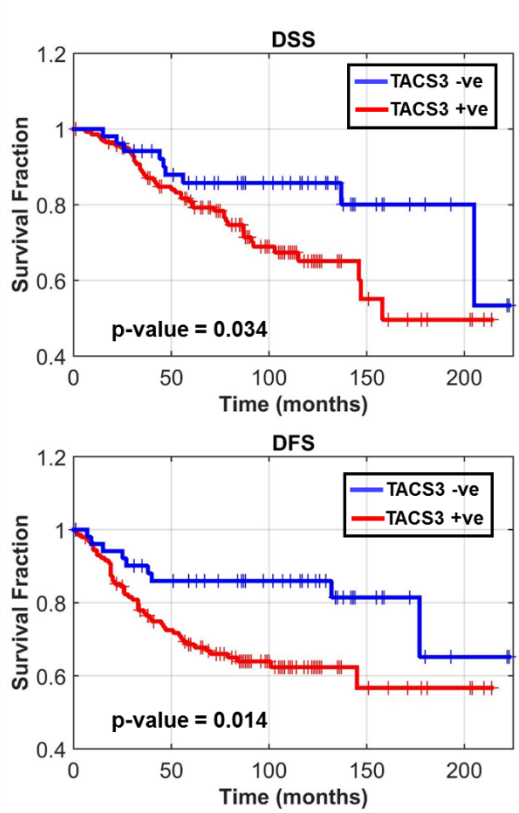

Figure 6.7. Results of survival analysis for TACS3 positive and TACS3 negative groups, classified based on fiber features measured from cSLIM $Z(x,y)$ maps. **(a)** Fiber features found to be most informative in classifying cores as positive or negative. μ_p and μ_n refer to the mean of these features for the groups classified as positive and negative, respectively. **(b)** Results of the univariate cox proportional hazard regression with TACS3 status as variable. **(c)** Kaplan-Meier estimate of survival function for DSS and DFS. Vertical tic marks represent right-censoring events. The number of cores classified as TAC3 negative were 52 and those classified as TACS3 positive were 144. **(d)** Pearson's correlation between the automated TACS3 scores and the 3 different manual pathologist scores (5).

Our results are significant because while TACS3 has been measured automatically using SHGM before, the cSLIM system provides important advantages over SHGM in terms of both speed and the fact that both phase and bright field images of epithelial tissue are obtainable in a single acquisition. As has been pointed out throughout this paper, a cSLIM based instrument will allow the assessment of traditional prognostic markers (e.g tumor grade and molecular subtype) as well as new prognostic markers (such as TACS3) in a single scan, posing modest new requirements

on instrument optics and no new requirements on sample preparation, compared with standard histopathology.

6.4 Methods

6.4.1 TMAs

TMA-1 was purchased unstained from US Biomax (Serial # BR1002) and comprised cases of IDC and normal benign tissue. The TMA was obtained from the manufacturer with all human subject identifiers removed and neither the author nor their institution were involved in the tissue collection. Details regarding this TMA have already been reported in ref. (87) and Chapter 4. For each case diagnosis was provided by the manufacturer's board certified pathologist through examination of both H&E stained tissue and IHC makers, both on parallel sections of tissue. After acquiring SLIM images, the TMA was H&E stained for cSLIM imaging using standard protocols (13). Before staining, the coverslip was removed from the slide and post-staining the slide was re-coverslipped using the same mounting medium as before (Xylene). As discussed in Results and Discussion, 15 cases of IDC and 15 cases of normal tissue (diagnosed as BWA by the manufacturer's pathologist) were randomly selected from the TMA for the studies discussed in this chapter. 1 core per case was available. Each biopsy core had a diameter of 1 mm and thickness of 5 μm. For the IDC cases, a second board certified pathologist also marked any benign regions within the tissue cores which were then excluded from the analysis. In this way, diagnosis of each ER within each core (BWA or IDC) was available.

TMA-2 was purchased, already H&E stained, from US Biomax (Serial # BR1003) and comprised cases of IDC, BAH and BWA. Within the BWA cases, cases of benign usual hyperplasia (BUH) were also available. The TMA was obtained from the manufacturer with all human subject identifiers removed and neither the author nor their institution were involved in the

tissue collection. This is the same TMA slide that was used in the study published in ref. (134). Each biopsy core had a diameter of 1 mm and thickness of 5 μm. For all cases in TMA-2, diagnosis was provided by the manufacturer through inspection by a board certified pathologist. The diagnosis was based on inspection of H&E stained tissue as well as evaluation of IHC based markers, on a parallel tissue section. For each core, the tissue block from which it was extracted was also examined to ensure correct diagnosis had been reached for the core. Since pathologist agreement on cases of BWA and IDC is high [reported as 97.1 and 97.7% in (129)] while that for BAH is low [<50% in (129)] the cores diagnosed as BAH by the first pathologist were re-examined by a second board certified pathologist. The second pathologist confirmed the BAH diagnosis of the first pathologist. Since we classify each ER as high risk/low risk in our method, all high-risk cores (IDC and BAH) were also examined by the second pathologist for low-risk regions (benign lesions without atypia), which were removed from analysis. In this way diagnosis for each ER (low-risk or high-risk) was available for all cases within TMA-2.

TMA-3 was used in previous studies by Bredfeldt *et al.* (116) and Conklin *et al.(5)*. Details regarding patient profiles, tissue processing and core selection have already been described in ref. (5). The dataset used from the TMA consisted of 196 cores (1 core per patient) and patients were followed up for a median time of 6.2 years, ranging from 1-223 months in order to determine patient outcomes. DSS and DFS information was available for each patient. DSS was defined as the time from diagnosis to death from breast cancer or date of last follow up evaluation. DFS was defined as the time from date of diagnosis to the first date of recurrence. The TMA-3 was H&E stained using standard protocols (13), allowing for simultaneous acquisition of both normalized phase and bright-field images using the cSLIM system. All tissue and patient information were obtained after approval by IRB (5).

Analysis of required sample size based on statistical power of 0.8 and two-sided p-value of 0.05 (using log-rank test) was performed using the method described in (135). Using the 10-year survival fractions in the Kaplan-Meier curves (Fig. 6.7) to compute the Hazard Ratio (135), the required sample size was estimated as N_{req} = 100 cases for DFS and N_{req} = 150 for DSS. These are both smaller than the 196 cases we used in our study. During this analysis proportions of TACS3 positive and TACS3 negative cases were based on the results of the SVM classifier (Section 6.3.5).

6.4.2 Epithelial tissue segmentation for feature extraction

For computation of epithelial features during supervised learning as well for measurement of relative fiber orientation, knowledge of the ER boundary is required. For TMA-1 and TMA-2, the ER boundaries were annotated in all the cores manually using the region-of-interest tool in ImageJ by using the H&E stained tissue bright-field images as a guide. Consistent criteria were used during annotation– groups of epithelial cells bounded by stroma on all side were considered a single ER. Other tissue components were considered part of the ER if surrounded on all sides by epithelial cells (87).

The ER segmentation procedure for TMA-3 has already been described in ref. (116). A supervised automated classification scheme, relying on features derived from tissue bright-field images, was used in that case. We used the same ER segmentation masks for the studies done in this chapter. Registration of $Z(x,y)$ maps with segmentation masks was carried out by first registering the cSLIM bright-field images with the bright-field images from the original study. Speed-Up Robust Features (SURF)(136) were extracted on both sets of bright-field images and an affine transform for registering them was found. This transform was then applied to the $Z(x,y)$ maps to register them with the ER segmentation masks.

6.4.3 SLM calibration with RGB camera

SLIM requires SLM calibration so the correct phase modulation is applied between the scattered and incident components of light (48). This calibration is different for different light spectra due to the wavelength dependent nature of the SLM liquid crystal response. The spectra of light in SLIM and cSLIM are different in terms of both spectral width and central wavelength. This illustrated in Fig. 6.8. Fig. 6.8 (a) compares the measured spectra of two modalities. The spectrum in SLIM is simply that of the illumination source whereas to obtain the cSLIM spectrum one has to multiply the illumination spectrum with the spectral response of the red, green and blue channels of cSLIM [see Eq. (A.1) in Appendix A]. From these spectra, which were measured as a function of wavelength λ, we obtain the frequency dependent spectra as function of angular frequency ω (which requires re-sampling and rescaling)(48). By taking the Fourier transform of these frequency spectra we obtain the temporal autocorrelations for both modalities, shown in Fig. 6.8 (b). The central wavelength λ_0 and the coherence length l_c extracted from these correlation functions are different: the cSLIM spectrum is slightly blue-shifted and the modality has a longer coherence length than the SLIM. l_c here is defined as the full-width half maximum (FWHM) of the envelope [dashed line in Fig. 6.8 (b)] of the autocorrelation function.

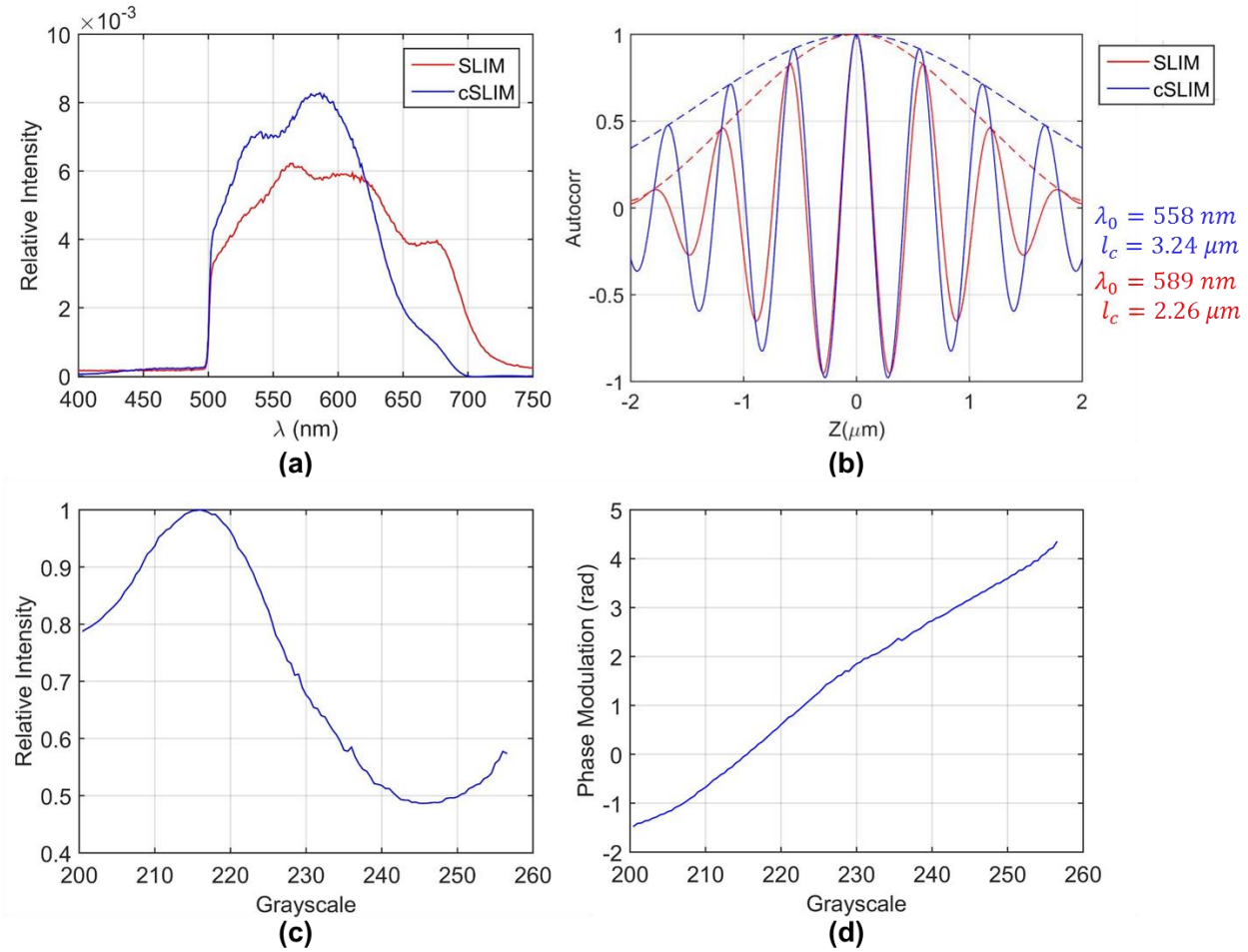

Figure 6.8 (a) Comparison of SLIM and cSLIM spectra. The raw spectra were normalized to make the sum over all wavelengths equal to 1. **(b)** Autocorrelation functions obtained by taking the Fourier transforms of the spectra in (a). **(c)** Amplitude (intensity) modulation curve obtained in cSLIM by configuring the SLM in amplitude mode. **(d)** Hilbert transform of the amplitude modulation curve in (c) provides the phase calibration.

For these reasons, recalibration of the SLM was required for the cSLIM system. After configuring the SLM in amplitude modulation mode (48), the 8 bit grayscale input to the SLM was scanned from 0-255. The corresponding amplitude modulation in $I(x,y;\varphi)$ was measured and each frame was averaged to generate a one dimensional amplitude modulation curve, shown in Fig. 6.8 (c). By taking the Hilbert transform of this curve, the SLM calibration curve, relating phase values to grayscale input, was obtained. The grayscale values corresponding to $\varphi = 0, \pi/2, \pi, 3\pi/2$ rad were used in all imaging experiments.

6.4.4 Attenuation calibration for bright-field objective

Phase contrast objectives contain a phase plate in their back focal planes that not only introduces a $\pi/2$ rad phase shift between the unscattered light U_0 and scattered light U_1 but also imparts an attenuation factor $\alpha_{pc} = \frac{|U_1|}{|U_0|}$. This factor is used during SLIM phase reconstruction while calculating the ratio of the amplitudes of the two interfering fields (48, 137). In our cSLIM experiments, we have used a bright-field objective that does not have this attenuating element. An equivalent value of attenuation, α_{bf}, was, therefore, used during phase reconstruction. α_{bf} was obtained through the following calibration procedure which is illustrated in Fig. 6.9. An unstained TMA core was imaged using cSLIM with both a phase contrast and bright-field objective. During phase reconstruction for the phase contrast case, the measured attenuation factor $\alpha_{pc} = 1.97$ was used and the raw phase image $\phi(x,y)$ was obtained [Fig. 6.9 (c)]. For the bright-field case the equivalent attenuation α_{bf} was numerically tuned and the phase $\phi(x,y)$ was obtained for each α_{bf}. For each α_{bf} the cross-correlation $\gamma(P_{pc}, P_{bf})$ between the probability distributions P_{pc} and P_{bf} of $\phi(x,y)$ in the phase contrast and bright-field cases, respectively, was measured (138). P_{pc} and P_{bf} were obtained by normalizing their respective image histograms (constructed with 512 bins each). As shown in Fig. 6.9 (b), $\gamma(P_{pc}, P_{bf})$ maximizes at $\alpha_{bf} = 3.4$ which was, thus, the value used for all subsequent imaging experiments. Fig. 6.9 (d) shows the phase image obtained using the bright-field objective at $\alpha_{bf} = 3.4$ which has similar values to the corresponding phase contrast objective image [Fig. 6.9 (c)].

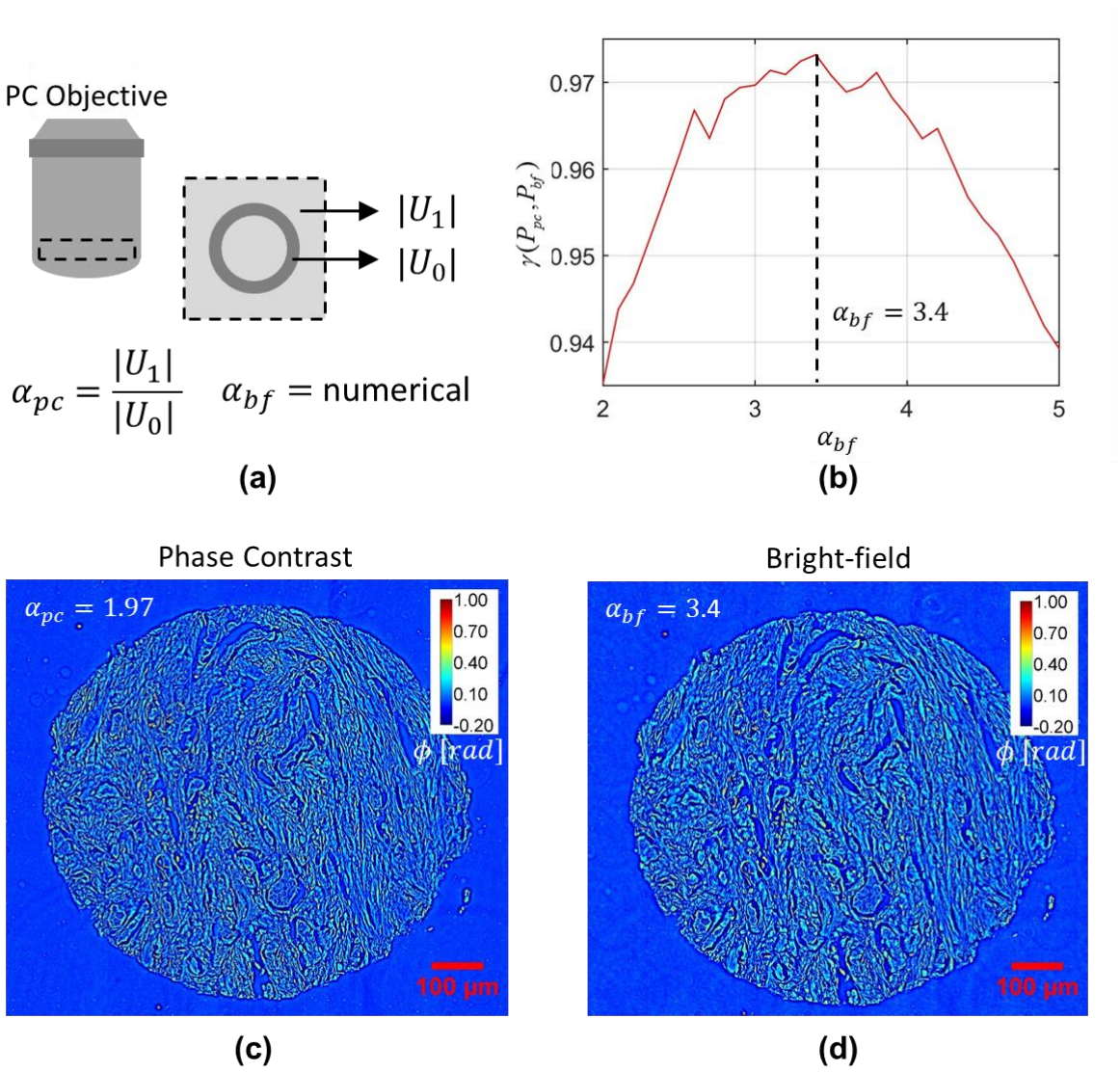

Figure 6.9 (a) Attenuation α_{pc} of the unscattered light U_0 with respect to scattered light U_1 in a phase contrast objective. For imaging with a bright-field objective this term is introduced numerically, α_{bf}. **(b)** Cross-correlation γ between the probability distributions P_{pc} and P_{bf} of the same unstained TMA core measured using phase contrast and bright-field objectives, respectively. γ is measured for different values of α_{bf} and maximizes at α_{bf} = 3.4. **(c)** cSLIM image of the unstained tissue core obtained using a phase contrast objective with the measured value of attenuation α_{pc} =1.97. **(d)** cSLIM image of the unstained tissue core obtained at the optimum value of α_{bf} = 3.4.

6.4.5 Procedure for stain normalization

As discussed in Results and Discussion Section 6.3.2, we extracted the normalized phase maps $Z(x,y)$ from the raw phase maps $\phi(x,y)$ generated by the cSLIM system, using Eq. (6.2). This computation is illustrated in Fig. 6.10. For each tissue core $\phi(x,y)$ map we first generated a segmentation mask [Fig. 6.10 (b)] using thresholding followed by morphological operations (morphological closing and removal of connected objects smaller than a certain number of pixels). A circular structural element for morphological closing was used and its diameter was determined iteratively. This mask was then used to calculate the mean μ and standard deviation σ of the foreground region in $\phi(x,y)$ (region occupied by tissue core). Finally, the $Z(x,y)$ image was computed for the core from these parameters as shown in Figs. 6.10 (c) and (d).

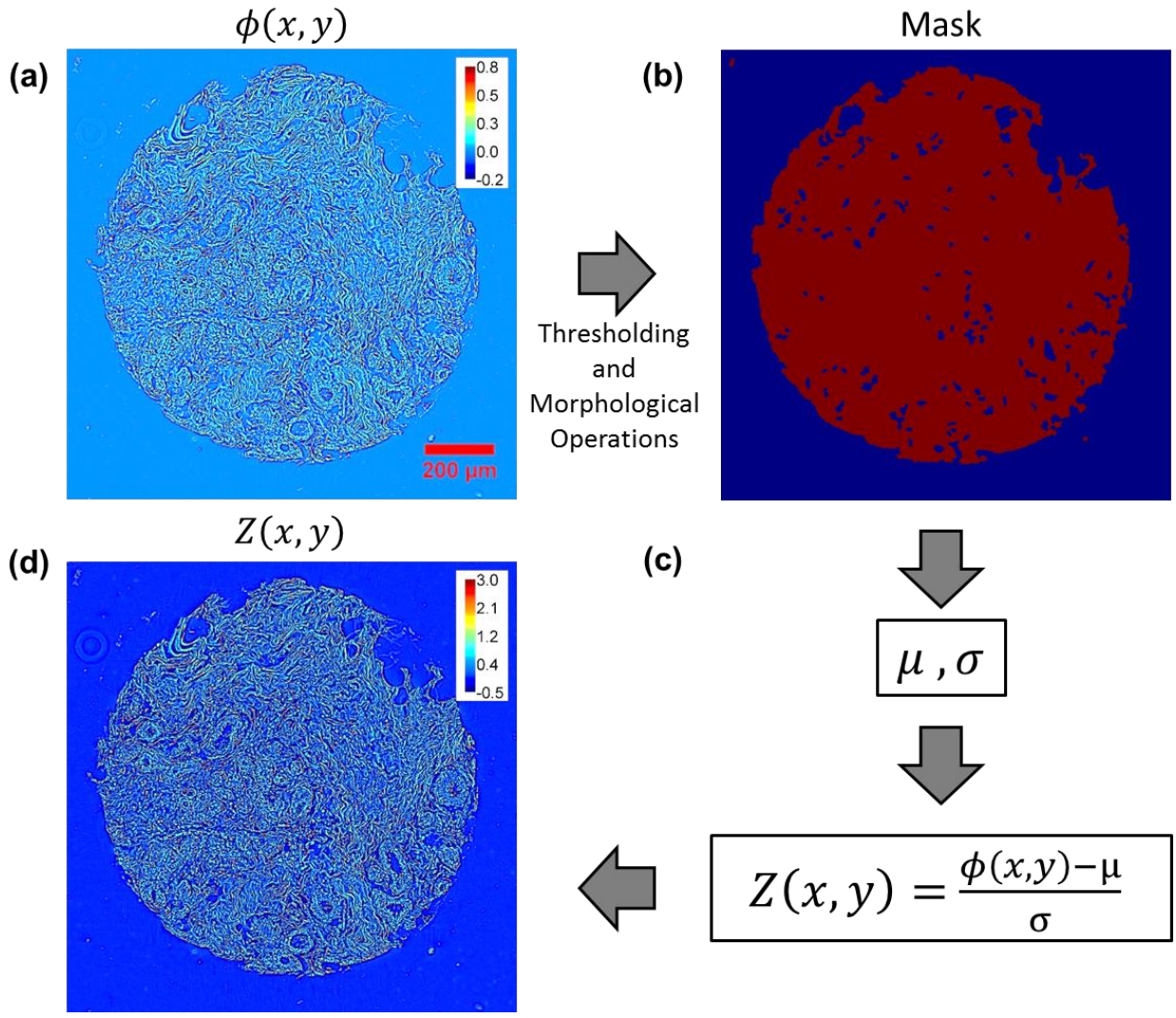

Figure 6.10. (a) Raw phase map of stained TMA core. **(b)** Mask for computation of μ and σ over foreground pixels. **(c)-(d)** Computation of normalized phase map.

6.4.6 Classification scheme for cancer diagnosis

The supervised classification of first benign versus malignant lesions, followed by low-risk versus high-risk lesions [Section 6.3.3 of Results and Discussion] is based on the procedure we reported in ref. (87) and described in Chapter 4. The procedure can be divided into three main steps: feature extraction, training and validation.

During feature extraction, first maps of the ER curvature C, mean scattering length l_s and texture vector T were extracted for each core within our datasets. The ER curvature C refers to the extrinsic curvature of a two-dimensional plane (in this case a benign or malignant ER) and can be construed as the magnitude of the rate of change of a vector tangent to the ER perimeter. We used an open-source MATLAB code to measure C for each annotated ER (89). The mean scattering length l_s is the length-scale over which a single scattering event happens on average and can be computed from tissue phase images using the scattering-phase theorem (57). The texture vector T consists of frequencies of elements known as 'textons' within the vicinity of a pixel in the image. Textons have been shown to be effective measures of the unique texture surrounding a pixel (25, 90, 91). For the straightforward benign versus malignant classification, contrary to our previous work where 50 textons were trained (resulting in a 50 dimensional vector T), we trained 30 textons due to the smaller size of the dataset (87). For classifying low-risk and high-risk lesions, once again 30 textons were trained. In each case, this number was obtained iteratively by measuring the cross-validation AUC (discussed below) while increasing the number of textons and stopping at the point where no improvement in AUC was noticed, to avoid overfitting. For feature extraction, all other parameters were identical to those used in ref. (87).

After pixel-wise computation of these features, the median over each ER was calculated for each feature $[<C>,<l_s>,<T>]$, using the ER masks obtained through manual segmentation [Section 6.4.2]. These were then concatenated to generate an overall (32 dimensional) feature vector for each ER. Using pathologist diagnosis for each ER as the class label (benign or malignant, low risk or high risk) and its overall feature vector as the predictor, an LDA classifier was trained. During validation, feature vectors for an unknown ER were input to the classifier which generated a likelihood score for the ER belonging to either class. The overall data set was partitioned into

three equal sets. Three validation trials were performed (3-fold cross validation) (93) and in each trial two sets were used for training and the remaining set for validation. The classifier performance was measured using ROC analysis. Likelihood scores for each ER, generated by the classifier from the three validation trials, were pooled together (95) to generate an overall ROC curve [Figs. 6.4 (i) and 6.5 (d)] and the area AUC was used as a metric for classifier accuracy.

6.4.7 Fiber orientation extraction on TMA-1 using CurveAlign

In Results and Discussion Section 6.3.4, we compared θ_r, the relative angle between the orientation of a collagen fiber and the tangent to the nearest point on the tumor edge (depicted in Fig. 6.6), between benign and malignant cases. The results were extracted using an open source MATLAB based tool called CurveAlign, algorithmic details of which have already been described in a number of publications (115, 116, 127, 139). For our analysis in Section 6.3.4, we chose the Curvelet Transform (CT) based fiber analysis method within CurveAlign. This method uses the curvelets provided by curvelet transformation (140) of the image to represent the edges of collagen fibers, without segmenting the individual fibers. From computation of these curvelets, thus, scale, location and relative orientation of each fiber can be calculated (127). Tiff files that contained masks of the ERs [obtained through manual annotation, described in Section 6.4.2] were used in the 'Boundary Method' field within CurveAlign. The fraction of coefficients to keep, during CT computation, was set at 0.005 and the distance from the tumor edge, up to which fibers are analyzed, was set to 100 pixels or approx. 63 μm. Before extraction of θ_r, ERs were segmented out from all the core images so that the cellular structures within them did not interfere with the process of fiber extraction during curvelet transformation.

6.4.8 TACS3 measurement on TMA-3 using CT-FIRE and CurveAlign

As described in Results and Discussion, for detecting the TACS3 prognostic marker on cSLIM $Z(x,y)$ maps the same general method as used in ref. (116) was employed. We summarize that analysis method here. First, the ERs within each core were segmented out using its corresponding segmentation mask [see Section 6.4.2]. This was carried out to ensure that during subsequent fiber segmentation, cell edges did not interfere. CT-FIRE was then used to segment out all fibers within the $Z(x,y)$ map of each core. Default parameters, as outlined in the CT-FIRE manual(132), were used except for the parameters labelled "thresh_im2" and "s_xlinkbox" for which values were set to 30 and 5 respectively. These fiber segmentation maps, along with ER segmentation masks, were then input to CurveAlign for extraction of fiber features. Features were computed for all fibers that were a distance of 100 μm from the tumor edge. In CurveAlign, the "CT-FIRE Fibers" fiber analysis method was chosen and the "TIFF Boundary" was chosen as the boundary method. CurveAlign extracts a total of 34 fiber features as part of its standard computation. These features are related to the fiber curvature, width, length, density, alignment, proximity to epithelium and relative angle to epithelial boundary (116). As discussed in the Results and Discussion, core-level statistics derived from 3 features (related to alignment, proximity to epithelium and relative angle) were found to be the best predictors of DSS and DFS. The first of these features was the mean nearest alignment ε, defined as the mean of the alignment of a fiber to its nearest 2, 4, 8 and 16 fibers. The algorithm for measuring the alignment of a fiber to its nearest neighbors has already been described in (116). The second feature used was the distance of each fiber to the nearest ER boundary, denoted l. The final feature was the relative fiber angle θ_r. Means of ε and l and skewness of θ_r, over each core, were used as predictors for SVM training [Section 6.3.5 of Results and Discussion].

For survival analysis, the Kaplan-Meier estimate was computed using an open-source MATLAB code (141).

6.5 Summary and Conclusion

In summary, we have presented in this chapter cSLIM, a tissue imaging modality that provides stain-independent, quantitative markers of disease while preserving traditional histopathology images. Our instrument makes clinical translation of our disease markers easier by posing no new sample preparation requirements and providing traditional and novel markers in a single acquisition. Due to its modular design, the cSLIM instrument also requires fewer additional optical components than other label-free techniques and has higher throughput. We demonstrated that cSLIM normalized phase maps are stain-independent by comparing the results of phase imaging of tissue before and after staining. We also demonstrated that diagnostic and prognostic markers relevant to breast cancer can be extracted from cSLIM images through automated machine learning techniques. Since these disease markers are quantitative, they eliminate subjectivity from tissue evaluation. Because the analysis is automated, disease markers can be obtained by pathologists rapidly and reproducibly. Furthermore, by providing a fast and convenient means of extracting stromal collagen based prognostic markers, our instrument can potentially help pathologists predict disease aggressiveness in patients for whom other more traditional disease markers fail.

Chapter 7: Thesis summary and future work

In summary, I have presented in this thesis instrumentation and computational tools that address some key limitations of/opportunities in traditional breast histopathology.

Traditional breast histopathology for diagnosis is qualitative and manual, resulting in inter-observer disagreement especially in cases that are difficult and when the tissue sample is small. The automated diagnosis scheme introduced in Chapter 4 relies on OPD based markers to perform quantitative histopathology for diagnosis. Relying on physical properties of tissue, this method performs an objective assessment of patient health and, being automated, can improve upon the throughput of existing evaluation methods. Previous attempts to quantify disease signatures for diagnosis have relied heavily on analysis of stained-dependent signals in images of tissue. The effect of stain variation complicates the process of automated detection in these approaches. While other label-free modalities have shown promise for breast cancer diagnosis, QPI has advantages over them in terms of speed, resolution, cost-effectiveness and compatibility with existing infrastructure in pathology labs. Furthermore, as I have demonstrated in Chapter 6, QPI can be used to obtain a stain-independent phase signal from stained tissue as well, which makes QPI based approaches even more attractive for clinical translation, once again due to the minimal disruption caused in existing methods.

Future studies on diagnosis, building on the methods and tools discussed in this thesis, need to be focused on two fronts. Firstly, while I have demonstrated that detection of IDC and stratification of benign lesions (with atypia vs without atypia) is feasible using QPI based imaging markers, other breast lesions need to be taken into consideration. Testing the algorithms described for diagnosis in Chapters 4 and 6 for classifying different invasive breast carcinomas (ductal,

lobular, tubular etc.) as well as for separating BAH from DCIS are important considerations for the future. Secondly, while we showed in Chapter 6 that breast cancer diagnosis on stained tissue is feasible using our OPD based feature set, the robustness of the approach needs to be tested against stain variation from slide to slide and laboratory to laboratory. Obtaining stained samples from different labs, with potentially different staining protocols, and testing the feature set on those samples would be an important next step.

On the prognosis front I have demonstrated in this thesis that tumor adjacent collagen-based prognostic markers can be detected using QPI of breast tissue. As discussed earlier, due to the heterogeneous nature of breast cancers, traditional prognostic markers do not provide sufficient information on disease aggressiveness for some patients and these novel markers can help pathologists make better treatment decisions for such patients. QPI provides a faster and more convenient means for extracting these stromal markers in tissue compared to other methods such as SHGM. I also demonstrated that algorithms used to extract collagen markers in unstained tissue biopsies also work for normalized phase images of stained tissue. Thus, detection of these markers on stained tissue not only obviates the need for additional sample preparation but also allows traditional epithelial prognostic markers to be observed simultaneously with markers in tumor adjacent stroma.

Futures studies related to imaging of collagen-based tissue biomarkers, extracted using QPI, can potentially look at correlations of these markers with other prognostic indicators such as histological grade and tumor molecular subtype. These studies can shed further light on epithelial-stromal interactions responsible for invasion and metastasis in breast tissue. Using the cSLIM system, which generates both bright-field and phase images of whole-slides rapidly, studies like these involving large patient cohorts are feasible. In addition, since the tumor microenvironment

influences tumor progression in carcinomas of other organs as well, analysis of collagen fibers in pancreatic, colon, ovarian and prostate cancer are also worth pursuing. Such analyses have already been performed to varying extents by other researchers (56, 72, 142) in the past but the algorithms and instrumentation discussed in this thesis provide an unprecedented ability to look at large case sets and merge traditional markers with novel ones.

Appendix A: Analysis of dispersion in stained tissue

As discussed in the main text, the spectra of SLIM and cSLIM are different due to the effect of the spectral responses of the red, green and blue channels of the cSLIM system. This results in different values of both central wavelength λ_0 and coherence length l_c for the two systems even in absence of a stained tissue sample [Fig. 6.8 (a) and (b)]. Due to differences in absorbance between different parts of H&E stained tissue, the cSLIM λ_0 and l_c are expected to change even further. Our results show that normalization of both stained and unstained tissue maps [using Eq. (6.2) in the main text] accounts for the differences between the SLIM and cSLIM spectra, making results from both modalities very similar. We discuss in this section reasons for why this normalization removes the stain dependent signal from phase images.

To explore this we first compute the pixel-wise spectra of light detected by the RGB camera when an H&E stained tissue core is imaged. From the bright-field image measured by the camera [illustrated in Fig. A.1 (a)] we extract the red, green and blue channel images, $R(x,y), G(x,y)$ and $B(x,y)$, respectively. By dividing each image by the average signal in a 30 x 30 pixel background region, we are able to obtain the transmission images for three channels: $T_R(x,y), T_G(x,y)$ and $T_B(x,y)$ [Fig. A.1 (b)]. Fig. A.1 (c) shows the spectral response of the cSLIM system, in the absence of tissue, for the red, green and blue channels [$S_R(\lambda), S_G(\lambda)$ and $S_B(\lambda)$, respectively]. This response includes both the filter response of the camera as well as the weights attached to the three channels numerically during computation of the equivalent grayscale image $I(x,y)$ [Eq. (6.1) in the main text]. Thus, the cSLIM spectrum for $I(x,y)$ is the sum

$$S_{cSLIM}(\lambda) = S_{ill}(\lambda)S_R(\lambda) + S_{ill}(\lambda)S_G(\lambda) + S_{ill}(\lambda)S_B(\lambda) \tag{A.1}$$

where $S_{ill}(\lambda)$ is the illumination source spectrum, which is also the spectrum for SLIM imaging. $S_{cSLIM}(\lambda)$ and $S_{ill}(\lambda)$ were also depicted earlier in Fig. 6.8 (a).

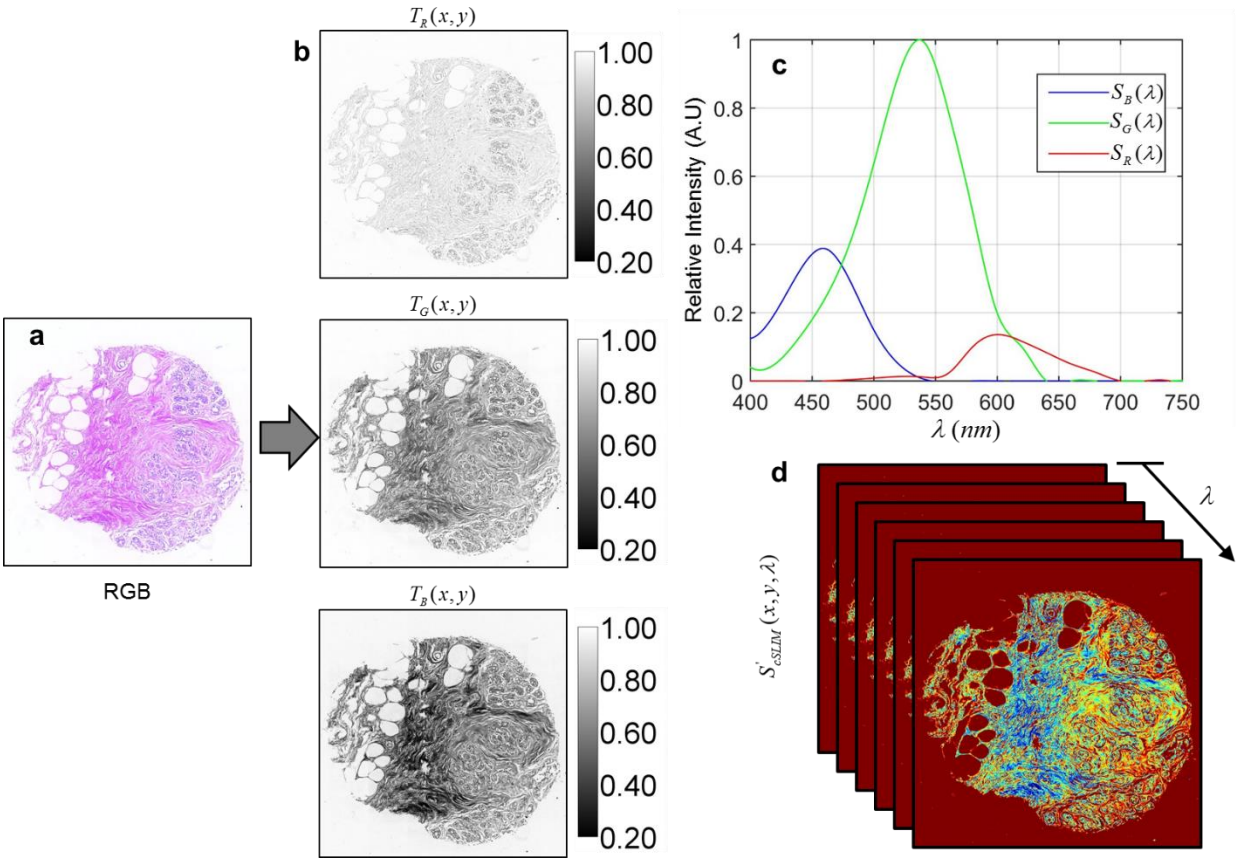

Figure. A.1 (a) Bright-field image of a stained TMA core. **(a)** Transmission maps for the red, green and blue channels. **(c)** Spectral response of cSLIM for the red, green and blue channels. **(d)** cSLIM spectrum at each pixel computed using Eq. (S2).

Assuming constant values of transmission for each spectral channel per pixel [$T_R(x,y)$, $T_G(x,y)$ and $T_B(x,y)$] the spectral response for each channel in the presence of stained tissue can be calculated as - $S'_i(x,y,\lambda) = S_i(\lambda)T_i(x,y)$ where $i = R,G,B$. Multiplying each response by the illumination spectrum $S_{ill}(\lambda)$ and summing them gives us the pixel-wise cSLIM spectrum in the presence of tissue as

$$S'_{cSLIM}(x,y,\lambda) = S_{ill}(\lambda)S'_R(x,y,\lambda) + S_{ill}(\lambda)S'_G(x,y,\lambda) + S_{ill}(\lambda)S'_B(x,y,\lambda). \quad \text{(A.2)}$$

This 3d spectrum is illustrated in Fig. A.1 (d). From $S'_{cSLIM}(x,y,\lambda)$ we can compute the central wavelength map $\lambda_0(x,y)$ for the tissue core. By subtracting the mean value of λ_0 in a 30 x 30 pixel background region from $\lambda_0(x,y)$, we obtain the wavelength shift image $\delta\lambda_0(x,y)$, illustrated in Fig. A.2 (a). This image shows that dispersion (variation of λ_0 in x and y) due to tissue absorbance is small. This is quantified by the histogram (computed over the foreground region consisting of tissue only) in Fig. A.2 (b) which shows a mean shift of 2.3 nm with a standard deviation of 1.5 nm. Dispersion also causes changes in coherence length l_c across the tissue. The image $l_c(x,y)$ can be obtained from $S'_{cSLIM}(x,y,\lambda)$ by computing its autocorrelation function through Fourier transformation and measuring the FWHM of the function's envelope [see Section 6.4.3]. The shift in coherence length $\delta l_c(x,y)$ can be extracted from $l_c(x,y)$ by subtracting from it the mean value of l_c in a 30 x 30 pixel background region. $\delta l_c(x,y)$ is shown in Fig. A.2 (c) and its histogram is shown in Fig. A.2 (d). A mean shift in l_c of $-81.0\,nm$ and a standard deviation of $58.3\,nm$ was measured through this analysis.

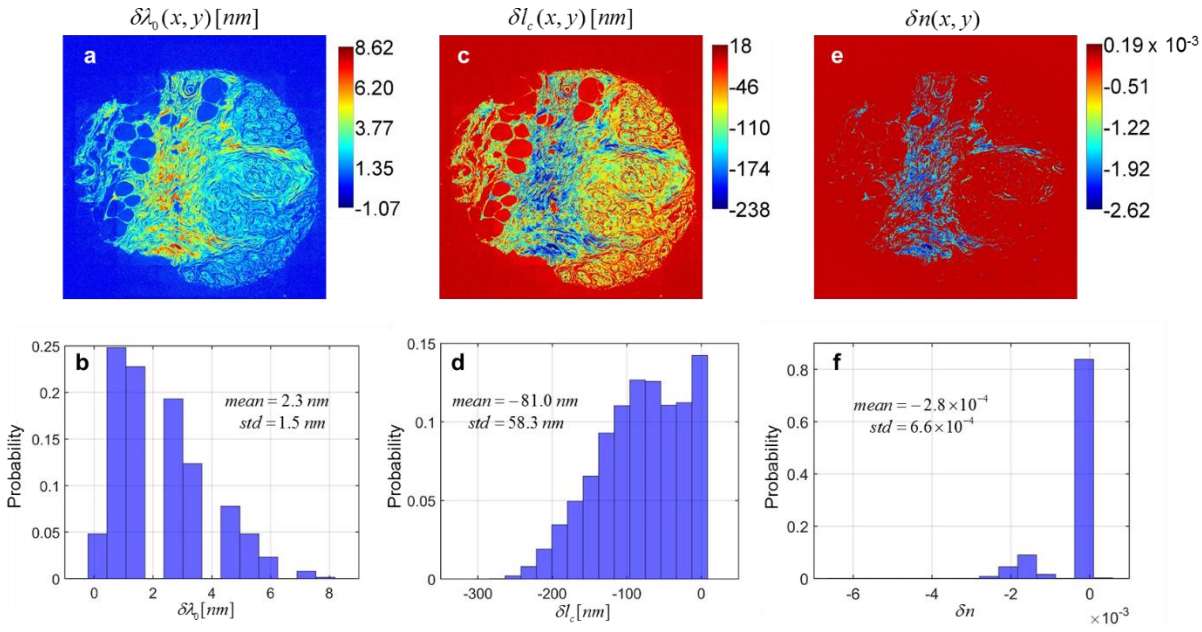

Figure A.2 (a) Wavelength shift across the tissue core due to dispersion. **(b)** Normalized histogram of the image in (a) over the foreground (tissue region). **(c)** Shift in coherence length across tissue core due to dispersion. **(d)** Normalized histogram of the image in (c) over the foreground (tissue region). **(e)** Dispersion (shift in refractive index) in the stained tissue core. **(f)** Normalized histogram of the image in (e) over the foreground (tissue region).

This spectral analysis sheds light on why a simple division by the standard deviation of $\phi(x,y)$ results in the stain-independent map $Z(x,y)$ [Eq. (6.2) in main text]. To begin with the slight difference in central wavelength between SLIM and cSLIM (589 nm vs 558 nm, see Section 6.4.3) would indicate that cSLIM should have different phase values even in the absence of tissue absorbance. However, division of $\phi(x,y)$ by its standard deviation removes the wavelength dependent $1/\lambda_0$ factor (27):

$$\phi(x,y) = \frac{2\pi}{\lambda_0}\left[\Delta n(x,y)t\right], \tag{A.3a}$$

$$Z(x,y) = \frac{n(x,y) - mean\{n(x,y)\}}{std\{n(x,y)\}}, \tag{A.3b}$$

accounting for the central wavelength difference between cSLIM and SLIM. In Eq. (A.3a), $\Delta n(x,y) = n(x,y) - n_0$ refers to the pixel-wise difference between the refractive index of the tissue $n(x,y)$ and that of the surrounding medium n_0. t is the thickness of the tissue section, assumed for simplicity to be constant. This assumption is reasonable for tissue biopsies that are cut to thin (4-5 μm) sections for histopathology (52, 56). Here it is also assumed that refractive index is independent of wavelength which is a reasonable assumption, in the absence of tissue absorbance, for the small difference in the two central wavelengths between SLIM and cSLIM.

However, in presence of stained tissue, λ_0 itself is x and y dependent and does not cancel out when $\phi(x,y)$ is divided by its standard deviation. The normalized phase image for cSLIM in this situation, Z', is thus given by

$$Z'\left[x,y,\lambda_0(x,y)\right] = \frac{\dfrac{\Delta n\left[x,y,\lambda_0(x,y)\right]}{\lambda_0(x,y)} - mean\left\{\dfrac{\Delta n\left[x,y,\lambda_0(x,y)\right]}{\lambda_0(x,y)}\right\}}{std\left\{\dfrac{\Delta n\left[x,y,\lambda_0(x,y)\right]}{\lambda_0(x,y)}\right\}} \tag{A.4a}$$

$$Z'[x,y,\lambda(x,y)] = \frac{\dfrac{\Delta n(x,y,\lambda_{cSLIM}) + \delta n[x,y,\delta\lambda_0(x,y)]}{\lambda_{cSLIM} + \delta\lambda_0(x,y)} - mean\left\{\dfrac{\Delta n(x,y,\lambda_{cSLIM}) + \delta n[x,y,\delta\lambda_0(x,y)]}{\lambda_{cSLIM} + \delta\lambda_0(x,y)}\right\}}{std\left\{\dfrac{\Delta n(x,y,\lambda_{cSLIM}) + \delta n[x,y,\delta\lambda_0(x,y)]}{\lambda_{cSLIM} + \delta\lambda_0(x,y)}\right\}} \tag{A.4b}$$

where λ_{cSLIM} is the cSLIM central wavelength (λ_0 = 558 nm) in the absence of tissue dispersion, $\delta\lambda_0$ is the shift in central wavelength caused by staining and δn is the shift in tissue refractive index due to stain induced dispersion.

Eqs. A.4 (a) and A.4 (b) would indicate the need for a local normalization constant rather than the global one we have used in our study. However, if $\delta\lambda_0$ and δn are small valued and/or have weak x and y dependence, $Z' \approx Z$. As shown in Fig. A.2, the x and y dependence of $\delta\lambda_0$

is small (standard deviation of 1.7 nm over the image). To determine this for δn, the following procedure was employed. The 3d spectrum $S'_{cSLIM}(x,y,\lambda)$, was first rescaled and resampled to obtain the frequency spectrum $S'_{cSLIM}(x,y,\omega)$ where $\omega = \frac{2\pi c}{\lambda}$, c being the speed of light. The same was done to $S_{cSLIM}(\lambda)$ to obtain $S_{cSLIM}(\omega)$. The transmission spectrum $T(x,y,\omega)$ was then obtained as

$$T(x,y,\omega) = \frac{S'_{cSLIM}(x,y,\omega)}{S_{cSLIM}(\omega)}. \tag{A.5}$$

From the transmission spectrum, the refractive index $n(x,y,\lambda)$ can be obtained by using the Hilbert transform relationship between the real and imaginary parts of the electric susceptibility (143, 144). The procedure for this is outlined in ref. (143). The resulting refractive index is determined only up to an additive constant since the Hilbert transform of a constant is zero. Since we have knowledge of the central wavelength at each pixel [given by $\lambda_0(x,y)$], the refractive index map $n(x,y)$ at this central wavelength can be computed from $n(x,y,\lambda)$. Finally, by subtracting the refractive index map in absence of dispersion, $n(x,y,\lambda_{cSLIM} = 558\,nm)$, from $n(x,y)$ we get the shift in refractive index due to tissue absorption $\delta n(x,y)$. This subtraction also accounts for the differences in additive constants across the $n(x,y)$ map caused by the computation of an independent Hilbert transform per pixel. $\delta n(x,y)$ is shown in Fig. A.2 (e) whereas Fig. A.2 (f) shows its histogram, once again computed only over the foreground (tissue region). As shown, not only is there a small shift in refractive index due to dispersion in tissue but the x and y dependence is also weak (standard deviation of 6.6 x 10^{-4}).

We, therefore, conclude that our normalization works well despite tissue dispersion because of the small change in λ_0, and thus in refractive index n, across the tissue core. Any

constant (spatially invariant) changes in both wavelength and refractive index are accounted for in $Z(x, y)$ by subtraction by the mean and division by the standard deviation of the raw phase $\phi(x, y)$.

References

1. Cancer Fact Sheets: Breast Cancer: International Agency for Research on Cancer - World Health Organization. Available from: http://gco.iarc.fr/today/fact-sheets-cancers?cancer=15&type=0&sex=2.
2. Lauby-Secretan B, Scoccianti C, Loomis D, Benbrahim-Tallaa L, Bouvard V, Bianchini F, Straif K. Breast-Cancer Screening — Viewpoint of the IARC Working Group. New England Journal of Medicine. 2015;372(24):2353-8.
3. Fernandez DC, Bhargava R, Hewitt SM, Levin IW. Infrared spectroscopic imaging for histopathologic recognition. Nat Biotech. 2005;23(4):469-74.
4. Taneja P, Maglic D, Kai F, Zhu S, Kendig RD, Fry EA, Inoue K. Classical and Novel Prognostic Markers for Breast Cancer and their Clinical Significance. Clinical Medicine Insights Oncology. 2010;4:15-34.
5. Conklin MW, Eickhoff JC, Riching KM, Pehlke CA, Eliceiri KW, Provenzano PP, Friedl A, Keely PJ. Aligned Collagen Is a Prognostic Signature for Survival in Human Breast Carcinoma. The American Journal of Pathology. 2011;178(3):1221-32.
6. Weigelt B, Peterse JL, van't Veer LJ. Breast cancer metastasis: markers and models. Nat Rev Cancer. 2005;5(8):591-602.
7. Cancer Facts & Figures. Atlanta: American Cancer Society, 2018.
8. Society AC. Cancer Prevention & Early Detection Facts & Figures 2017-2018. Atlanta: American Cancer Society, 2017.
9. Rakha EA, Ahmed MA, Aleskandarany MA, Hodi Z, Lee AH, Pinder SE, Ellis IO. Diagnostic concordance of breast pathologists: lessons from the National Health Service Breast Screening Programme Pathology External Quality Assurance Scheme. Histopathology. 2017;70(4):632-42.
10. Rakha EA, Reis-Filho JS, Baehner F, Dabbs DJ, Decker T, Eusebi V, Fox SB, Ichihara S, Jacquemier J, Lakhani SR, Palacios J, Richardson AL, Schnitt SJ, Schmitt FC, Tan P-H, Tse GM, Badve S, Ellis IO. Breast cancer prognostic classification in the molecular era: the role of histological grade. Breast Cancer Research : BCR. 2010;12(4):207.
11. Canene-Adams K. Chapter Fifteen - Preparation of Formalin-fixed Paraffin-embedded Tissue for Immunohistochemistry. In: Lorsch J, editor. Methods in Enzymology: Academic Press; 2013. p. 225-33.
12. Wissozky N. Ueber das Eosin als Reagens auf Hämoglobin und die Bildung von Blutgefässen und Blutkörperchen bei Säugethier-und Hühnerembryonen. Archiv für mikroskopische Anatomie. 1877:479-97.
13. Fischer AH, Jacobson KA, Rose J, Zeller R. Hematoxylin and Eosin Staining of Tissue and Cell Sections. Cold Spring Harbor Protocols. 2008;2008(5):pdb.prot4986.
14. de Matos LL, Trufelli DC, de Matos MGL, da Silva Pinhal MA. Immunohistochemistry as an Important Tool in Biomarkers Detection and Clinical Practice. Biomarker Insights. 2010;5:9-20.
15. Elmore JG, Longton GM, Carney PA, et al. Diagnostic concordance among pathologists interpreting breast biopsy specimens. JAMA. 2015;313(11):1122-32.
16. Van Eycke Y-R, Allard J, Salmon I, Debeir O, Decaestecker C. Image processing in digital pathology: an opportunity to solve inter-batch variability of immunohistochemical staining. Scientific Reports. 2017;7:42964.

17. Bejnordi BE, Litjens G, Timofeeva N, Otte-Holler I, Homeyer A, Karssemeijer N, van der Laak JA. Stain Specific Standardization of Whole-Slide Histopathological Images. IEEE Trans Med Imaging. 2016;35(2):404-15.
18. Bancroft JD, Gamble M. Theory and Practice of Histological Techniques. New York: Elsevier Health Science; 2008. 744 p.
19. Gurcan MN, Boucheron L, Can A, Madabhushi A, Rajpoot N, Yener B. Histopathological Image Analysis: A Review. IEEE reviews in biomedical engineering. 2009;2:147-71.
20. Veta M, Pluim JPW, Diest PJv, Viergever MA. Breast Cancer Histopathology Image Analysis: A Review. IEEE Transactions on Biomedical Engineering. 2014;61(5):1400-11.
21. Turashvili G, Brogi E. Tumor Heterogeneity in Breast Cancer. Frontiers in Medicine. 2017;4:227.
22. Koren S, Bentires-Alj M. Breast Tumor Heterogeneity: Source of Fitness, Hurdle for Therapy. Mol Cell. 2015;60(4):537-46.
23. Bianchini G, Balko JM, Mayer IA, Sanders ME, Gianni L. Triple-negative breast cancer: challenges and opportunities of a heterogeneous disease. Nature Reviews Clinical Oncology. 2016;13:674.
24. Kutomi G, Mizuguchi T, Satomi F, Maeda H, Shima H, Kimura Y, Hirata K. Current status of the prognostic molecular biomarkers in breast cancer: A systematic review. Oncology Letters. 2017;13(3):1491-8.
25. Nguyen TH, Sridharan S, Macias V, Kajdacsy-Balla A, Melamed J, Do MN, Popescu G. Automatic Gleason grading of prostate cancer using quantitative phase imaging and machine learning. Journal of Biomedical Optics. 2017;22(3):036015.
26. Llorà X, Priya A, Bhargava R. Observer-invariant histopathology using genetics-based machine learning. Natural Computing. 2009;8(1):101-20.
27. Popescu G. Quantitative Phase Imaging of Cells and Tissues. New York: McGraw Hill; 2011. 362 p.
28. Mertz J. Introduction to Optical Microscopy. Greenwood Village (CO): Roberts and Company; 2010. 413 p
29. Lichtman JW, Conchello J-A. Fluorescence microscopy. Nature Methods. 2005;2:910.
30. Zernike F. Phase contrast, a new method for the microscopic observation of transparent objects. Physica. 1942;9(7):686-98.
31. Majeed H, Sridharan S, Mir M, Ma L, Min E, Jung W, Popescu G. Quantitative phase imaging for medical diagnosis. Journal of Biophotonics. 2017;10(2):177-205.
32. Popescu G, Park Y, Lue N, Best-Popescu C, Deflores L, Dasari RR, Feld MS, Badizadegan K. Optical imaging of cell mass and growth dynamics. American Journal of Physiology - Cell Physiology. 2008;295(2):C538-C44.
33. Barer R. Interference microscopy and mass determination. Nature. 1952;169(4296):366-7.
34. Davies HG, Wilkins MH. Interference microscopy and mass determination. Nature. 1952;169(4300):541.
35. Mir M, Wang Z, Shen Z, Bednarz M, Bashir R, Golding I, Prasanth SG, Popescu G. Optical measurement of cycle-dependent cell growth. Proceedings of the National Academy of Sciences. 2011;108(32):13124-9.

36. Cooper KL, Oh S, Sung Y, Dasari RR, Kirschner MW, Tabin CJ. Multiple phases of chondrocyte enlargement underlie differences in skeletal proportions. Nature. 2013;495(7441):375-8.
37. Rappaz B, Barbul A, Emery Y, Korenstein R, Depeursinge C, Magistretti PJ, Marquet P. Comparative study of human erythrocytes by digital holographic microscopy, confocal microscopy, and impedance volume analyzer. Cytometry Part A. 2008;73A(10):895-903.
38. Wang R, Wang Z, Millet L, Gillette MU, Levine A, Popescu G. Dispersion-relation phase spectroscopy of intracellular transport. Optics Express. 2011;19(21):20571-9.
39. Rappaz B, Charrière F, Depeursinge C, Magistretti PJ, Marquet P. Simultaneous cell morphometry and refractive index measurement with dual-wavelength digital holographic microscopy and dye-enhanced dispersion of perfusion medium. Optics Letters. 2008;33(7):744-6.
40. Born M, Wolf E. Principles of Optics: Electromagnetic Theory of Propagation, Interference and Diffraction of Light. 2nd ed. New York (NY): Pergamon Press; 1964. 808 p.
41. Shechtman Y, Eldar YC, Cohen O, Chapman HN, Jianwei M, Segev M. Phase Retrieval with Application to Optical Imaging: A contemporary overview. Signal Processing Magazine, IEEE. 2015;32(3):87-109.
42. Ikeda T, Popescu G, Dasari RR, Feld MS. Hilbert phase microscopy for investigating fast dynamics in transparent systems. Optics Letters. 2005;30(10):1165-7.
43. Cuche E, Bevilacqua F, Depeursinge C. Digital holography for quantitative phase-contrast imaging. Optics Letters. 1999;24(5):291-3.
44. Cuche E, Marquet P, Depeursinge C. Simultaneous amplitude-contrast and quantitative phase-contrast microscopy by numerical reconstruction of Fresnel off-axis holograms. Applied Optics. 1999;38(34):6994-7001.
45. Kim MK. Digital Holographic Microscopy. In: Digital Holographic Microscopy: Principles, Techniques, and Applications. New York (NY): Springer New York; 2011. p. 149-90.
46. Majeed H, Sridharan S, Mir M, Ma L, Min E, Jung W, Popescu G. Quantitative phase imaging for medical diagnosis: Supporting Information. Journal of Biophotonics. 2016.
47. Bhaduri B, Edwards C, Pham H, Zhou R, Nguyen TH, Goddard LL, Popescu G. Diffraction phase microscopy: principles and applications in materials and life sciences. Adv Opt Photon. 2014;6(1):57-119.
48. Wang Z, Millet L, Mir M, Ding H, Unarunotai S, Rogers J, Gillette MU, Popescu G. Spatial light interference microscopy (SLIM). Optics Express. 2011;19(2):1016-26. doi: 10.1364/OE.19.001016.
49. Kim T, Zhou R, Mir M, Babacan SD, Carney PS, Goddard LL, Popescu G. White-light diffraction tomography of unlabelled live cells. Nat Photon. 2014;8(3):256-63.
50. Kandel ME, Sridharan S, Liang J, Luo Z, Han K, Macias V, Shah A, Patel R, Tangella K, Kajdacsy-Balla A, Guzman G, Popescu G. Label-free tissue scanner for colorectal cancer screening. Journal of Biomedical Optics. 2017;22(6):066016.
51. Majeed H, Kandel ME, Han K, Luo Z, Macias V, Tangella K, Balla A, Popescu G. Breast cancer diagnosis using spatial light interference microscopy. Journal of Biomedical Optics. 2015;20(11):111210.
52. Wang Z, Tangella K, Balla A, Popescu G. Tissue refractive index as marker of disease. Journal of Biomedical Optics. 2011;16(11):116017.
53. Lue N, Bewersdorf J, Lessard MD, Badizadegan K, Dasari RR, Feld MS, Popescu G. Tissue refractometry using Hilbert phase microscopy. Optics Letters. 2007;32(24):3522-4.

54. Wang P, Bista R, Bhargava R, Brand RE, Liu Y. Spatial-domain low-coherence quantitative phase microscopy for cancer diagnosis. Optics Letters. 2010;35(17):2840-2.
55. Takabayashi M, Majeed H, Kajdacsy-Balla A, Popescu G. Disorder strength measured by quantitative phase imaging as intrinsic cancer marker in fixed tissue biopsies. PLOS ONE. 2018;13(3):e0194320.
56. Sridharan S, Macias V, Tangella K, Kajdacsy-Balla A, Popescu G. Prediction of Prostate Cancer Recurrence Using Quantitative Phase Imaging. Scientific Reports. 2015;5:9976.
57. Wang Z, Ding H, Popescu G. Scattering-phase theorem. Optics letters. 2011;36(7):1215-7.
58. Uttam S, Pham HV, LaFace J, Leibowitz B, Yu J, Brand RE, Hartman DJ, Liu Y. Early Prediction of Cancer Progression by Depth-Resolved Nanoscale Mapping of Nuclear Architecture from Unstained Tissue Specimens. Cancer Research. 2015;75(22):4718-27.
59. Berthomieu C, Hienerwadel R. Fourier transform infrared (FTIR) spectroscopy. Photosynthesis Research. 2009;101(2):157-70.
60. Kwak JT, Kajdacsy-Balla A, Macias V, Walsh M, Sinha S, Bhargava R. Improving Prediction of Prostate Cancer Recurrence using Chemical Imaging. Scientific Reports. 2015;5:8758.
61. Argov S, Ramesh J, Salman A, Sinelnikov I, Goldstein J, Guterman H, Mordechai S, editors. Diagnostic potential of FTIR microspectroscopy and advanced computational methods in colon cancer patients2002: SPIE.
62. Dong L, Sun X, Chao Z, Zhang S, Zheng J, Gurung R, Du J, Shi J, Xu Y, Zhang Y, Wu J. Evaluation of FTIR spectroscopy as diagnostic tool for colorectal cancer using spectral analysis. Spectrochimica Acta Part A: Molecular and Biomolecular Spectroscopy. 2014;122:288-94.
63. Benard A, Desmedt C, Smolina M, Szternfeld P, Verdonck M, Rouas G, Kheddoumi N, Rothe F, Larsimont D, Sotiriou C, Goormaghtigh E. Infrared imaging in breast cancer: automated tissue component recognition and spectral characterization of breast cancer cells as well as the tumor microenvironment. Analyst. 2014;139(5):1044-56.
64. Walsh MJ, Holton SE, Kajdacsy-Balla A, Bhargava R. Attenuated total reflectance Fourier-transform infrared spectroscopic imaging for breast histopathology. Vibrational Spectroscopy. 2012;60:23-8.
65. Michael J, Joannie D, Kelly A, Karl S-A, Wendy-Julie M, Etienne De M, Marie-Christine G, Dominique T, Brian CW, Kevin P, Frederic L. A review of Raman spectroscopy advances with an emphasis on clinical translation challenges in oncology. Physics in Medicine & Biology. 2016;61(23):R370.
66. Abramczyk H, Brozek-Pluska B, Surmacki J, Jablonska-Gajewicz J, Kordek R. Raman 'optical biopsy' of human breast cancer. Progress in Biophysics and Molecular Biology. 2012;108(1):74-81.
67. Chowdary MVP, Kumar KK, Kurien J, Mathew S, Krishna CM. Discrimination of normal, benign, and malignant breast tissues by Raman spectroscopy. Biopolymers. 2006;83(5):556-69.
68. Wang L, Fan JH, Guan ZF, Liu Y, Zeng J, He DL, Huang LQ, Wang XY, Gong HL. Study on bladder cancer tissues with raman spectroscopy. Guang Pu Xue Yu Guang Pu Fen Xi/Spectroscopy and Spectral Analysis. 2012;32(1):123-6.
69. Hutchings JC, Kendall CA, Shepherd N, Barr H, Stone N. Evaluation of linear discriminant analysis for automated Raman histological mapping of esophageal high-grade dysplasia. Journal of Biomedical Optics. 2010;15(6): 066015.

70. Campagnola P. Second Harmonic Generation Imaging Microscopy: Applications to Diseases Diagnostics. Analytical chemistry. 2011;83(9):3224-31.
71. Ambekar R, Lau T-Y, Walsh M, Bhargava R, Toussaint KC. Quantifying collagen structure in breast biopsies using second-harmonic generation imaging. Biomedical Optics Express. 2012;3(9):2021-35.
72. Drifka CR, Loeffler AG, Mathewson K, Keikhosravi A, Eickhoff JC, Liu Y, Weber SM, Kao WJ, Eliceiri KW. Highly aligned stromal collagen is a negative prognostic factor following pancreatic ductal adenocarcinoma resection. Oncotarget. 2016;7(46):76197-213.
73. Tilbury KB, Campbell KR, Eliceiri KW, Salih SM, Patankar M, Campagnola PJ. Stromal alterations in ovarian cancers via wavelength dependent Second Harmonic Generation microscopy and optical scattering. BMC Cancer. 2017;17(1):102.
74. Nguyen TH, Kandel M, Shakir HM, Best-Popescu C, Arikkath J, Do MN, Popescu G. Halo-free Phase Contrast Microscopy. Scientific Reports. 2017;7:44034.
75. Kandel ME, Fanous M, Best-Popescu C, Popescu G. Real-time halo correction in phase contrast imaging. Biomedical Optics Express. 2018;9(2):623-35.
76. Chan A, Tuszynski JA. Automatic prediction of tumour malignancy in breast cancer with fractal dimension. Royal Society Open Science. 2016;3(12):160558.
77. Dundar MM, Badve S, Bilgin G, Raykar V, Jain R, Sertel O, Gurcan MN. Computerized classification of intraductal breast lesions using histopathological images. IEEE Transactions on Biomedical Engineering. 2011;58(7):1977-84.
78. Kowal M, Filipczuk P, Obuchowicz A, Korbicz J, Monczak R. Computer-aided diagnosis of breast cancer based on fine needle biopsy microscopic images. Computers in Biology and Medicine. 2013;43(10):1563-72.
79. Weyn B, van de Wouwer G, van Daele A, Scheunders P, van Dyck D, van Marck E, Jacob W. Automated breast tumor diagnosis and grading based on wavelet chromatin texture description. Cytometry. 1998;33(1):32-40.
80. Filipczuk P, Kowal M, Obuchowicz A. Fuzzy Clustering and Adaptive Thresholding Based Segmentation Method for Breast Cancer Diagnosis. In: Burduk R, Kurzyński M, Woźniak M, Żołnierek A, editors. Computer Recognition Systems 4. Berlin, Heidelberg: Springer Berlin Heidelberg; 2011. p. 613-22.
81. Janowczyk A, Madabhushi A. Deep learning for digital pathology image analysis: A comprehensive tutorial with selected use cases. Journal of Pathology Informatics. 2016;7(1):29.
82. Azar J, Busch C, Carlbom I. Histological stain evaluation for machine learning applications. Journal of Pathology Informatics. 2013;4(2):11.
83. Park HS, Rinehart MT, Walzer KA, Chi JT, Wax A. Automated Detection of P. falciparum Using Machine Learning Algorithms with Quantitative Phase Images of Unstained Cells. PLoS One. 2016;11(9):e0163045.
84. Yoon J, Jo Y, Kim M-h, Kim K, Lee S, Kang S-J, Park Y. Identification of non-activated lymphocytes using three-dimensional refractive index tomography and machine learning. Scientific Reports. 2017;7(1):6654.
85. Fisher RA. THE USE OF MULTIPLE MEASUREMENTS IN TAXONOMIC PROBLEMS. Annals of Eugenics. 1936;7(2):179-88.
86. Heang-Ping C, Datong W, Helvie MA, Sahiner B, Adler DD, Goodsitt MM, Petrick N. Computer-aided classification of mammographic masses and normal tissue: linear discriminant analysis in texture feature space. Physics in Medicine & Biology. 1995;40(5):857.

87. Majeed H, Nguyen TH, Kandel ME, Kajdacsy-Balla A, Popescu G. Label-free quantitative evaluation of breast tissue using Spatial Light Interference Microscopy (SLIM). Scientific Reports. 2018;8(1):6875.
88. Kreyszig E. Differential Geometry. Toronto: The University of Toronto Press; 1991. 370 p.
89. Kroon D-J. 2D Line Curvature and Normals 2011 [cited 2017]. Available from: https://www.mathworks.com/matlabcentral/fileexchange/32696-2d-line-curvature-and-normals?focused=5199905&tab=function.
90. Varma M, Zisserman A. A Statistical Approach to Texture Classification from Single Images. Int J Comput Vision. 2005;62(1-2):61-81.
91. Leung T, Malik J. Representing and recognizing the visual appearance of materials using three-dimensional textons. Int J Comput Vision. 2001;43(1):29-44.
92. Matlab script for generating our implementation of the L-M filter bank: Visual Geometry Group, University of Oxford; [cited 2017]. Available from: http://www.robots.ox.ac.uk/~vgg/research/texclass/code/makeLMfilters.m.
93. Hastie T, Tibshirani R, Friedman J. The Elements of Statistical Learning: Data Mining, Inference, and Prediction. New York: Springer; 2009. 534 p.
94. Kumar V, Abbas AK, Aster JC. Robbins and Cotran Pathologic Basis of Disease. Philadelphia: Elsevier/Saunders; 2014. 1408 p.
95. Japkowicz N, Shah M. ROC Curves. Evaluating Learning Algorithms: A Classification Perspective: Cambridge University Press; 2011. p. 148-53.
96. Japkowicz N, Shah M. Isometrics. Evaluating Learning Algorithms: A Classification Perspective. Cambridge: Cambridge University Press; 2011. p. 119-24.
97. Doyle S, Agner S, Madabhushi A, Feldman M, Tomaszewski J, editors. Automated grading of breast cancer histopathology using spectral clustering with textural and architectural image features. 2008 5th IEEE International Symposium on Biomedical Imaging: From Nano to Macro; 2008 14-17 May 2008.
98. Araújo T, Aresta G, Castro E, Rouco J, Aguiar P, Eloy C, Polónia A, Campilho A. Classification of breast cancer histology images using Convolutional Neural Networks. PLOS ONE. 2017;12(6):e0177544.
99. Madabhushi A, Lee G. Image analysis and machine learning in digital pathology: Challenges and opportunities. Medical Image Analysis.33:170-5.
100. Clarke EL, Treanor D. Colour in digital pathology: a review. Histopathology. 2017;70(2):153-63.
101. Sridharan S, Macias V, Tangella K, Melamed J, Dube E, Kong MX, Kajdacsy-Balla A, Popescu G. Prediction of prostate cancer recurrence using quantitative phase imaging: Validation on a general population. Scientific Reports. 2016;6:33818.
102. Sloane JP, Ellman R, Anderson TJ, Brown CL, Coyne J, Dallimore NS, Davies JD, Eakins D, Ellis IO, Elston CW, et al. Consistency of histopathological reporting of breast lesions detected by screening: findings of the U.K. National External Quality Assessment (EQA) Scheme. U. K. National Coordinating Group for Breast Screening Pathology. Eur J Cancer. 1994;30A(10):1414-9.
103. Elmore JG, Longton GM, Carney PA, Geller BM, Onega T, Tosteson AN, Nelson HD, Pepe MS, Allison KH, Schnitt SJ, O'Malley FP, Weaver DL. Diagnostic concordance among pathologists interpreting breast biopsy specimens. JAMA. 2015;313(11):1122-32.
104. Kalluri R, Zeisberg M. Fibroblasts in cancer. Nat Rev Cancer. 2006;6(5):392-401.

105. Arendt LM, Rudnick JA, Keller PJ, Kuperwasser C. Stroma in breast development and disease. Seminars in Cell & Developmental Biology. 2010;21(1):11-8.
106. Tamimi SO, Ahmed A. Stromal changes in invasive breast carcinoma: an ultrastructural study. J Pathol. 1987;153(2):163-70.
107. Radisky D, Muschler J, Bissell MJ. Order and Disorder: The Role of Extracellular Matrix in Epithelial Cancer. Cancer investigation. 2002;20(1):139-53.
108. Bergamaschi A, Tagliabue E, Sorlie T, Naume B, Triulzi T, Orlandi R, Russnes HG, Nesland JM, Tammi R, Auvinen P, Kosma VM, Menard S, Borresen-Dale AL. Extracellular matrix signature identifies breast cancer subgroups with different clinical outcome. J Pathol. 2008;214(3):357-67.
109. Grossman M, Ben-Chetrit N, Zhuravlev A, Afik R, Bassat E, Solomonov I, Yarden Y, Sagi I. Tumor Cell Invasion Can Be Blocked by Modulators of Collagen Fibril Alignment That Control Assembly of the Extracellular Matrix. Cancer Research. 2016;76(14):4249-58.
110. Ajeti V, Nadiarnykh O, Ponik SM, Keely PJ, Eliceiri KW, Campagnola PJ. Structural changes in mixed Col I/Col V collagen gels probed by SHG microscopy: implications for probing stromal alterations in human breast cancer. Biomedical Optics Express. 2011;2(8):2307-16.
111. Provenzano PP, Eliceiri KW, Campbell JM, Inman DR, White JG, Keely PJ. Collagen reorganization at the tumor-stromal interface facilitates local invasion. BMC Medicine. 2006;4(1):1-15.
112. Locker J, Segall JE. Breast Cancer: The Matrix Is the Message. The American Journal of Pathology. 2011;178(3):966-8.
113. Chen X, Nadiarynkh O, Plotnikov S, Campagnola PJ. Second harmonic generation microscopy for quantitative analysis of collagen fibrillar structure. Nat Protocols. 2012;7(4):654-69.
114. Riching Kristin M, Cox BL, Salick Max R, Pehlke C, Riching Andrew S, Ponik SM, Bass Benjamin R, Crone Wendy C, Jiang Y, Weaver AM, Eliceiri Kevin W, Keely Patricia J. 3D Collagen Alignment Limits Protrusions to Enhance Breast Cancer Cell Persistence. Biophysical Journal. 2014;107(11):2546-58.
115. Bredfeldt JS, Liu Y, Pehlke CA, Conklin MW, Szulczewski JM, Inman DR, Keely PJ, Nowak RD, Mackie TR, Eliceiri KW. Computational segmentation of collagen fibers from second-harmonic generation images of breast cancer. Journal of Biomedical Optics. 2014;19(1):016007.
116. Bredfeldt J, Liu Y, Conklin M, Keely P, Mackie T, Eliceiri K. Automated quantification of aligned collagen for human breast carcinoma prognosis. Journal of Pathology Informatics. 2014;5(1):28.
117. Zoumi A, Yeh A, Tromberg BJ. Imaging cells and extracellular matrix in vivo by using second-harmonic generation and two-photon excited fluorescence. Proc Natl Acad Sci USA. 2002;99.
118. Majeed H, Okoro C, Kajdacsy-Balla A, Toussaint JKC, Popescu G. Quantifying collagen fiber orientation in breast cancer using quantitative phase imaging. Journal of Biomedical Optics. 2017;22(4):046004.
119. Boyd RW. Nonlinear optics. Burlington (MA) : Academic Press; 2008. 613 p.
120. Santosh T, Brynmor JD, Kimani CT, Jr., Carney PS. Determination of the second-order nonlinear susceptibility elements of a single nanoparticle using coherent optical microscopy. Journal of Physics B: Atomic, Molecular and Optical Physics. 2011;44(1):015401.

121. Rao RAR, Mehta MR, Toussaint KC. Fourier transform-second-harmonic generation imaging of biological tissues. Optics Express. 2009;17(17):14534-42.
122. Okoro C, Toussaint JKC. Experimental demonstration of two-photon Mueller matrix second-harmonic generation microscopy. Journal of Biomedical Optics. 2016;21(1):016011.
123. Otsu N. A threshold selection method from gray-level histograms. Automatica. 1975;11(285-296):23-7.
124. Bredfeldt JS, Liu Y, Conklin MW, Keely PJ, Mackie TR, Eliceiri KW. Automated quantification of aligned collagen for human breast carcinoma prognosis. Journal of Pathology Informatics. 2014;5:28.
125. DeGroot MH, Schervish MJ. Probability and Statistics: Addison-Wesley; 2012. 911 p.
126. Malik R, Lelkes PI, Cukierman E. Biomechanical and biochemical remodeling of stromal extracellular matrix in cancer. Trends Biotechnol. 2015;33(4):230-6.
127. Liu Y, Keikhosravi A, Mehta G, Drifka C, Eliceiri K. Methods for Quantifying Fibrillar Collagen Alignment. In: Rittie L, editor. Fibrosis: Methods and Protocols. New York: Springer; 2017.
128. Perry SW, Burke RM, Brown EB. Two-Photon and Second Harmonic Microscopy in Clinical and Translational Cancer Research. Annals of Biomedical Engineering. 2012;40(2):277-91.
129. Elmore JG, Nelson HD, Pepe MS, et al. Variability in pathologists' interpretations of individual breast biopsy slides: A population perspective. Annals of Internal Medicine. 2016;164(10):649-55.
130. Jain RK, Mehta R, Dimitrov R, Larsson LG, Musto PM, Hodges KB, Ulbright TM, Hattab EM, Agaram N, Idrees MT, Badve S. Atypical ductal hyperplasia: interobserver and intraobserver variability. Mod Pathol. 2011;24(7):917-23.
131. Francis K, Palsson BO. Effective intercellular communication distances are determined by the relative time constants for cyto/chemokine secretion and diffusion. Proc Natl Acad Sci U S A. 1997;94(23):12258-62.
132. CT-FIRE 2018. Available from: http://loci.wisc.edu/software/ctfire.
133. The logrank test. BMJ : British Medical Journal. 2004;328(7453):1412.
134. Mittal S, Wrobel TP, Leslie LS, Kadjacsy-Balla A, Bhargava R, editors. A four class model for digital breast histopathology using high-definition Fourier transform infrared (FT-IR) spectroscopic imaging. SPIE Medical Imaging; 2016: SPIE.
135. Machin D, Campbell M, Tan SB, Tan SH. Comparing Survival Curves. Sample Size Tables for Clinical Studies. Singapore: Wiley-Blackwell; 2009. p. 84-101.
136. Bay H, Ess A, Tuytelaars T, Van Gool L. Speeded-Up Robust Features (SURF). Computer Vision and Image Understanding. 2008;110(3):346-59.
137. Popescu G, Deflores LP, Vaughan JC, Badizadegan K, Iwai H, Dasari RR, Feld MS. Fourier phase microscopy for investigation of biological structures and dynamics. Optics Letters. 2004;29(21):2503-5.
137. Bracewell R. The Fourier Transform and Its Applications. New York: McGraw-Hill; 1965. 616 p.
139. CurveAlign 2018. Available from: http://loci.wisc.edu/software/curvealign.
140. Candès E, Demanet L, Donoho D, Ying L. Fast Discrete Curvelet Transforms. Multiscale Modeling & Simulation. 2006;5(3):861-99.
141. Cardillo G. KMplot 2008 [cited 2018]. Available from: https://www.mathworks.com/matlabcentral/fileexchange/22293-kmplot.

142. Wen B, Campbell KR, Tilbury K, Nadiarnykh O, Brewer MA, Patankar M, Singh V, Eliceiri KW, Campagnola PJ. 3D texture analysis for classification of second harmonic generation images of human ovarian cancer. Scientific Reports. 2016;6:35734.
143. Whittaker KA, Keaveney J, Hughes IG, Adams CS. Hilbert transform: Applications to atomic spectra. Physical Review A. 2015;91(3):032513.
144. Lucas J, Géron E, Ditchi T, Holé S. A fast Fourier transform implementation of the Kramers-Kronig relations: Application to anomalous and left handed propagation. AIP Advances. 2012;2(3):032144.